Personalised Procedures for Thoracic Radiotherapy

Chi-Shuo Chuang

A dissertation submitted in partial fulfillment

of the requirements for the degree of

Doctor of Philosophy

of

University College London.

Department of Medical Physics and Biomedical Engineering

Proton and Advanced Radiotherapy Group

University College London

June 24, 2019

I, Chi-shuo Chang, confirm that the work presented in this thesis is my own. Where information has been derived from other sources, I confirm that this has been indicated in the work.

Abstract

This thesis presents the investigation, development, and estimation of two personalised procedures for thoracic cancer therapy in Shenzhen, China and two projects were carried out: (1) respiratory motion management of a lung tumour, and (2) the application of a three-dimensional (3D) printing technique for post-mastectomy irradiation.

For the first project, all subjects attended sessions of free-breathing (FB) and personalised vocal coaching (VC) for respiratory regulation. Thoracic and abdominal breathing signals were extracted from the subjects' surface area then estimated as kernel density estimation (KDE) for motion visualisation. The mutual information (MI) and correlation coefficient (CC) calculated from KDEs indicate the variation in the relationship between the two signals. From the 1D signal, through VC, the variation of cycle time and the signal value of end-of-exhale/inhale increased in the patient group but decreased in volunteers. Mixed results were presented on KDE and MI.

Compared with FB, VC improves movement consistency between the two signals in eight of eleven subjects by increasing MI. The fixed instruction method showed no improvement for day-to-day variation, while the daily generated instruction enhanced the respiratory regularity in three of five volunteers. VC addresses the variation of the single signal, while the outcome of the two signals, thoracic and abdominal signals, requires further interpretation.

The second project aims to address both the enhancement of the skin dose and avoidance of hotspots of critical organs, focusing on improving irradiative treatment for post-mastectomy patients. A 3D-printed bolus was presented as a solution for the air gap between the bolus and skin. The results showed no evidence of significant skin dose enhancement with the printed bolus. Additionally, an air gap larger than 5 mm was evident in all patients. Until a solution for complete bolus adhesion is found, this customised bolus is not suitable for clinical use.

Impact

The data collected in this thesis have the potential to raise awareness about personalised procedures in the management of thoracic tumours. In the process of this project, participating patients perceived differences in the effect between a personalised procedure and a conventional method. For the personalised procedure, patients followed vocal instruction, of the same waveform as free-breathing, during radiotherapy, requiring no extra time. Thus, the expected treatment time does not increase compared to the conventional method. During the process, a contactless camera was used as the input source. Patients thus experienced minimal discomfort during the recording of their breathing motion.

Regarding the bolus study, medical physicists should construct a customised bolus for patients during the period between the CT simulation scan and the first treatment day. This period differs for individual patients.

For medical staffs, a user-friendly workflow has been created for both vocal coaching and customised bolus studies. Several types of software are required for steps between gaining the CT images to obtaining bolus products, as well as for post-processing (utilisation of the DICOM file converter and 3D model tool, for example). Special software knowledge and skills are often required for its operation, resulting in additional time and effort to be put in by medical physicists. In circumstances in which time is limiting, obliging medical physicists to apply the presented procedures is likely impractical. With MATLAB software packages, producing workflow can be as simple as drawing a region of interest on the target image. The same holds true for vocal coaching, where personalised vocal instruction is generated immediately after free-breathing is recorded. Medical staffs found learning and operating the software required for vocal coaching easy.

For medical facilities, it is inexpensive to perform these advanced treatment procedures. For vocal coaching in the study, commercial surrogate systems were replaced using Microsoft Kinect, which allowed the total price for building a surrogate system to be reduced to around 200 USD. The system is purchasable by every hospital. In the bolus study, the customised bolus can be manufactured overnight; thus, for hospitals, as compared to ordering the same product from a third company, it is time-saving and productivity-increasing. Overall, the proposed procedures are within a reasonable price for hospital use.

Acknowledgements

The implementation of the research projects described in this thesis would not have been possible without the help, guidance, and collaboration of many excellent researchers. It has been a wonderful experience and an excellent opportunity to carry out my research at top research facilities in both London and Shenzhen, without which, all projects could not have been completed.

Primarily, I wish to express my sincere appreciation to my supervisor, Professor Gary Royle, who guided me through my research project. I am grateful to him for the considerable patience he showed me during the writing stage of this thesis and his great advice for my research proved monumental towards the completion of this study. Always generous with his time, he provided me with countless assistance as I worked my way through the countless hiccups and dead-ends that occurred during the whole process. Needless to say, without his input and guidance, finalising this project would be unimaginable.

I would also like to express my deepest gratitude to Doctor Jamie McClelland who encouraged me to explore every possibility throughout my research project. He has been an outstanding supervisor and has been a great asset with his vast knowledge of medical imaging. His understanding of the needs of his students both academically and on a personal level has always been of tremendous support.

Furthermore, I wish to recognise the invaluable assistance that the Department of Oncology and Radiation Oncology at the Shenzhen People’s Hospital. Dr Li, Dr Xu, Dr Fan, and Dr Catherine provided me with during the acquisition of the clinical data required for the fulfilment of the project.

I want to thank to Prof. Daoyi Chen at Tsinghua University in Shenzhen for entrusting me with the design and development of an entirely new system. With his experience and guidance, I was able to share my knowledge and expertise with the excellent Ocean Science research team.

I am indebted to all my colleagues from the Department of Medical Physics and Biomedical Engineering at UCL, with special thanks going to Dr Reem Al-Samarraie and Dr Catarina Veiga, who were always concerned and supportive in the office and who went out of their way, helping me to relax with joyful coffee breaks and regular Friday evening hangouts.

I would like to pay my special regards to my colleague, Esther Bar, for providing me with valuable guidance on the publication of my first journal article and on structuring my thesis.

Contents

Chapters

List of Figures

List of Tables

List of Abbreviations

AP	anterior-posterior
BH	breath-hold
CBCT	cone-beam computed tomography
COR	centre of rotation
CT	computed tomography
CTV	clinical target volume
CUDA	compute unified device architecture
DIBH	deep inhale breath-hold
DSD	distance to detector
DSO	distance to object
FDK	filtered back projection
FFD	free-form deformation
FOV	field of view
GTV	gross target volume
GUI	graphical user interface
HU	Hounsfield unit
ICRU	International Commission on Radiation Units and Measurements
IR	infrared
ITV	internal target volume
KDE	kernel density estimation
MRI	magnetic resonance imaging
MR	magnetic resonance
OAR	organ at risk
OLS	ordinary least squares
PCA	principal component analysis
PCR	principal component regression
PDD	percent depth dose

PLA	polylactide
PLS	partial least square
PTV	planning target volume
RPM	Real-time Position Management
RT	radiotherapy
SI	superior-inferior
STD	standard deviation
TIGRE	Tomographic Iterative GPU-based Reconstruction
TLD	thermoluminescent dosimeter
TPS	treatment planning system
UCL	University College London
VC	vocal coaching
VR	volume rendering

Preface

Structure of this thesis

The thesis is comprised of two personalised cancer treatment projects with Shenzhen People’s Hospital. In terms of the organisation of the thesis, the rationale, literature review, and aim of the study for each topic of the project are illustrated in their own chapters.

The remainder of the thesis is organised as follows. Chapters 1 and 2 illustrate the research on real-time respiratory motion modelling. Chapter 1 presents an investigation of the respiratory motion model. A motion model was constructed with various surrogate input signals and regression approaches to assess the accuracy of internal motion estimation. The results indicated the proper region for the source of the surface surrogate used in Chapter 2.

Chapter 2 introduces a new method for breathing regulation. The stability of the breathing patterns was evaluated by investigating different instruction protocols. The aim was to develop a simple approach to decrease respiratory variation. The results demonstrated the relationship between internal motion and external movement, which resulted in a simple method being developed for breathing regulation.

Chapter 3 presents an integrated investigation of a 3D-printed bolus. It describes the detailed workflow from the verification of the printed material under dosimetry experiments to the feasibility of its clinical use by evaluating its adhesion with the surface.

Finally, Chapter 4 presents the impacts of the overall findings of this thesis.

Chapter 1

Investigation of the respiratory motion model: A case study

Research aims and contribution

To evaluate the potential of the respiratory motion model to improve the accuracy of motion estimation, the objectives of this project were as follows:

- To re-examine the result of a previously published article on respiratory motion management which introduces the concept of this chapter and pertains to the assessment of the respiratory motion model. By making use of dynamic images, our research aims to investigate the correlation between the external surface and internal motion.
- To compare the motion estimation outcome from different respiratory signals. The internal motion is difficult to monitor during treatment, resulting in difficult internal location pinpointing. However, it is relatively simple to monitor surface movement involved with different breathing signals. The regression model allows the bridging of the respiratory signals (input) and internal location (output). The comparison between the estimated results and actual results is an important stage in signal selection for further studies. Simply stated, the result reveals the best surrogate for motion modelling.
- To evaluate the feasibility of advanced regression methods for internal respiratory estimation. Following the results of the aims in the aforementioned paragraph, motion estimation is improved by using whole-surface signals. To avoid over-fitting the regression model, there is a need to apply advanced approaches to reduce the system's dimensions. The quantitative result within different regression approaches reveals the feasibility of using whole-surface signal and the result reveals the best regression method for motion modelling.

I was in collaboration with the Centre for Medical Image Computing (CMIC) at University College London for this study. My work was to inspect the respiratory model motion presented by Wilms' article [1] and I adapted the current program which is developed by CMIC to meet the purpose of this study. In addition, Wilms' method was compared with other related studies in this study.

1.1 Background

In thoracic and upper abdominal radiotherapy, respiratory induced organ motion is a source of uncertainty that affects the accuracy of radiotherapy planning and delivery and thus is of critical concern. Respiratory motion can lead to the mismatching of tumour location from planning to therapy [2] [3]. Uncertain respiratory motion causes both under-prescribed doses for the target region (a tumour) and over-irradiation of the unwanted area (surrounding healthy tissue). Post-treatment radiation complications such as radiation pneumonitis can occur, with 29% of lung cancer patients developing at least grade 2 pneumonitis after receiving conformal radiation therapy [4]. For a more precise treatment, a number of motion compensation techniques are applied as a technical solution to minimise the negative impact of respiratory motion [5].

Current respiratory motion-compensated techniques exhibit several disadvantages. For example, breath-hold is not suitable for patients with dysfunctional breathing and the risk of pneumothorax increases when implementing fiducial markers. In addition, current image modalities do not possess the ability to monitor tumour motion during treatment. The air in the lungs and the ribs of the chest cavity are the natural boundaries for transmitting ultrasound. This reason leads to very limited soft tissue ultrasound images from the chest. X-rays can capture the entire chest area, but the low contrast between the tumour and the surrounding soft tissues is a problem in distinguishing the respiratory movement of the tumour. Therefore, indirect methods to estimate internal motion are needed for respiratory compensation.

A respiratory motion model is a potential candidate for such a purpose since internal motion can be estimated from the selected external breathing signals. The major advantage of using a motion model is the ability to overcome irregular breathing cycles. The breathing cycle is presented as the average motion within the scanning session, which is unable to deal with variations in the breathing cycle itself. In contrast, a respiratory motion model is able to overcome this problem by monitoring the subtle changes in breathing signals and for this reason, motion models have received substantial attention. However, accurate motion estimation requires a clear input respiratory signal without other noise from physical movement [1], a proper regression approach to bridge the input surrogate and the internal motion. The following two chapters present the result of the motion model, a novel method to monitor external respiratory motion, and the technique applied to regularise the breathing cycle.

1.2 Rationale

This work aims to develop an advanced method to estimate internal respiratory motion. With better knowledge of internal motion, it is possible to more accurately track the tumour and deliver the exact dose as required during treatment. However, direct monitoring of internal motion radiotherapy is challenging. Real-time monitoring is less practical due to poor image contrast to separate the tumour and healthy tissue and low images frame rates from imaging devices. In order to improve treatment quality, an indirect motion estimation method is introduced. The results demonstrated that only small differences (estimated error:3mm <) in motion estimations were observed when applying 1D surrogates, which means to establish a linear relationship between internal tumour motion and one or more surrogate signals using the best fit line, that allows internal motion to be estimated from external respiratory signals [1]. The model includes three components: respiratory signals, movement data, and statistically sound regression approaches.

Major concerns relating to motion model methods include proper external signal selection and regression approach selection, which play an important role in the estimated outcome. Currently, motion models are usually constructed using 4DCT, which is criticised for its demonstration of the average breathing cycle in the recording session. Briefly, 4DCT is incapable of illustrating the variation of each breathing cycle. In order to investigate the breathing variation in each cycle, instead of just the average breathing cycle, this work introduced dynamic MR images for further analysis.

According to Low’s research [5], two respiratory signals are sufficient to improve the estimated accuracy of internal motion. The study focuses on whole-surface respiratory monitoring for multiple signals for motion estimation. The aim of our work is to re-examine the workflow presented in Wilms’ article [7] to evaluate the estimation of internal motion by using various respiratory signals and related regression approaches. The results of this study lead to suggestions for signal selection and regression options for respiratory motion models.

1.2.1 Respiratory motion management

- Tumour margin

To improve the understanding of the overall influence of respiratory motion, it is crucial to define tumour motion. The definition of tumour volume plays a critical role in radiotherapy. According to the International Commission on Radiation Units and Measurements (ICRU), reports 50 [8] and 62 [9], tumour volume is defined as follows:

1. Gross Target Volume (GTV): GTV is defined as a visualised tumour volume following a clinical examination, such as computed tomography (CT) or magnetic resonance imaging (MRI). Delineation of the GTV is a critical process in radiotherapy. Other target volumes are extended from the GTV when an unwanted blurring of the image blurs the tumour contour, which enlarges the GTV into surrounding healthy tissue. Along with obtaining improved breathing information, it is also beneficial to clarify the GTV.

2. Clinical Target Volume (CTV): CTV involves a suspected microscopic margin around the GTV. The range of the CTV is determined using previous pathological studies and patient-specific conditions according to the oncologist’s experience.

3. Internal Target Volume (ITV): ITV highlights a crucial spot for moving tumours, especially thoracic and upper abdominal tumours. The ITV is defined as the CTV and its physiologically internal margin. Thus, the ITV encompasses changes in the shape and size of the CTV during physical

movement caused by heartbeats, the breathing cycle, or random muscle contractions. This description indicates that the ITV is related to dynamic serial images taken over a period of time, and thus, the delineation of the ITV is barely viable with only conventional 3D image approaches.

4. Planning Target Volume (PTV): PTV includes ITV and added mechanical uncertainty (from both the beam delivery system and setup error). To ensure a positive treatment outcome. PTV must not receive less than the prescribed dose

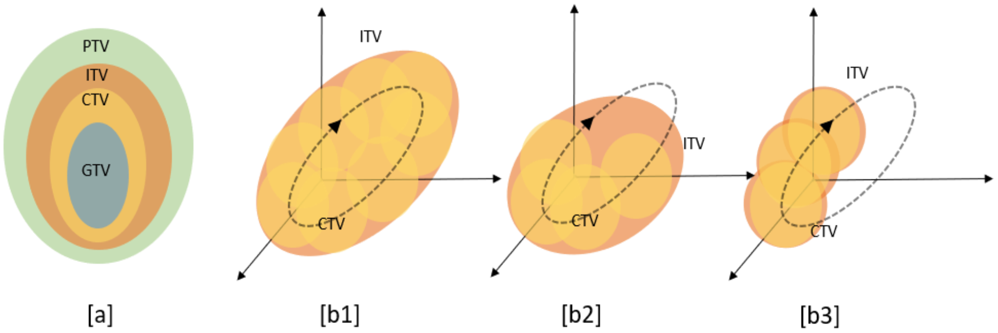

Figure 1.1: Demonstration of tumour volume definition by ICRU 62. [b] Comparison of conventional and modified ITVs. In conventional 3D RT, the ITV should cover all the marginal of the CTV that might irradiate excess normal tissue. With a motion compensation technique (for example, gating [b2] or tracking/modelling [b3]), the ITV can be shaped with superior knowledge of tumour movement.

- Technical solutions for respiratory motion management

Breath-hold (BH) and deep inhale breath-hold (DIBH) are generally regarded as the easiest and simplest approaches to respiratory motion immobilisation [4, 11]. DIBH is a patient-friendly approach requiring minimal coaching with significant benefits, one of the important ones being that it pulls critical organs (for example, the heart or spinal cord) away from the hot-spot, thereby potentially reducing radiation toxicity. However, there has been some doubt as to whether patients are typically capable of holding their breath for more than 30 seconds; in particular, those who suffer from pulmonary dysfunction. For this reason, DIBH appears to be inadequate in a number of clinical situations (for example, tomotherapy and arch therapy). Furthermore, intra-fraction variations of 1.4–2.5 mm will certainly involve a larger volume of normal tissue to accommodate a realistic PTV [4]. Therefore, when BH and DIBH are used, intra-fraction variation is involved.

For a superior dose distribution, direct or indirect knowledge of the tumour location in each breathing cycle becomes critical; thus, ideally, tumour tracking will be the best method of motion compensation. The idea of tumour tracking is that if a tumour shifts, then the motion can be accurately detected and followed, providing migratory information with medical images. However, limited apparatuses exist for tumour tracking. A fluoroscope is a popular choice, according to TG76 [5,12-21], demonstrating a group of studies have been presented. But the poor tissue-tumour contrast when using a fluoroscope makes this approach unfeasible. As an alternative, radiopaque fiducial implants can be embedded near or inside a tumour, but the difficulty with such implants is twofold. First, physicians are reluctant to implant fiducial markers for the purpose of radiographic or fluoroscopic tumour localisation because of the risk of complications during and after biopsy, including infectious complications and pneumothorax. As shown in various studies, needle induced pneumothorax ranges between 8% and 38% [22]. The second issue with fiducial implants is the uncertainty associated with their placement in the lungs. Residual migrations of fiducial markers have been reported [23] and these fiducial implants became unreliable when they were dislocated from the target locations where they were originally situated. Therefore, some non-invasive strategies have been developed to deal with the estimation of respiratory motion, as well as to safeguard patients from potential risks and complications.

As a consequence, indirect tumour-localising methods currently rely on breathing signals as surrogates for internal motion, interplay the position of the internal tumour motion with breathing signals. Indirect localisation methods require the attachment of devices, known as surrogates, to monitor the respiration-induced physiological change. It is assumed that a perfect relationship exists between the external and internal motions. Respiratory gating leads to higher robustness and reliability in each breathing cycle through the imaging of data from a selected window, according to breathing surrogates. Theoretically, gated treatment verification could increase both setup and residual migration reduction, resulting in an approximate PTV and CTV [24]. Furthermore, it is compatible with most patients after regularised breathing cycle training, and many types of surrogate systems exist for different breathing information. These include spirometer [22,25] for lung volume, and electromagnetic tracking systems[26], optical tracking systems [27], and respiratory belts [28] for the displacement of the chest or abdomen, which have been investigated for certain applications. However, gated treatment has the predictable consequence of increasing treatment time, so the optimisation of both time and accuracy is required. The respiratory motion model is presented as a possible solution [29].

In this study, we addressed the following question: If multiple surrogates can be generated from the skin surface, do they estimate tumour location more effectively with a high-dimensional system? Verification of the degree of freedom is a crucial step in the motion model. The second question we addressed was the following: Can we modify the current signal to improve the overall system? Some results demonstrated the importance of a signal’s gradient, which may have a positive influence on the estimated accuracy. This could potentially provide us with another method for enhancing the model’s computational efficiency.

Compared with multivariate regression approaches, we attempted to minimise the portion of signal components when the estimated errors were still accepted, which shows that the rest of the signal can be ignored. In this chapter, we present an investigation of a single case study by following the concept of Wilms, which his concepts is to compare the feasibility of the motion model using various regression approaches.

The major difficulties of respiratory motion estimation arise from intra-cycle variation, also referred to as hysteresis, specifically, the path of respiration-induced motion may change from inhalation to exhalation. Most current surrogate devices (e.g., the spirometer or thoracic-abdominal belt) can only generate 1D signals. However, if a 1D surrogate has a perfect relationship with the internal motion, the motion model can still provide an accurate estimation [30,31].

- Internal-external relationship

Koch [32] demonstrated that skin markers have the strongest correlation with internal landmarks and are direction-dependent. The volunteers and patients in the study had surface markers placed on their skin, which provided an improved technique in which the internal landmarks in the thoracic cavity and skin movement were monitored simultaneously, overcoming the limited scanning area for 4DCT. In general, SI motion correlated more with lower markers near the abdomen (correlation coefficient [CC] = 0.89), whereas AP motion correlated more with markers on the chest (CC = 0.72). However, the overall correlation of internal landmarks with skin fiducials was not always strong. The study concluded that effective tracking of respiration might rely on a combination of multiple sources of signals or other physiological parameters. Therefore, limitation to single-channel surrogates may preclude proper motion estimation. A similar outcome was reported by Fayad [33], where some internal landmarks were independent of skin motion. That is, a single signal was not sufficient to depict the entire internal path. However, Koch selected specific markers on the skin, and full skin information available was not taken into account. Furthermore, Koch was able to demonstrate the relationship between multiple markers with internal targets and highlight the skin sources to describe internal motion. Notably, the number of dimensions of a signal determines the degrees of freedom in the corresponding model. Following the conclusion of Koch, a 1D signal is not suitable for complete modelling of internal motion.

To extend the signal dimensions, derivative signals generated from raw signals have been investigated to study motion models, and time deviation or gradients of spirometers have been integrated for estimation. Low et al. [5] were highly original in their approaches. Tidal volume and airflow were used as surrogate signals, and the path of landmarks could be described by the linear function of tidal volume and airflow. A good agreement existed between the motion model and 4DCT image (average discrepancy = 0.75 mm). The model was also robust over a period of weeks. This research demonstrated that consideration of the gradient of the surrogate was key when extending the number of surrogates. Nevertheless, the use of spirometers may not be universally applied to all patients as it is limited by patient condition.

Because skin surrogates can generate multi-dimensional signals suitable for informing the finer manipulations required for respiratory motion modelling, signals from different locations are occasionally highly correlated with one another, which may result in a motion model suffering from over-fitting [34]. Over-fitting is a phenomenon where the number of predictors grows to be too large and sample data are likely to fit the model perfectly, but will nevertheless fail to predict new outcomes well.

Hence, a situation arises in which the complexity of the overall system should be simplified to avoid unwanted over-fitting events. Wilms demonstrated different correspondence approaches for a motion model with multiple skin inputs. Using the database of 4DCT and 4DMR, the virtual surrogate signals can be generated to simulate real respiratory behaviour. In the report, a spirometer, a thoracic-abdominal belt, and range image (skin surface) were used. The report concluded that using a reduced-dimension approach instead of the ordinary least square (OLS), although not necessary in all cases, may help to reduce over-fitting in the case of very high-dimensional signals, by lessening the complexity when reducing the dimension. However, some cases in the report used the 4DCT or 4DMR where images from 4DCT are already processed by averaging every breathing cycle and analysing inter-cycle variance is difficult and a similar situation which exists for 4DMR may increase errors when tracking landmarks.

Our study utilised 2D+t MR series images with an improved spatial resolution to track internal landmarks. Although LR motion cannot be tracked, it is negligible in most cases, and there is, therefore, sufficient resolution for inter-cycle analysis. Wilms' work inspired the principle idea, that is through reducing dimensions, thereby simplifying the complexity, the problem of over-fitting can be solved. The major aim of this chapter is to evaluate Wilms' article, which provides an extensive discussion of the evaluation of various types of common breathing signals and different regression approaches for internal motion estimation. The study offers a comprehensive framework for examining the feasibility of each scenario, using both 4DCT and 4DMR as image sources. Using the images from both 4DCT and 4DMR, the data set covered intra- and inter-cycles and a detailed framework was presented for correspondence-modelling based on multivariate regression. The major outcome of this study was the generation of simulated multiple surrogate signals (spirometry, abdominal belt, and diaphragm movement) from 4D images.

Furthermore, the signal gradients were calculated for other input breathing signals. The results demonstrated that no significant differences in motion estimations were observed when applying 1D surrogates. The results highlighted that the application of 2D breathing signals, including the signals with their gradients, may be necessary for an accurate motion model since the accuracy of internal motion estimation was improved as the number of surrogate channels increased. Finally, no significant differences were observed between motion models calculated using corresponding methods.

Overall, the selection of breathing signal played a more crucial role than regression approaches for internal motion estimation. Although Wilms extensively investigated motion models and obtained conclusive results, the image source was actually an issue, particularly because of intra-cycle variation. The 4DCT images, sorted by the breathing phase, illustrated the average breathing cycle during recording. However, subtle changes in a single cycle were lost in the process and could no longer be observed. This may have led to estimation uncertainty due to slight variations. For 4DMR images, although intra-cycle variation could be accounted for, temporal resolution was 0.5s per frame while the spatial resolution was merely 3.91 x 10 mm. Such poor resolution obscured the fine movement of internal landmarks, which may have decreased the effectiveness of the regression approach.

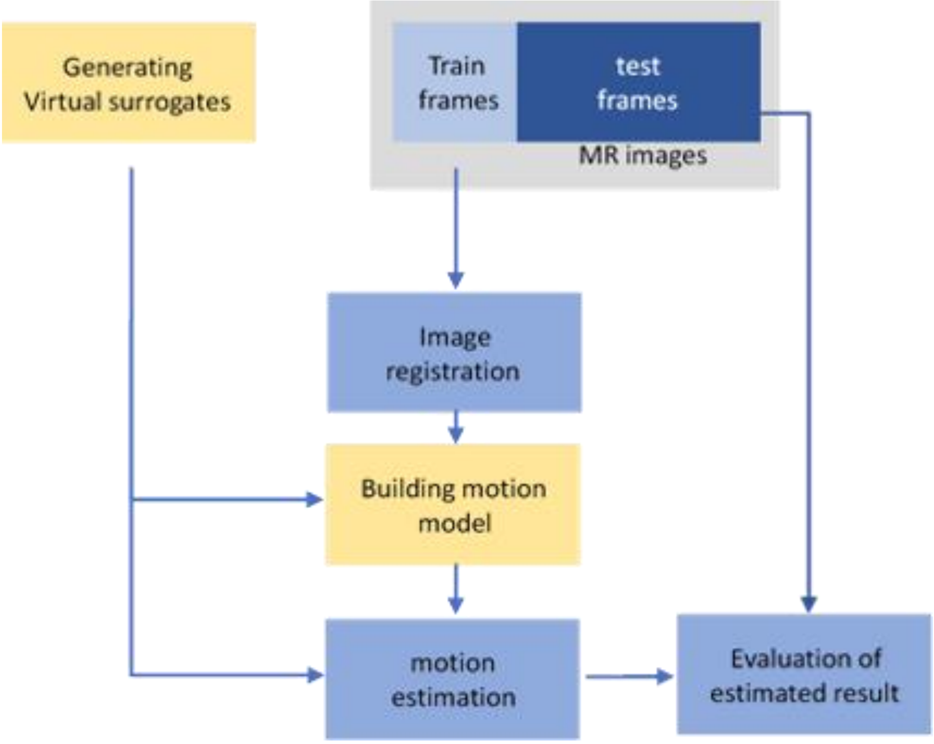

Figure 1.2: Workflow of motion model evaluation.

In the present study, 2D+t MR with high spatial and temporal solution in the selected slice was used for a large FOV and landmark points within the body required to define this research clearly. The left/right (LR) motion was assumed to be negligible for the assessment of the motion model as there was minimal LR motion in most patients. However, future work will investigate the feasibility of extending capture from 2D to 3D to register all internal motion during breathing. The aim of the present study is to evaluate different surrogate input and regression approaches for motion estimation. Hence, we present a case study of dynamic MR with finer scanning parameters.

1.3 Materials and Methods

1.3.1 Image data

First, we recorded a dynamic MR series of a free-breathing volunteer. To maintain a high spatial and temporal resolution in our work, 2D sagittal slices with a pixel size of 0.94 x 0.94 mm and a rate of four frames per second for 300 frames were used. The resulting image has a resolution much higher than those used in Wilms' work (pixel size of 3.91 x 10 mm and 2 frames per second rate in AP/SI). The coverage of dynamic imaging ranged over nearly the full body trunk (from the upper lung to the middle pelvis structure). Figure 1.3 [a] shows the first frame of the series.

1.3.2 Generating virtual surrogates

Because the skin measurements were derived from MR images, our method was similar to Wilms' work where the additional surrogate signals were required to be synchronised with the source images [30, 35]. There is a misleading time for two data results in incorrect external-internal relationships, but the motion model with single-source data is able to overcome this problem. Moreover, the wide coverage of MR images is capable of covering the entire surface; that is, virtual surrogates, referring to the indirect respiratory movement monitoring by series clinical images, can be generated either from the thoracic belt or Real-time Position Management (RPM) in the abdomen for the investigation of the feasibility of each surrogate for the motion model. The virtual surrogates can be directly interpreted into the current surrogate system.

In this study, the skin surface was automatically detected using Otsu's method [36] on the images, in which clustering-based image thresholding was performed automatically. Otsu methods can compute a single intensity threshold that separates pixels into two groups with the lowest variation within each group. The series images were then re-sorted into the new axes: AP axis, and acquisition time (Fig. 1.3 [b1]). There was a clear respiration-induced waveform in the re-binned image for the subsequent external change, and later, two major clusters can be observed on the intensity histogram (Fig. 1.3 [c]). The skin, which contains an amount of fat tissue, could be separated from other organs by using the Otsu's method as fat tissue generates a high-intensity signal, allowing separation by automatic binary segmentation. The dynamics MR image shows greater intensity from the fat, whereas the skin surface contributes to the creation of a weaker signal. Poor signals make it difficult to capture movement. Therefore, a signal from the skin could not be detected in this section

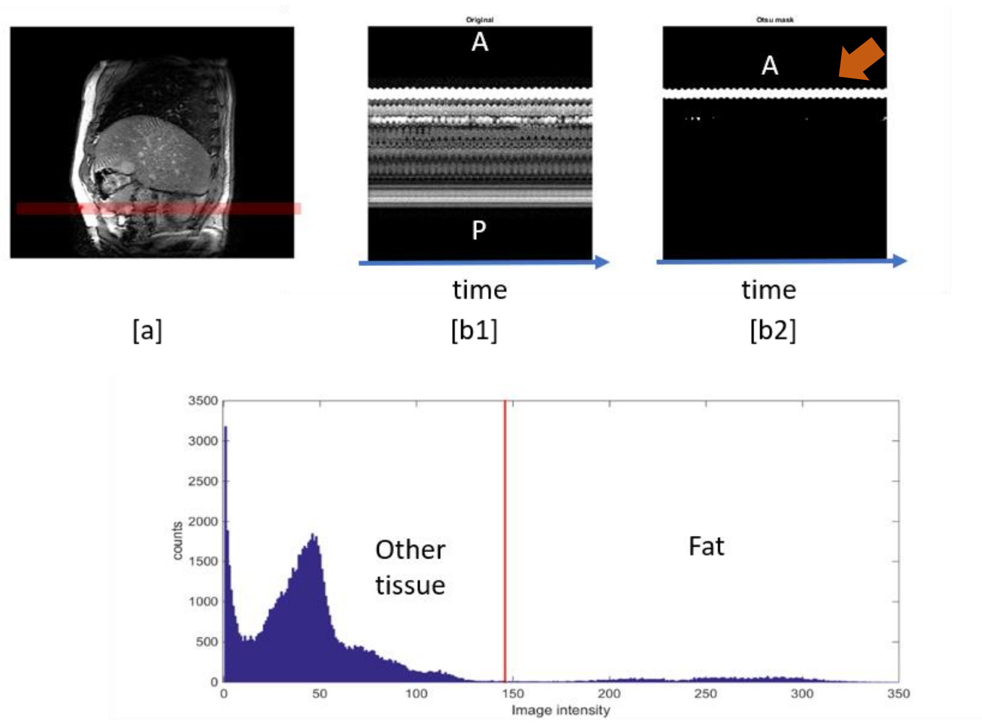

[a] [b1] [b2]

[c]

Figure 1.3: Example of Otsu's method for signal generation. [a] Demonstrates the selected slice as the virtual surrogate. [b1] and [b2] are the selected slices aligned by time. [b2] shows the result of Otsu segmentation. [c] illustrates the intensity histogram of [b1].

Figure 1.3 [a] shows the selected slice, which after being manipulated by AP and time dimensions is shown in [b1]; figure 1.3 [c] shows a histogram of non-zero intensity for the demonstration image [b1], in which the threshold computed by the Otsu’s method is shown as a red line. The image intensity distribution can be separated into two groups: high intensity (fat) and low intensity (other tissue).

Figure 1.3 [b2] shows the result of high-intensity mask processing, where after masking, the image was converted to binary. Detecting the first nonzero voxel form anterior boundary became the displacement of the skin surface (see the brown arrow in Fig. 1.3 [b2]). After we divided the full skin into five equal segments, we reduced the noise from the MRI by averaging the signal to generate five virtual surrogate signals. The gradient of each signal was also calculated, giving a total of ten surrogate signals. OLS-1 is a single surrogate signal from the abdominal segment (Pseudo-RPM is to mirror the respiratory surrogate of RPM system) while

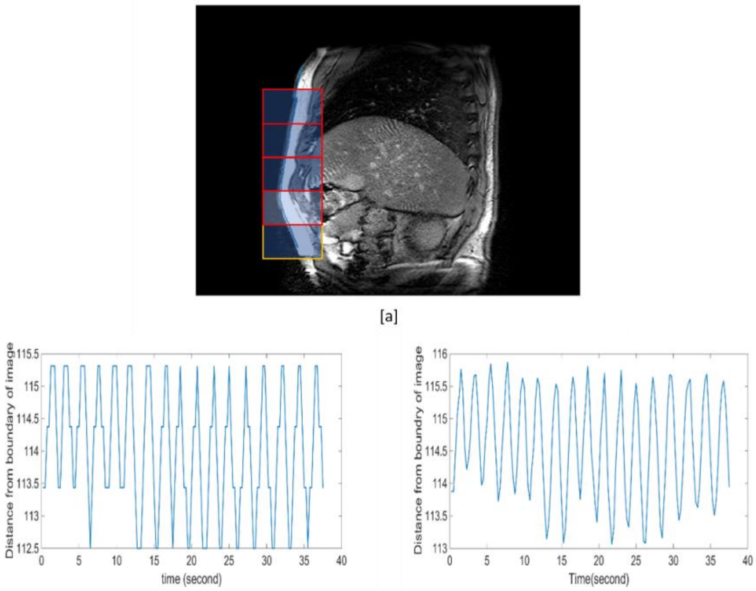

[a]

[b1]

[b2]

Figure 1.4: Signal from abdominal segment and its gradient. [a] shows the skin detection of the first frame. The OLS-1 [b1] signal was from the yellow box in [a] and the OLS-5 [b2] signal was the average displacement from the yellow box and all the red boxes.

OLS-1G is the signal from the abdominal segment plus its gradient. Because of the limitations in time and spatial resolution inherent in MR, the virtual signal for the signal row appeared to be discrete. To simulate the surrogate signals as more realistic events, each signal was averaged from five segments for them to be smooth and continuous. OLS-5 represents the averaged signals from all 5 segments (full skin monitoring), while OSL-5G represents and all signals and their gradients.

1.3.3 Image registration

The result of the image registration shows the vector field, which illustrates the entire respiratory motion. Compared with landmark tracking, which focuses on selected points, the image registration method is straightforward, comparing the difference between the target image and reference image, for analysis using image processing. In terms of regression, computation of the vector field is less computed than advancing pixel-by-pixel when estimating internal motion, where the internal motion was computed from the frames using B-spline-based deformable image registration [37], which is an intensity-based deformable image registration method that has recently become a powerful tool in image processing. The package used for registration, NIFTYREG, was developed by the Translational Imaging Group with the Centre for Medical Image Computing at University College London, United Kingdom [38].

Intensity-based registration estimates the deformation from all image voxels. Not only does every voxel contribute information about the deformation, but it also accelerates computing in the transfer process. The basic procedure of deformable image registration consists of three parts: similarity measurement, transformation, and optimisation. The goal of registration is to minimise the cost function between the two images and regulate transformation.

$$F = (1-\alpha)S(I_f, T(I_m)) + \alpha R(T(I_m)) \tag{1.1}$$

The general form of image-based registration is shown in Eq. 1.1, where I_f is the fixed image (target image or reference image), which is the goal of transformation; I_m serves to move the image (floating image); F refers to the cost function for registration, which seeks for minima during the process; T donates to the transformation of the image; S is the similarity metric between the fixed image and the transformed moving image; R represents a smoothing term to remove the unwanted deformed field from I_m; and α is the weighting parameter defining the trade-off between the similarity measure and regularisation of the transformation.

For this study, the core registration session was conducted by free-form deformation (FFD) based on a B-spline. A basic framework of the registration process is initiated with the transformation of moving the image. After mapping deforms the moving image to the coordinate space of the fixed image, the outcome of the cost function can be calculated. The current cost function shows the fitness of the mapping. The optimiser sets new transformation parameters according to this measure, and the iteration loop is repeated until convergence.

The purpose of applying image registration is to create the vector for internal movement. In this case, the registered result brings the vector field, which incited the regional movement of human tissue during respiration. It is one of three-part to build motion model. Then, regression aspects bridge external signal (virtual surrogate) and internal motion (vector field after registration) to complete the entire motion model.

1.3.4 Multivariate regression aspects

The multiple input surrogate signals may lead to the over-fitting of the motion model. Furthermore, different surrogates may contain similar information and are, therefore, redundant. The regression approaches were described in Wilms' article. Decreasing the dimensions of the multiple surrogate signals allows for the simplification of the complexity of the overall model, by removing similar respiratory signals from the input matrix, as well as highlighting the critical components in external and/or internal motion [1].

1.3.5 Assessment of respiratory motion models

1. Ordinary least squares

OLS, or so-called linear least squares, is an approach for estimating the unknown parameters in a linear regression model. From here on, X is the predictor of the surrogate signal matrix; Y represents the response; and the B-splined fields are represented by $Y \in R^{2m}$ and $X \in R^{n \cdot sur}$, where m denotes the number of control points of an image.

$$X = [S_1, S_2, \ldots, S_n] \quad (1.2)$$

$$Y = [V_{1(t)}, V_{2(t)}, \ldots, V_{n(t)}] \quad (1.3)$$

In the common context of OLS, the least-square solution for

$$Y = XB + \varepsilon \quad (1.4)$$

2. Principal component regression

   In principle, OLS can be applied usefully with numerous input/output variable. In some scenarios involving highly complex models, however, over-fitting may occur. There may be only a few underlying or latent factors that account for most of the variation in the response, and PCR is an efficient method to remove noises from the input function in multivariate regression. In principal component analysis (PCA), high-dimensional data are simplified by translocating coordinates to approach variance and covariance maxima and minima, respectively, which requires uncorrelated raw data to avoid the problem of high redundancy. The function of the PCR is to regress the output function by including only selected principal components. Principal component regression is a standard linear regression model that uses dimensionality reduction, with little loss of information, based on PCA performed on the surrogate measurements first.

3. Partial least squares

   When comparing PLS with PCR, PLS is found to be similar to PCR with the difference that the response is not considered. Principal component regression addresses only the uncorrelated signals in the observed (input signal/surrogate signals in the research) part and does not involve further processes to determine the expected outcome. Dimensionality reduction is not guaranteed to be successful. While for PLS, the core process involves consideration of both the surrogate data and the internal vector field with latent variables. The general idea of PLS is to try to extract these latent factors, account for manifest variations as accurately as possible while simultaneously model the responses accurately. For this reason, the acronym PLS has also been taken to mean projection to a latent structure.

The scores of observation and prediction were chosen so that the relationship between successive pairs of scores was as strong as possible. In principle, this is similar to a robust form of redundancy analysis, seeking directions in the factor space that are associated with high variations in responses, but biasing them towards directions that are accurately predicted.

Because no gold standard exists for motion estimation, the estimated error becomes the proper criterion; this is the difference between the actual location and estimated motion by the surrogate. The core task is to focus on the various surrogate signal(s), and different correspondence approaches for motion estimation. This study proceeded along two independent paths: surrogate generation and internal motion monitoring. The method of signal production is described in subsection 1.3.2.

There were four surrogate signals in this study: OLS-1 (abdominal movement), OLS-1G (abdominal movement with its signal gradient), OLS-5 (average of all movements from the surface), and OLS-5G (average of all movements from the surface with its signal gradient). Internal motion makes use of the vector field from image registration. In this assumption, if the series images perfectly align with the reference images, the vector field from the B-splined registration can be considered the internal motion. The first 100 frames serve for the train frame to establish the motion model, and the other 200 frames serve for evaluation when comparing estimation outcomes from the models. There are three correspondence approaches in the complete task, namely OLS for all four surrogates and PCR and PLS for OLS-5G.

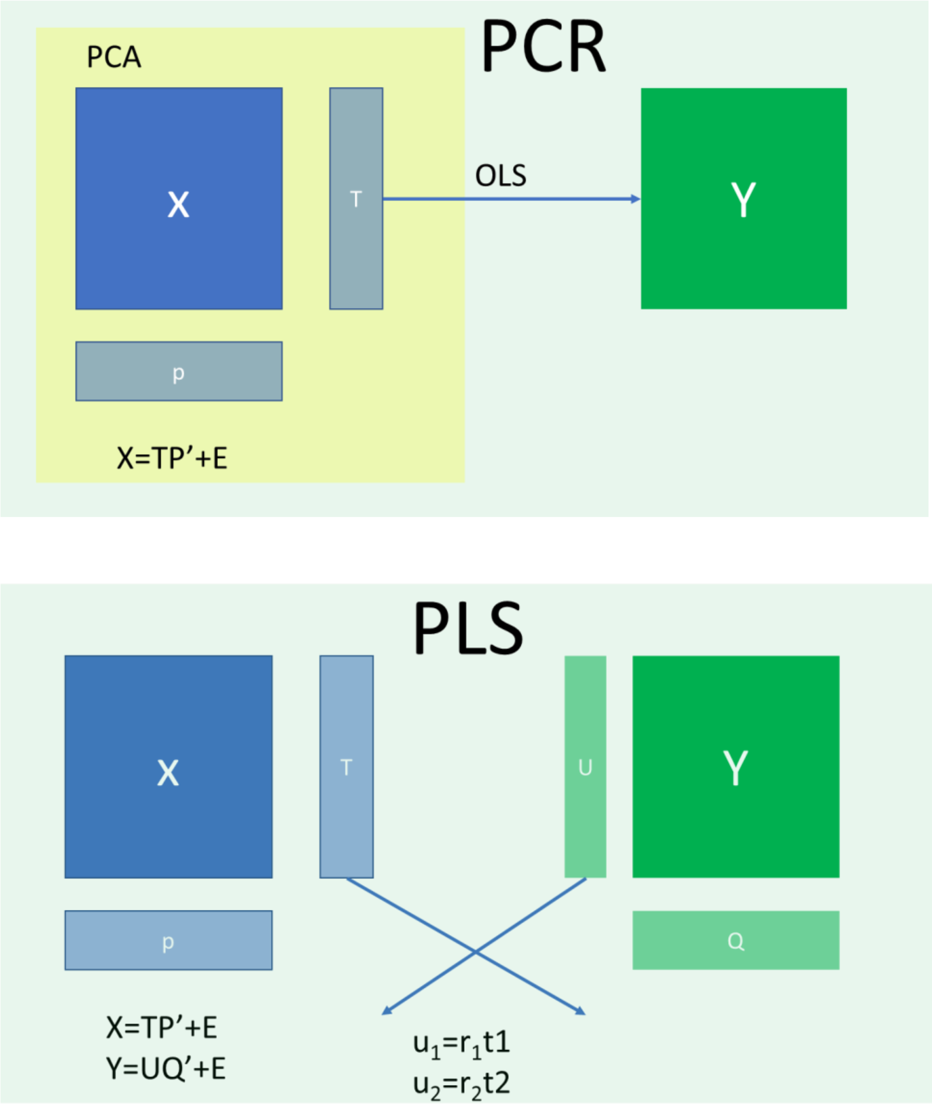

Figure 1.5: The demonstration of PCR and PLS methods.

(1) For PCR, **X** is decomposed into score (**T**), load **(P)** and residual (**E**) through the PCA model. The matrix T contains the original data in the rotated coordinate system (the variance displayed in each dimension is the largest). Then, an OLS model is established between the matrix **T** and **Y** variables.

(2) In the case of PLS. Both **X** and **Y** are broken down into their scores and loads. PLS does not find the eigenvalues and eigenvectors of the X variable, like PCA, but finds the maximum covariance between **T** and **U** (score matrix).

The evaluation of the motion model used five manually selected landmarks which are clear in full image series. The mismatch errors between the test frame and estimation outcome are criteria to judge the reliably of each approach. Another criterion is the target compensation time. This parameter represents the duration of estimation for which the error is less than a setup goal, measured to within 1 mm. In this study, the portion of test frames in which the estimated errors were lower than the setup goal was defined as the target compensation time. A longer compensation time meant more stable approaches for motion estimation.

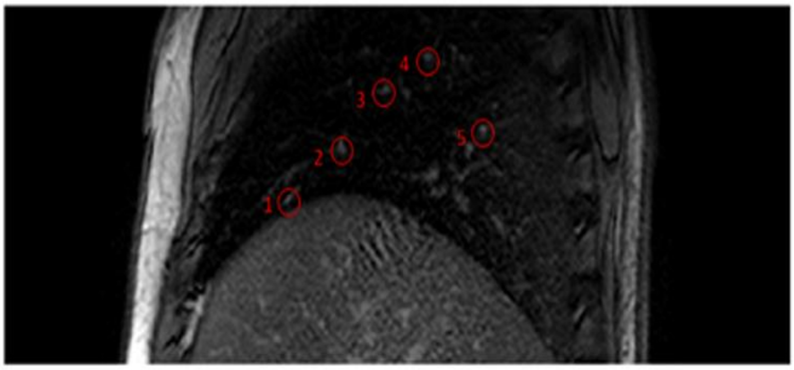

Figure 1.6: Five target landmarks for evaluating registration and motion compensation results.

1.4 Result: Assessment of respiratory motion estimation

1.4.1 Virtual breathing signals

The selection of surrogate signals is based on their quality. If a signal contains a large amount of noise, that signal is not suitable for use in building the motion model. At first glance, all the signals seem to reflect periodic changes induced by respiratory movement. Hence, the Otsu mask approach appears to be successful in deriving skin surface displacement as surrogate signals.

In this case, Seg. 5 (abdominal movement), a pseudo-RPM, demonstrated great potential and is commonly used as the surrogate source as it is within a significant displacement of all other sources, to get a less noisy signal, whilst being poorly correlated with Seg.1 to Seg.4 (CC = 0.38 ±0.24, <0.6). On the other hand, Seg. 1

(thoracic movement) showed high correlation (CC = 0.74 ±0.32, >0.6), indicating that there is a phase mismatch between them. Breathing pattern mismatching, which is the phase difference between thorax and abdomen, agrees with the assumption that people normally breathe using two major methods: thoracic breathing and abdominal breathing. In analysing the surrogate signals (displacement motion for all 5 seg) using PCA, the summation of the first two principal components described nearly 99% (76.8% and 22.2% for first and second components, respectively) of the movement variance in all virtual surrogate signals. The first component was correlated with Seg. 5 (CC = 0.98), and the second component was correlated with Seg. 1 (CC = 0.91). These two principal components represented the vast majority of surrogate data. Therefore, it can be concluded that the two principal waveforms form the entire surface motion. The other three signals are produced by mixtures of these two components. Based on the PCA test, the volunteer presented in Fig. 1.6 showed normal abdominal breathing.

The frequency analysis of the first 15 and last 15 seconds of the respiratory rhythm change during MR scanning is presented in Fig 1.7. The major finding revealed that the first 15 seconds of signals (blue) were more irregular and faster, showing wide and short peaks with mixed frequencies while the last 15 seconds (red), showed sharp peaks with a single frequency component (0.44 Hz). The changing breathing cycle may accommodate various regression coefficients for the correspondence model and provides us with a guide for large test cases. In addition, this finding that indicates an anxious patient led us to assume that a relaxed breathing pattern was more regular, which is evaluated in Chapter 2.

For this frequency analysis, the dominant frequency was 0.44 Hz (i.e., 26.5 cycles/minute for all monitoring time, despite the normal rate is around 12 to 18 cycles/minute [11]). Possible reasons for the fast breathing rate are the volunteer being anxious (as opposed to claustrophobic) or MR coils compressing the movement of the chest wall, thereby limiting the volume of the thoracic cavity. In this latter case, the volunteer would be required to raise their breathing cycle to take insufficient air. Given that this breathing rate was relatively fast and shallow, slight internal movements of this case were retained for later motion evaluation.

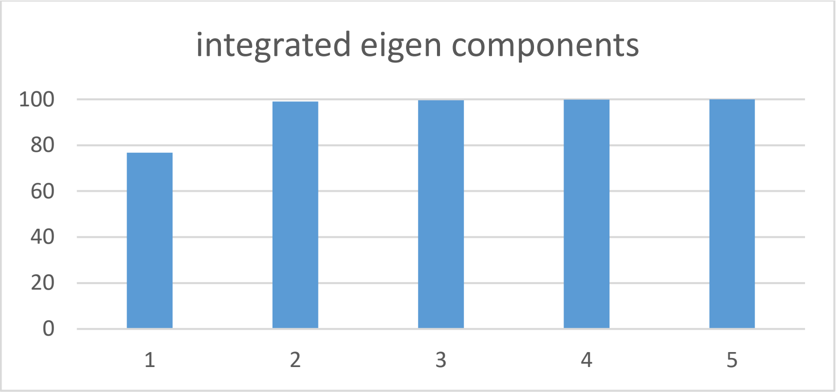

Figure 1.7: Components represent the portion of the original surrogate signals for 5 region.

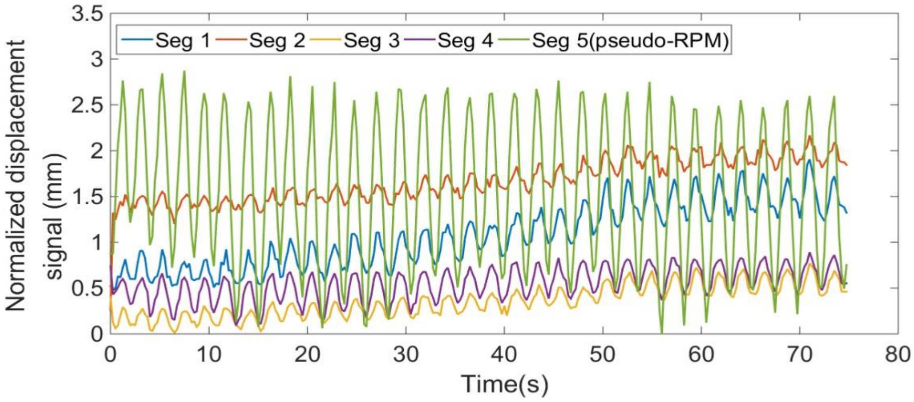

Figure 1.8: Five virtual respiratory signals from five equal-length skin regions from superior to inferior of a volunteer, with a duration of 75 s (i.e., a total of 300 frames). All signals are normalised, with zero as the minimised value. Among them, Seg. 5 (signal of abdominal movement) is considered a pseudo-RPM and requires further analysis. Clear baseline shifting is observed in Seg. 1 (signal of thoracic movement) Such shifting means that the relationship between external movement and internal motion may change, resulting in uncertainty of the motion model if only these signals are used.

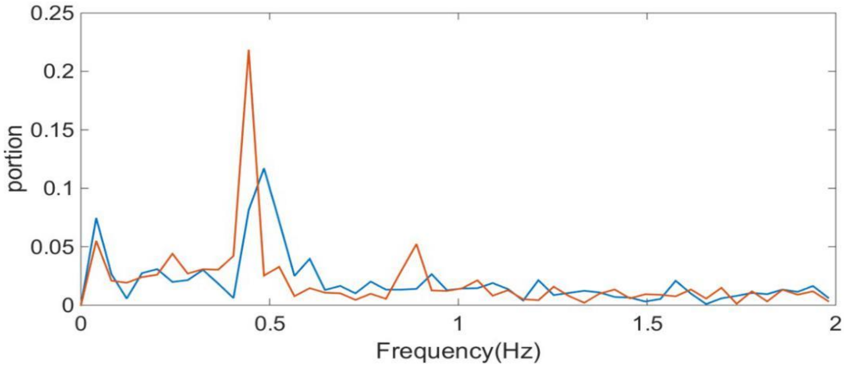

Figure 1.9: Frequency analysis of Seg. 5. The blue and red spectrum represent the frequency of the first 15 seconds and the last 15 seconds signals. The respiratory rhythm shifted from irregular to more regular, showing a sharp peak of major frequency for the red spectrum.

The phase of Seg. 5 was ahead of the phase of the other signals, implying that SI motion was faster than AP motion for each cycle. Phase shifts were assessed between all five virtual skin signals, using manually determined end-points for exhalation. With 95% confidence intervals for all phase differences from all virtual surrogates, there were significant phase shifts between Seg. 5 and Seg. 1, 2, and 3 ($p < 0.01$, T-test). Seg. 5 was further ahead of the end-of-exhale point than the thoracic region (mean = 0.17 s) in a statistically significant manner ($p < 0.01$, T-test). When comparing mean displacements from the first 10% (7.5 s) of the session with the last 10%, all sections except for Seg. 5 (which decreased by 0.3 cm) increased by between 0.21 and 0.83 cm. The increased mean displacement illustrated thoracic cavity enlargement through relaxation. Providing that the correlation of the surrogate internal field is constant, the initial session may not have provided a proper surrogate signal recording time in this case. However, This result provides us with a useful parameter that can be used to set up a phantom for physical testing. For example, the cycle time of chest movement (15 cycles/min) and the displacement of internal markers (6mm in SI movement). These parameters can help establish a simulated chest model for quantitative analysis in further research. The programmatic phantom is able to move as setting up. By understanding the parameters of internal and external motion, we can eliminate the noise of uncertain signals and focus on the evaluation of the regression model.

1.4.2 Lung landmark tracking

The internal motion of selected landmarks is tracked by template tracking across total dynamic frames. The standard starting point is the location of frame 6, a reference image for the next session. Frame 6 corresponds to the end-of-exhale point, which is seen as a relatively reproducible location in each cycle.

Initially, we supposed that landmark 1 (L1) displayed the longest mean trajectory because of its location near the diaphragm. However, the volunteer in question had a rapid respiratory rate, and thus the migration of the diaphragm was not as expected, compared with normal free-breathing people with normal respiratory rate. In contrast, landmark 5 (L5), located in the posterior middle lung, showed the largest mean and maximum displacement of all landmarks (max. 2D displacement for 5.13 mm). In Fig. 1.8, the end-of-exhale point of the surrogate does not agree with L1 and landmark 2 (L2). The end-of-exhale points of L1 and L2 occur 0.25 seconds after the surrogate signal. x. This result shows the latency between external movement and the internal landmark motion.

	L1	L2	L3	L4	L5
2D	2.21± 3.12	2.23± 2.45	2.51± 3.58	2.77± 1.78	3.45± 4.32
SI	1.90± 1.45	1.82± 1.25	1.93± 1.87	1.93± 1.55	2.67± 2.51
AP	0.76± 1.02	0.83± 0.98	1.22± 1.10	1.74± 0.43	2.07± 1.73
R2	0.43	0.22	0.05	0.07	0.68

Table 1.1: The mean 2D Euclidean, SI, and AP distance for each of the target landmarks (in mm) and the regression coefficient for the evaluation of hysteresis.

Figure 1.10 demonstrates the hysteresis of the target landmarks. Without hysteresis, the trajectory would have been a straight line. Hence, the level of hysteresis in each landmark was evaluated from the R^2 value of simple linear regression. The R^2 results in Table 1.1 show that all landmarks travel with different levels of hysteresis. The results also agree with the idea that the distance of the landmarks to the diaphragm has an influence on hysteresis behaviour. The contraction of the muscles of respiration during inhalation flattens the diaphragm, drawing it downwards, thus altering the distance to landmarks, which in turn increases the complexity of the internal trajectory (owing to other forces behind respiration increasing). The longer distance from the diaphragm to landmark, the less consistent between AP/SI landmark movement can be observed. Even if all R^2 values for L1, L2, and L5 within the lower thoracic cavity are not high, there tends to be less intra-cycle variation in landmark 3 (L3) and landmark 4 (L4).

Interestingly, L5 travels in a roughly linear path, hinting at the potential correlation between the two directions (SI/AP), and the correlation would not be counter to the construction of a motion-compensated model. The paths of the other landmarks show typical hysteresis with an elliptical trajectory. Among them, L4 displays the strongest hysteresis, demonstrating that the phase between the two directions (SI/AP), has a 50% delay. The different pathways of inhaling and exhaling for these landmarks may challenge the respiratory model due to phase incoherence in the AP axis. Hysteresis effects typically lead to a phase difference. Phase shift analysis along the SI axis was accessed between Seg. 5 and the landmark trajectories, which, as was the case for the surrogate, were manually selected at the end-of-exhale point.

Moreover, there was no statistical significance in phase shift with Seg. 5 in four of five landmark trajectories (with the exception of L2, $p < 0.01$, remaining trajectories had a mean of $p = 0.36$, T-test), whereas the mean phase shift for Seg. 5 was 0.03 and 0.01 s for L4 and L5, respectively. It was assumed that the motion of these landmarks largely corresponded with abdominal surface movement. However, the phase difference varied highly in the AP axis. All of the landmarks in SI movement demonstrated strong correlation with Seg. 5. The mean directional phase shifts of all landmarks in the SI axis were phase-matched with the Seg. 5 signal within a smaller shifting time than the rate frame error (0.25 seconds). By contrast, the AP phase of Seg. 5 was faster (AP movement occurs earlier than SI movement) and was coupled with a large phase delay from target landmarks. Moreover, this result showed strong linear regression in phase shift in a given situation ($R^2 = 0.39$ and 0.96 with and without L5, respectively, with ordinary least squares method). This result was not conclusive, and thus investigation of how the phase shifts in relation to the two directions (SI/AP) is worthy of further analysis.

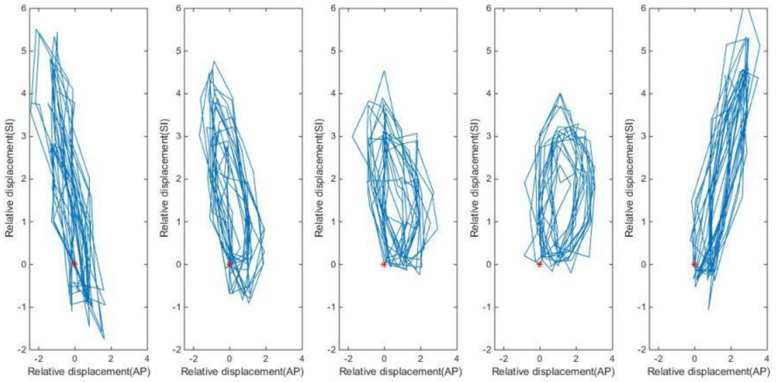

Figure 1.10: An example of the continuous trajectory of five target landmarks within a volunteer. The trajectories were a wide variety of shapes, consisting of both wider (L2, L3, and L4) and narrower (L1 and L5) elliptical trajectories. The trajectories matched with the R^2 in Table 1.1. The lesser R^2 value led to a circle-like trajectory, indicating more hysteresis.

Moreover, there was no statistical significance in phase shift with Seg. 5 in four of five landmark trajectories (with the exception of L2, $p < 0.01$, remaining trajectories had a mean of $p = 0.36$, T-test), whereas the mean phase shift for Seg. 5 was 0.03 and 0.01 s for L4 and L5, respectively. It was assumed that the motion of these landmarks largely corresponded with abdominal surface movement. However, the phase difference varied highly in the AP axis. All of the landmarks in SI movement demonstrated strong correlation with Seg. 5. The mean directional phase shifts of all landmarks in the SI axis were phase-matched with the Seg. 5 signal within a smaller shifting time than the rate frame error (0.25 seconds). By contrast, the AP phase of Seg. 5 was faster (AP movement occurs earlier than SI movement) and was coupled with a large phase delay from target landmarks. Moreover, this result showed strong linear regression in phase shift in a given situation ($R^2 = 0.39$

and 0.96 with and without L5, respectively, with ordinary least squares method). This result was not conclusive, and thus investigation of how the phase shifts in relation to the two directions (SI/AP) is worthy of further analysis.

We observed a strong relationship between abdominal movement (Seg. 5) and internal SI motion. Linear regression analysis revealed a strong relationship between the Seg. 5 (Pseudo-RPM) signal and landmark motion in the SI axis, although their displacement variation was not large (<2mm).

When all the data were combined for analysis, the first-order linear regression (R^2) value was 0.90, and the SI motion in the thorax, which corresponded highly with the abdominal muscle, was driven by the diaphragm. This outcome provided a positive confirmation that monitoring the abdomen is an appropriate approach for determining the source of a surrogate. It is encouraging that the greatest directional movement, in the SI axis, can be well-correlated. In the AP axis, the R^2 value for L4, 0.07, approximated to zero while the R^2 value for L5, 0.68, showed a moderate regression. The low mean R^2 value of 0.18 can be considered a non-relationship for these combined data.

The gradient of surrogates revealed a considerable potential for use as additional signals. By following Low’s idea (of making use of a signal with its time deviation), the gradient of (Seg. 5) pseudo-RPM lifts the mean R^2 value to 0.55 with landmark AP movement (Table 1.2). L3 and L4 showed a weak linear relationship and provided a large improvement by Seg5-G (>0.6). L5 goes a specific spot of all, which only decreases the R^2 value with the pseudo-RPMs gradient (between Seg5 AP to Seg-G). From another viewpoint, hysteresis is an inevitable challenge in motion

R^2 value	L1	L2	L3	L4	L5
Seg5 (SI/AP)	0.88/0.24	0.91/0.12	0.91/0.07	0.90/0.00	0.89/0.49
Seg1 (AP)	0.53	0.38	0.3	0.06	0.1
Seg5-G (AP)	0.33	0.59	0.71	0.81	0.33

Table 1.2: R^2 value of the linear regression of surrogate and landmark trajectories.

modelling because of the different forces that occur during the breathing cycle. Hence, the use of only a single surrogate input is insufficient. Linear regression analysis was also performed to assess the relationship between Seg. 1 and thoracic movement, which may become a surrogate with the use of a thoracic belt. The R^2 value was 0.41 for the AP trajectory. A weak correlation, average $\boldsymbol{R^2}$ as 0.27, was found between Seg. 1 and all AP axes

Using landmarks in frame 6 as location benchmarks, the mean 2D Euclidean, superior-inferior, and anterior-posterior distances of all target landmarks were 2.64, 2.05, and 1.32 mm, respectively, and the maximum displacement of all the landmarks was 6.82, 6.22, and 4.47 mm, respectively. Table 1 lists the basic displacement information of target structures. Furthermore, the value from the linear regression of the AP/SI path was used to judge the hysteresis of target landmarks. If no hysteresis exists, the R^2 value should approach 1.

1.4.3 Image registration

Image registration presents the outcome of internal motion. The quality of the registration has a critical influence on motion modelling. In this study, the image registration used frame 6 as a reference image, which was the end-of-exhale point, which is considered less location variance than other breathing phases. The image registration conducted for the first 100 frames provided the training frames to obtain the internal motion vector fields. We focused on the internal motion of the lungs and evaluated the results according to the target registration error.

Because of susceptibility effects, the boundary between solid tissue and air introduced noise to the images. Fortunately, L1 exhibited an excellent correlation with Seg. 5, as well as less hysteresis, which might overcome the leading error from the registration; 16% of the registered error was beyond the pixel size for L1, whereas there were no errors larger than this for the other landmarks. There was a significant registration error in various direction s for L1 ($p < 0.01$,T-test). For group analysis, the test results were significant ($p < 0.01$,ANOVA) for both the 2D and 1D error of L1 and other landmarks, whereas we found an undistinguished difference ($p = 0.02$, 0.02, and 0.03 for 2D, SI, and AP, respectively,T-test) when we excluded L1. A possible reason for the larger registration error is the location of L1 extremely proximal to the diaphragm.

The registered error was phase-dependent. In Fig. 1.11, the red dots indicate when the 2D error became larger than the pixel size (0.94 mm). There seemed to be a tendency for most of the significant errors to occur at the beginning of exhalation, coupled with 15 of 16 large error frames of L1. However, this was only observed for the first 15 seconds and may have resulted from an irregular breathing cycle during the initial period of acquisition.

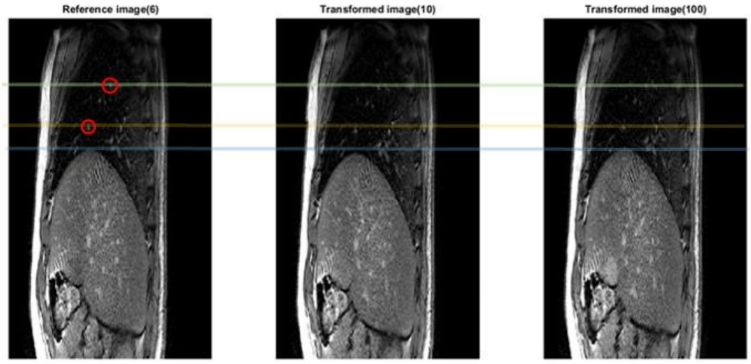

Figure 1.11: Images of the registration results. The transformed frames 10 and 100 are shown. Three horizontal lines are used to visualise the accuracy of the registration. Slight mismatches for the diaphragm (blue line) can be seen. L2 (yellow line) and L4 (green line) aligned with the correct expectation. The modelling results were not homogeneous.

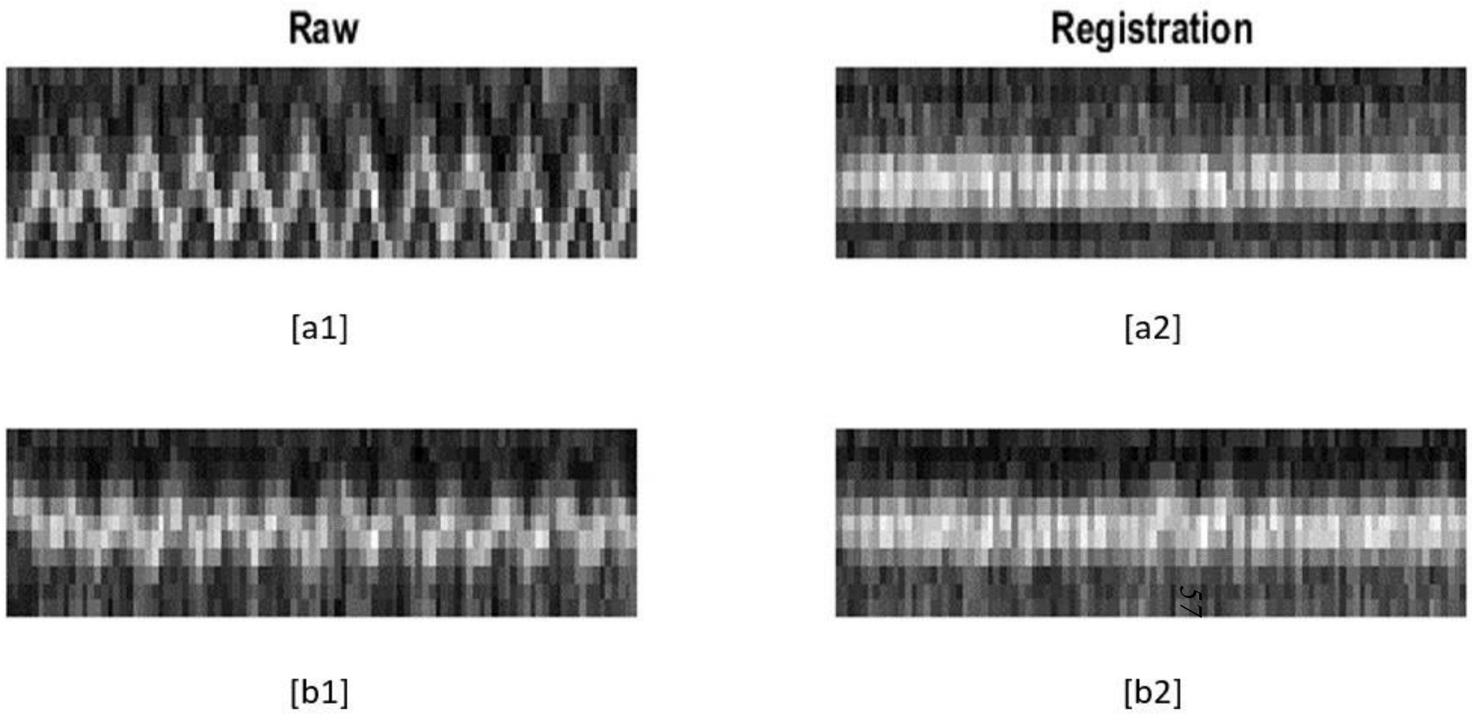

Figure 1.12: Examples of registration images for L1. Images were re-binned in a single dimension (SI or AP axis) across time. A clear semi-periodic change of L1 was noticed in both SI [a1] and AP [b1]. If registration was conducted perfectly, the re-binned images formed a straight line without a visible shift. However, the small ripple in the middle of the SI registration image [a2] implies that the target landmarks were misaligned. Such an effect was also visible in corresponding frames of the AP image [b2].

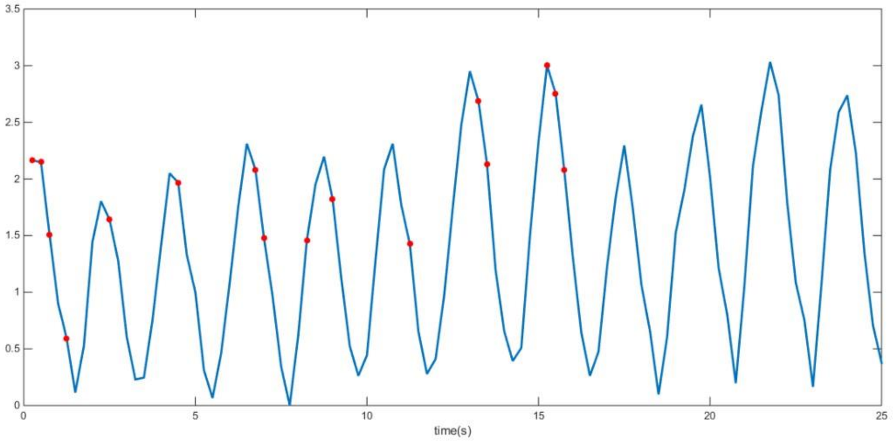

Figure 1.13: The error is greater than the pixel size with the surrogate signal (> 0.935 mm).

1.4.4 Motion model estimation

There were four surrogate signals (OLS-1, OLS-1G, OLS-5, and OLS-5G) with three correspondence approaches (OLS, PCR, and PLS) for the evaluation of the motion model. The last 200 frames were for the assessment of the five selected landmarks. Table 1.3 presents the error of landmarks between test frames and estimation of models. To evaluate the mean errors between different surrogates, regression approaches, paired t-tests, and one-way analysis of variance (ANOVA) with a strict significance level of 1% ($p < 0.01$) were conducted by pairing or grouping landmark-variated mean values.

Model	None	OLS-1	OLS-1G	OLS-5	OLS-5G	PCR	PLS
2D	2.86± 6.71	1.19± 3.54	1.04± 2.62	0.99± 2.93	0.77± 2.72	0.74± 2.64	0.74± 2.64
SI	2.15± 5.48	0.41± 1.69	0.33± 1.4	0.6± 2.7	0.52± 2.18	0.5± 2.09	0.51± 2.09
AP	1.53± 4.47	1.03± 3.53	0.94± 2.62	0.68± 2.88	0.48± 1.79	0.46± 1.72	0.46± 1.72
t%	4.9±4	45.5±6	43.7±15	52.4±11	69.3±22	70.7±24	70.7±24

Table 1.3: The mean Euclidean 2D error, SI error, and AP error for each of the different models evaluated (in mm) and target compensated period (%).

Briefly, the input surrogates with gradients and advanced regression approaches resulted in improved motion estimation. The results of all approaches reported in Table 1.3 show the potential of using a gradient as a surrogate, a high-dimensional surrogate signal, and varying multivariate regression methods. Most illustrative of this fact is the comparison of OLS-1 (as the common used surrogate signal, like RPM system) with other surrogate signals. The following section discusses different variables. First, the simplest approach, OLS-1, effectively ameliorates motion estimation in a 2D and SI axis with 58% and 80% improvements with non-fit data, respectively, but shows a limited improvement in the AP axis of 32%. A 2D maximum error produced a similar result to that of AP, suggesting that the overall 2D error was reduced along with AP because of the minimal SI error observed. The majority of the estimated errors were associated with a correlation between the landmark's path and the surrogate signals. For this section, an extreme R2 value (0.9/0.18) for the pseudo-RPM in the SI and AP axes associated with the OLS-1 result was noted. Therefore, it can be supposed that if the target tumour displays motion in a single axis motion (craniocaudal displacement), one channel is sufficient as an abdominal belt surrogate for dynamic correspondence.

The selection of the input surrogate plays a crucial role in overall modelling. Because there was more surface information, the overall error was marginally reduced. The OLS-5 generally compensated more than the signal region source, OLS1, by fitting a setup goal in the AP axis. The 2D and AP errors required more effective management because their errors (of 68% and 56%, respectively) increased in tandem with non-fitting data. The accurate estimation contributed to a relatively strong regression, which may have come from Seg. 1 along the AP axis. Seg. 1 shows a better correlation in Table 1.2. For displacement signals alone, full skin monitoring is a superior type of management than using a single source.

In addition, over-fitting seemed to enhance the SI error. Because the total number of surrogates was not large (n=10), over-correlation did not greatly impact the overall error. This could also explain the growing maximum SI error in OLS-5, preventing the complete application of the pure displacement surrogate signal. This effect was assumed to become more evident as the full skin source was separated into more signal sources; that is, increasing total system dimensions. In an opposite scenario, however, a thorax-dominant breathing volunteer may require a change of viewpoint and region of interest when the experiment was being designed. Moreover, if the respiratory phase does not mismatch between the thorax and abdomen, the degrading degree of freedom would not only result in a poor AP assessment but also a stronger over-fitting effect.

The gradient is capable of compensating for AP motion. By pairing non-gradient signals with gradient-involved groups, it was evident that the original signals (with gradients) accounted for all 2D estimations by effecting significant compensation in the AP axis. All directional errors decreased; among them, OLS-1G was the simplest input surrogate (possessing two degrees of freedom) that was able to cope with AP movement. This also shows that a non-imaged surrogate using spirometry or an abdominal belt with a 1D signal can still address the hysteresis problem by adding a time deviation factor to the surrogate signals. This conclusion was similar to the one arrived at in Low's report. In an OLS-5 group, OLS-5G improved the 2D error by 22.2% with OLS-5. The AP error in OLS-5G was a crucial finding in this context, minimising the maximum error of all OLS to under 2 mm. Signals with gradients were able to enhance overall motion estimation efficiently. For reduced-dimension approaches with full surrogate signal inputs, limited error reduction improvements were seen. The results of both PCR and PLS showed no statistical significance ($p < 0.01$,T-test). Furthermore, there was no significant difference in either mean errors or maximal errors with the three correspondence approaches used in this work.

As shown in Fig. 1.12, the input portions of the components were extremely similar. However, it seems that low-dimensional systems allowed for the same accuracy as those of high dimension. In this test, the systemic dimensions can be reduced to four in PCR and PLS and maintain a strong overall correlation, whereas to achieve a similar outcome in OLS, ten systemic dimensions are required. Another standard for evaluating different approaches is the target-compensated period, which illuminates an agreement with error estimation. The non-fit landmarks accounted for approximately 5% of the testing time. Because of the significant baseline shift, as shown in Fig. 1.13, the baseline of the respiratory trajectory had drifted, leading to a high error. For the 1D surrogate signal, adjustment of the compensated trajectory reached 46% of the time to reach the target, meaning 46% motion in image series can be compensated; a time that represents more than half of the breathing cycle is impractical for advanced treatment. The best result (for PCR/PLS) would be approximately 70% of the time to reach the target: 55% more time than OLS-1. Although shifts in the baseline caused the trajectory to move from the previous centre, the motion model was still able to cope with the dislocation from the change in breathing behaviour. The target-compensated period strongly agrees with the estimated errors for both 2D and AP (R^2 = 0.91 and 0.92, respectively). The hysteresis dilemma arises predominantly from the phase-pattern mismatch in the AP axis, leading to major uncertainty in the overall compensation. When improving AP movement estimation, more time can result in higher precision. Despite the fact that most landmarks could be targeted, the increasing standard deviation suggested that at least one of the landmarks did not fit with the others. The model became increasingly inconsistent with reduced-dimension regression approaches.

In the SI axis, the phase was prior to that of the general signal, and thus OLS-1G was in advance of the phase of the pseudo-RPM in order to fit its movement pattern. For AP motion, OLS-5 raised its baseline to meet the real conditions. Both of these characteristics vanished for the other surrogate combinations.

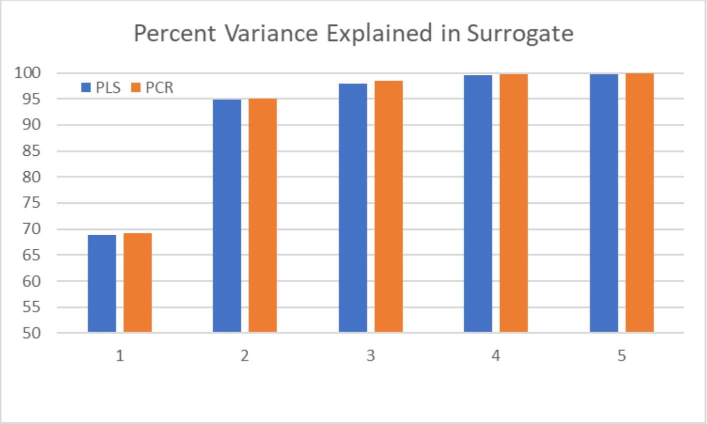

Figure 1.14: Components represent the portion of the original surrogate signals for 5 region inputs with their gradients. When comparing PCR with PLS as an explanation of multiple dimensions, it was noted that there was a small difference between the approaches. The difference for the first four components was less than 1.5%, which is nearly the same value for the first component.

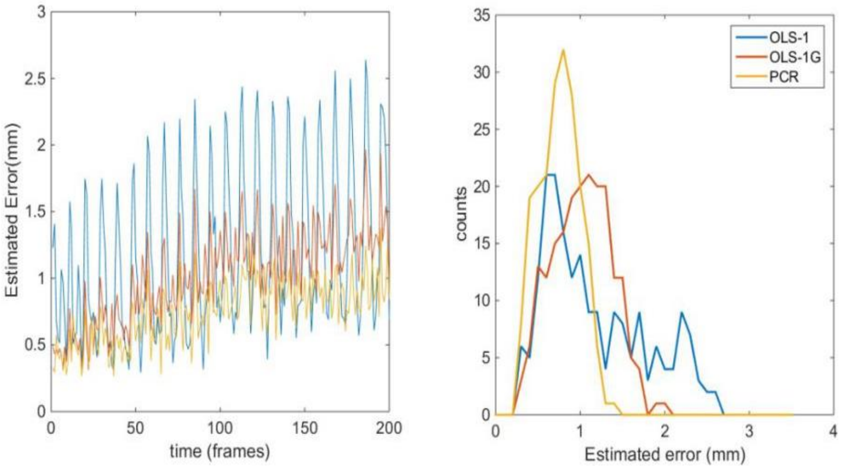

[a] [b]

Figure 1.15: Errors of the three regression approaches. The error of OLS-1 is clearly displayed, as well as motion induced-factors, namely poor comparison with a striking breathing pattern. OLS-1G and PCR gave similar outcomes; the regular pattern was reduced as breathing influence decreased. With more efficient corresponding approaches, the error distribution became increasingly Gaussian (R2 = 0.60, 0.96, and 0.97 for OLS-1, OLS-1G, and PCR, respectively) in Fig. 1.13 [b], which seems to derive from random noise rather than being a poor correlation. When pairing OLS-1G and PCR, the smaller median of PCR was considered to produce a superior estimation.

1.5 Discussion and Conclusion

The motion model is a feasible method for respiratory motion compensation in thoracic and upper abdominal radiotherapy. In this chapter, we evaluated the workflow presented by Wilms' article for motion estimation from a single image source, which relies on image registration and various multivariate regression approaches. Virtual surrogates were used as the input signals, and the virtual surrogate signals generated from the dynamic images ensure that there is no time-shifting between any two modalities. Incorrect time-shifting leads to an uncertain external-internal motion relationship and an incorrect motion model while unforeseen system latency compounds this problem [40].

A rapid breathing cycle in this study was observed from the breathing signals, implying shallow breathing of the subjects as opposed to spontaneous breathing. The relationship between the surrogate internal landmarks may not be typical; this condition has seldom been reported in previous research. Lee [41] reported that the correlation between internal and external motion changes when subjects' breathing changes from free-breathing to biofeedback-guided breathing. In our study, the breathing cycle was found to change across the scanning session, as shown in the frequency spectrum; such a rapid breathing cycle may be explained by the MR coils the subject was wearing. The accuracy of motion estimation depends on the accuracy of the training data.

In our study, the correlation between virtual surrogate signals and the selected landmarks is in agreement with previous research [32,33,41]. A very strong correlation between abdominal movement and internal SI motion and a relatively strong correlation between thoracic movement and internal AP motion were observed, and these findings represent strong motives for the acquisition of both thoracic and abdominal breathing signals.

The signal gradients permitted a large improvement in correlation with the axis. This finding agrees with Low's idea that motion compensation can be achieved with a 1D surrogate signal with its time deviation. In his study, input surrogates are used, namely volume and flow from a spirometer. Wilms presented a comparable idea to a 1D signal in the form of a time derivative. The reported differences in motion estimation are statistically significant ($p<0.01$,T-test) compared with estimation using the 1D signal alone. Without the whole-surface image, the current surrogate systems (RPM, belt, and spirometry) are able to compensate for internal motion.

This study highlighted the importance of multiple input surrogate signals as the solution for the estimation of hysteresis. The difficulty in the correlation of hysteresis derived from the respiratory phase mismatch between surrogate signals and target landmarks. Non-single-channel surrogates can reduce estimation errors at different levels according to how the secondary surrogates correlate with the internal AP path of the landmark. This concept has been proven is that the usage of displacement and gradient perform a good internal estimation with the motion model [42].

Both signals with time deviated (gradient), and full skin-monitoring could compensate for AP movement as well as improve overall estimation by providing more corresponding information about internal motion and systematically increasing the field of view (FOV). However, many similar surrogate signals for correspondence may lead to over-fitting, which generates adverse effects such as increasing the maximum overall error. Proper control over the number of systemic dimensions is another critical issue for multiple surrogate input motion models. This

Figure 1.16 shows an oblique ellipse with a positive rotation of the trajectory of the L5 angle, whereas the other four landmarks are analogous to an ellipse with negative rotation. The landmark on the elliptical trajectory moved anticlockwise, meaning that the phase in the AP axis changed faster than in the SI axis. This phase mismatch could cause poor compensation because the pseudo-RPM had the smallest phase of all in this test, as shown in Fig. 1.15. This finding illustrated the importance of including different types of trajectory when modelling internal motion.

The reduced dimension approaches can effectively reduce estimation errors, although the nature and magnitude of the errors across different approaches were not evident. Nevertheless, one particular finding was that the motion of the AP motion was earlier and the movement of SI in L5 did not correlate well with the compressed dimensions. Only surrogates with a gradient of more than one dimension can address this type of path.

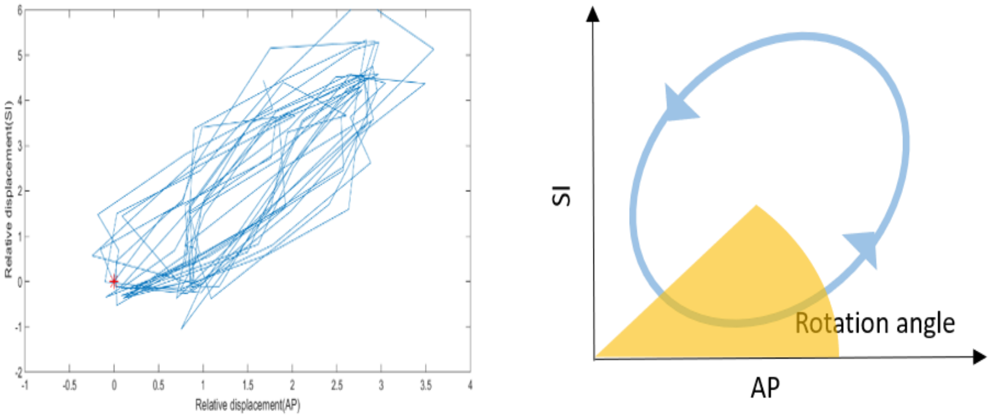

[a] [b]

Figure 1.16: Demonstration of the trajectory of L5 (in mm). The red star in Fig 1.14 [a] marks the location of frame 6, the reference spot for the whole test.

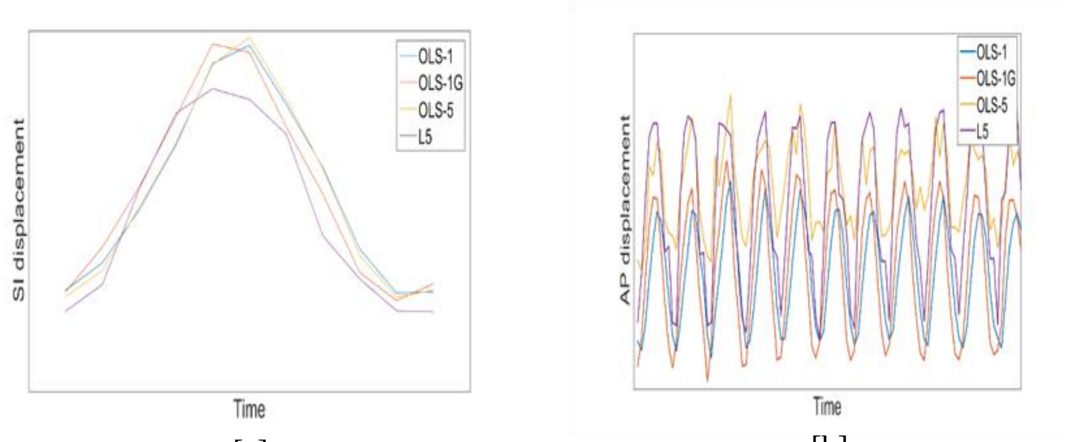

[a] [b]

Figure 1.17: Example of the movement of L5. Violet lines are the true trajectories in both directions. Fig. 1.15 [a] shows that the real phase arrives earlier than that of the surrogate signals; hence, OLS-1 and OLS-5 cannot simulate a realistic breathing pattern. OLS-1G brings a gradient signal with a smaller phase than the displacement signal, which successfully moves a full cycle ahead. However, this property did not appear to be unique to OLS-5G and PCR/PLS. During AP estimation, a very large shift in the baseline was a problem. This data did not reveal sufficient useful information about the abdominal region to allow the full skin surrogate to complete the depicted movement.

The major limitation of this study is it is a single case report and is therefore not representative of the clinical evidence of the nature of the population at large. Furthermore, the number of surrogates was insufficient to induce noticeable over-fitting events, and the number of surrogates will highlight the largest difference between OLS and PCR/PLS, which was not clearly revealed in our work. In addition, the intra-variance analysis could not be performed because single images were acquired.

We assumed that the difference produced by each approach would be evident. Our future work will extend to both volunteers and patients as well as developing a subpopulation model. However, this aim would require the development of an advanced respiratory surrogate device. Although our results indicated that most of the surrogates considered here are equally suitable for motion estimation purposes, patient-specific differences exist. Therefore, surrogate simulations and the proposed framework could be used to determine optimal patient-specific surrogates (and positions) during treatment planning.

This study revealed that using the entire surface surrogate with advanced regression approaches is feasible for the compensation of respiratory motion, but a location-specific trajectory (L5) was also observed. Therefore, the breathing signal with gradients was used to determine the optimal surrogate source for internal motion compensation.

.

Chapter 2

A novel approach to evaluate the effect of personalised vocal instruction on the regularity of respiration

- **Publication**

  Chuang, C. S., Xu, R., Li, X., Royle, G., Fan, J. Bar, E., & McClelland, J. A¨ novel approach to evaluate personalised vocal instruction on the regularity of respiration. *In preparation*.

- **Conference presentation**

  Chuang, C. S., Xu, R., Li, X., Royle, G., & McClelland, J. (2018). OC-0525: An evaluation of vocal instruction for external respiratory motion using kernel density estimation. Radiotherapy and Oncology, 127, S277S278.

Research aims and contribution

- To develop a cheap contactless image system to monitor respiratory surface movement with clinical accuracy. The system has to meet the following requirements: the camera has to be easy to set up, and the set up involves no time costs for treatment rooms; the breathing waveform must be fully recorded without any breaks to represent the continuous breathing signals, and the total costs of the setting up of this new system should be much lower than currently available clinical products.

- To compare the variations in breathing patterns between free-breathing and vocal-coached subjects. The interaction of thoracic and abdominal breathing signals must be easily observed, which means that the observers should be able to distinguish the variations of breathing patterns. The different breathing patterns can be quantified for further analysis and comparison.

- To evaluate the feasibility of adapting personalised vocal instructions for respiratory regularisation. By following the result of the aim in the previous paragraph, the vocal coaching methods should result in a higher similarity across daily breathing patterns. The quantitative result across different recording days reveals the feasibility of vocal coaching.

I worked together with a radiation oncologist at Shenzhen People’s Hospital to develop an efficient method to regularise the variation in intra-breathing cycles in the clinical environment, spending about a full year, including five months in the clinical area for data recording, at the department of radiation oncology of Shenzhen People’s hospital and assisting in the development of an economical and accurate breathing motion management method. I was involved in the development of surrogate systems and the recruitment of volunteers from Tsinghua University. I also recorded the breathing sessions of both volunteers and patients and tested the developed surrogate system using a low-cost depth camera (Kinect).

The novelty of the work

The investigation of the influence of vocal instruction by whole-surface monitoring presents the first combination of vocal coaching and a contactless surrogate system with a biofeedback approach. It has been proven that breathing variation reduces with biofeedback methods, but this technique is limited by its long setup time. To overcome the time-consuming preparation of wearable devices in the visual feedback approach, this study presents a complete contactless biofeedback system. Specifically, there is no wearable device or marker placement during either recording or audio-guiding. This method allows treatment-room operation at full capacity while reducing the uncertainty of respiratory motion.

2.1 Rationale

This work aims to investigate an optimised method for stabilising respiratory motion as an irregular breathing motion has a negative influence on treatment planning

[2][3]. In order to improve treatment quality, respiratory regulation procedures were introduced during the treatment process. Among all motion management methods, biofeedback received particular attention due to its simplicity and straightforwardness. Patients were able to follow visual and vocal instruction to breathe during imaging and treatment sessions, with the aim of reducing the variation of respiratory motion from one session to another.

A major concern with regards to biofeedback is the time consumed by the setting up of the monitoring system and patient training, which negatively impacts its feasibility in the treatment room. Another concern is that currently available commercial respiratory monitoring products are relatively expensive and difficult to install in the treatment room. There is also a lack of knowledge about external respiratory signals, and at present, the signal is usually acquired from a single area, such as the abdomen or thorax, which may not be sufficient to describe the entire motion of areas surrounding the tumour.

The study introduces a rapid-setup vocal-coaching approach in a clinical environment. To expedite the setup time, a contactless camera, which is a commercial product for entertainment, was used to monitor movements from the entire skin surface and overcome the limitation of a single signal. By following the computer-generated personalised breathing waveform, patients were able to follow vocal instruction to guide them on how to breathe and improve respiratory regularity. Furthermore, since patients were guided by vocal sounds rather than virtual reality goggles, which was applied for visual feedback, the positioning time for each patient should be reduced, and the number of patients accommodated in each treatment room should be maximised. The results of this study may be beneficial to hospitals, as well as patients.

2.1.1 Vocal coaching

Respiration-driven organ motion is a critical concern in radiotherapy. Current technical solutions for respiratory motion compensation are 4DCT [5,12,43], respiratory gating [22,44], and DIBH [8,9], as reported by the American Association of Physicists in Medicine Task Group 76 [11]. However, most techniques rely on the assumption of the reproducibility of the breathing cycle. The variation of intrafractional motion results in image artefacts for 4DCT [44], cone-beam CT [45], and PET [46]. For the day-to-day variability in motion, discrepancies in variation lead to a large margin of error or unwanted dose distribution, and regularising the breathing cycle can reduce these discrepancies.

Venkats approached this idea by combining a personalised breathing waveform [47] with audiovisual biofeedback. With the RPM system, the breathing waveform of a specific patient was captured, and a personalised waveform was computed to guide the patient’s subsequent breathing by following the audiovisual biofeedback system. The patient viewed a path on the screen and heard ascending, and descending tones played, which represented inhaling and exhaling, respectively, to guide them on how to breathe. The results showed a root mean square displacement of 0.08 cm and periods 0.2 s longer than in the target waveforms, whereas, with free-breathing (FB), the root mean square displacement was 0.016 cm with periods 0.77 s longer than in the target waveforms. The paper concluded that biofeedback with personalised waveform reduces variation in breathing.

More studies have concluded that the biofeedback approach is feasible. Yu [48] investigated the difference between the audio- and visual-only feedback. The results showed that there was no significant difference between the methods, implying that the audio-only mode has clinical potential because it is more time-efficient. Baba [49] made use of an electronic metronome to instruct volunteers. Their research applied the concept of personalised instruction of a given individual’s breathing cycle. The instructed cycle was derived from the mean FB cycle for each individual. This personalised audio coaching improved breathing cycle stability within the volunteer group. To apply the visual feedback method, the installation of visual devices such as virtual reality goggles or reflection mirrors is required, which may be challenging for some departments with high patient throughput. Several approaches can be found in the literature addressing irregular respiratory motion with breathing guidance, audio and/or visual feedback technique (e.g., the overview by Pollock [50]). However, the same limitation existed as in the aforementioned studies in that the RPM system only presents 1D signals.

Feedback requires a breathing signal as the surrogate, and one of the surrogate signals is acquired from the surface motion of the abdomen. Commercial surface imaging devices are generally expensive and thus, to reduce costs, some groups have investigated the use of the Kinect camera. The University of Surrey has performed a series of research studies on this topic and have shown that the Kinect performed similarly to other surrogate systems [51,52] but generated multiple signals from the breathing movement of the thoracic-abdominal surface. Dual Kinect systems for whole-surface imaging were also investigated to reduce the artefacts of PET imaging [53].

The aforementioned studies only applied single signals as surrogates—predominantly the abdominal displacement signal. No research has been performed to investigate the correlation between multiple surface signals and changes in their relationship during breathing.

Lee presented systemic biofeedback with personalised waveform studies [39,40,55]. The main breakthrough of these studies is the application of internal images. The same experimental framework was performed in each study where the breathing patterns with RPM for FB were recorded for the volunteers. The individual-specific guiding waves were then computed and displayed on a reflecting mirror, and the respiratory paths were followed. The benefit of visual feedback is twofold: first, the correlation between abdominal movement and 2D tumour motion improved by 11% with visual feedback (absolute mean correlation = 0.59), which was higher than the correlation obtained with FB (absolute mean correlation = 0.53). This finding implies that the superior model motion can be achieved with a higher external-internal correlation. Second, the visual feedback improved intra-fraction tumour motion consistency by 34% in displacement (0.2 cm and 0.13 cm in FB and feedback, respectively) and by 73% in periods (0.98 s and 0.3 s in FB and feedback, respectively) when compared with FB. Regarding interactional differences, visual feedback improved tumour motion consistency by 42% in displacement (0.11cm and 0.06 cm in FB and visual feedback, respectively) and by 74% in periods (data not presented) when compared with FB. These outcomes reveal the effectiveness of using biofeedback methods for breathing stabilisation.

Lee performed a series of studies to demonstrate the advantages of applying a personalised waveform to guide each individual, but the study outcomes were foreseen as it was well known that there is a high correlation (a CC of up to 0.9) between abdominal movement and SI tumour motion, as presented in previous research [32, 56]. The improvement of correlation in the SI axis may be redundant since a poor correlation still existed between the abdomen movement and the AP axis of internal motion when the biofeedback method was used. Therefore, the performance of 1D surrogates is limited even with patient-specific biofeedback.

This chapter investigates the variation of 2D breathing signals by instructing volunteers to follow a vocal coaching technique and presents a novel method for evaluating the impact of breathing guidance by analysing two external breathing signals—one corresponding to the abdomen and the other to the thorax—as well as the relationship between the two signals. This is based on the hypothesis that the motion of the tumour and other internal anatomy is affected by both abdominal and thoracic motion. Therefore, a more consistent relationship between the signals implies less variability in internal motion, whereas a more variable relationship between the signals implies more variability in internal motion. This study assesses the impact of audio coaching on both volunteers and breast cancer patients who were treated at the Shenzhen People's Hospital in China.

2.2 Materials and Methods

2.2.1 Respiratory monitoring system setup

- Select surrogates

The source of external movement relies on the selection of the surrogate system. The RPM system is a common option for processing this type of study, but it only delivers 1D signals, normally from the displacement of the abdomen. Since the use of both thoracic and abdominal movement is more accurate for motion models as a result in Chapter 1, the surface scanner was our first choice.

Due to the rapid development of optical devices over the last few decades, full skin monitoring has generated much interest among researchers, and this approach has advantages in regards to multiple signal inputs and patient cooperation. Hughes [27] noted that signals from the VisionRT stereo camera are strongly correlated with signals from a spirometer, showing that surface monitoring may become another potential surrogate system. In 2010, a breakthrough product, the Xbox Kinect, which is a low-cost infrared camera that uses stereo structure light measurement, was released by Microsoft. Systemic research studies that demonstrated positive outcomes of using the Kinect have been conducted by the University of Surrey [51,57–59], constituting further evidence that the Kinect is in good agreement with other surrogates (e.g., the RPM).

Moreover, the skin surface can be divided into abdominal or thoracic regions by Eigen images to simplify complete signals. Such information may be used to inform the development of motion correction and motion estimation strategies in diagnostic and therapeutic imaging. When evaluating the accuracy, most Kinect tests are on static objects, and there had been case reports showing that environmental lighting or texture of surfaces may have an adverse effect on Kinect readouts. Therefore, there is still a concern that errors may be enhanced when working in an exam room. To solve this problem, an additional aim of this project was to combine the Kinect with other modalities to transform it into an effective surrogate device.

In this study, surface displacement was measured from the surrogate signals for the detection of internal motion. Surface measurement was performed using the Microsoft Kinect V2, which has been validated as a highly accurate depth camera with considerable coverage. The latest model of the Kinect is a time-of-flight camera, capable of measuring the distance by measuring the phase shift between emitted and reflected infrared light. The Kinect performed with a measurement error of 0.1 mm in a range of 0.8 to 1.2 m from the camera. The advantages of using the Kinect are its low costs, mobility, and capacity for contactless measurement. Five healthy male volunteers and six post-mastectomy female patients were enrolled in the study, and all subjects were asked to remove their clothes and place their arms under their heads to reduce the influence of the infrared signal reflected by the texture of their clothing. The patients were referred from the calibrated oncologist. This study was approved by the ethical committee and local government. The Kinect V2 was placed on a tripod approximately 100 cm obliquely above the subject's surface. Studies have shown that the measurement error is minimal, less than 1 mm, at this range [58].

2.2.2 Breathing recording sessions

Comparing FB with experiment design sessions is a critical task as the results reflect the feasibly of breathing control approaches. Each volunteer went through

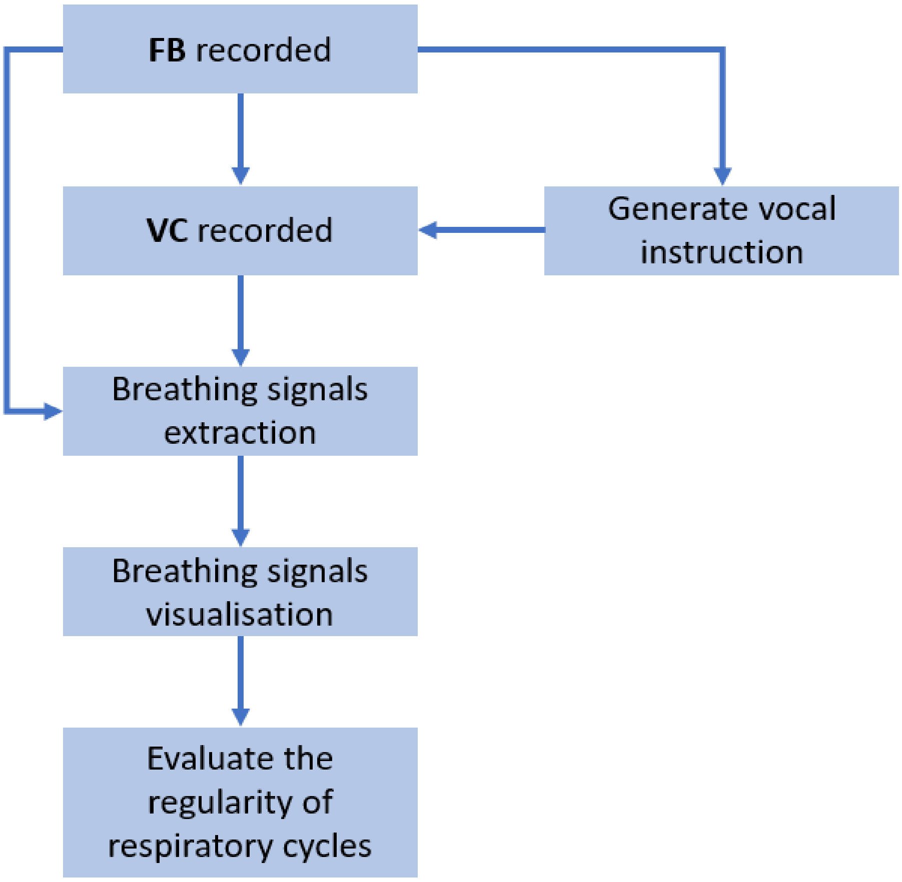

Figure 2.1: Workflow of the personalised vocal coaching evaluation

two types of sessions, free-breathing (FB) and vocal coaching (VC), on the same day for three recording days within a week. Every recording day, volunteers went through the two breathing sessions in a fixed order, first FB, then VC. In the FB session, the volunteers were told to breathe freely, as if they were at rest, for 4 minutes, which was a sufficient duration for their breathing cycle to achieve a relaxed rhythm (R). This was based on the assumption that people breathe more regularly when they are relaxed. In the VC sessions, the volunteers received customised computer-assisted breathing instructions. They received one VC sessions (VC1) on the first day and two VC sessions (VC1 and VC2) on the second and third days. The vocal instructions for VC1 were generated using the average breathing cycle from the FB session of the first day; our study found that number of inhales and exhales were unequal for most of the volunteers. For VC2, the vocal instructions were generated using the FB signals of the same day. The purpose of the different VC sessions is to investigate the robustness of the breathing pattern following VC1. To minimise the inconvenience of the patients' treatment, the recording workflow for patients was simplified to achieve a duration of only two days. Patients only recorded one minute FB each day for two days and one minute VC for one day. The respiration recording scheme is shown in Fig. 2.2.

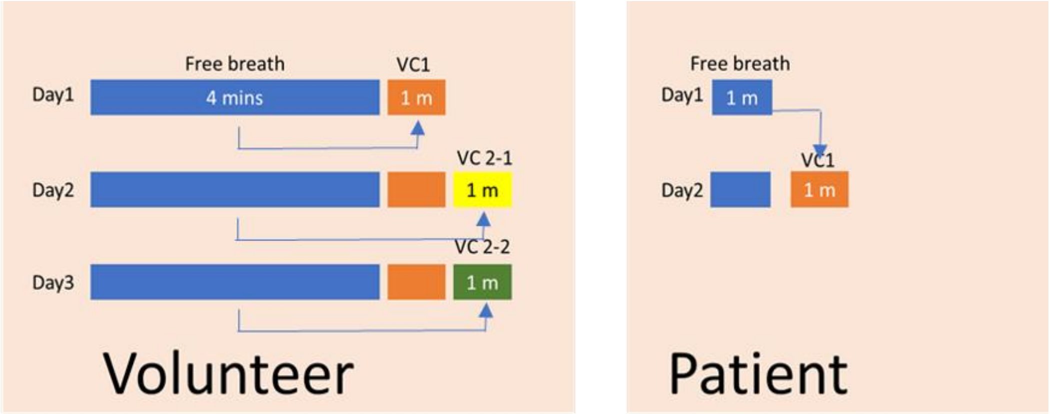

Figure 2.2: Schematic of the recording workflow for volunteers and patients. The volunteers received 2 VC sessions on Days 2 and 3. VC1 (orange) was the instructions generated following the Day 1 FB. The instructions of the VC2 series (yellow and green) was generated from the FB on the same day. Specifically, VC2-1 was created from the FB session from day 2. The simplified patients' protocol was reduced to 2 days.

2.2.3 Signal extraction

In contrast to other studies [11], the surrogate signals in this study could be used after experiments, and the recorded data were serial frames of the depth image. To reduce the variation in the breathing signals, the manual region of interest (ROI) selection was not considered. Furthermore, the primary aim was to compare both abdominal and thoracic signals internally between various conditions, so post-processing was necessary. The presented workflow in Fig 2.3 was adopted from Tahavoris' work [58]. To extract the breathing signals from the Kinect images, the following workflow was applied.

1. Image acquisition: Image collection was performed at 30 frames per second. Each

pixel in each frame contained the distance from the Kinect to the subject's surface, as illustrated in Fig. 2.3[a]. This is referred to as the depth image.

2. Background subtraction: Because of the experimental setup, the Kinect required daily repositioning, leading to a subtle setup mismatch. To handle this problem, background scans (in which no subject was present in the room) of 500 frames (16.7 sec) were collected before the daily experiment and averaged to form a background image. The background image was subtracted from the first frame of the subject's depth image to create a subject mask, as illustrated in Fig. 2.3(b). This mask was applied to all depth images, thereby ensuring that volunteers and patients were the only objects in the depth image for further analysis.
3. ROI: To measure thoracic and abdominal movement, ROIs on the subject's surface were manually selected. The rectangular ROIs on the surface image were placed within a range from the armpits to the hips to capture both movements, as illustrated in Fig. 2.3 [a]. From the first principal component, PC1, the scale of motion on the surface could be displayed as the value of the first PC in each pixel, also known as the Eigen image (Fig. 2.3[c]).
4. PCA: For the first 1800 frames (60 seconds) of FB data, each pixel inside the mask (Fig. 2.3[b]) was realigned into a 2D matrix (distance-time). To extract the highest variance of motion for each pixel, PCA was performed on the 2D matrix.
5. Binary segmentation of PC1: Subsequently, the first Eigen image was segmented into two zones using Otsus' method (binary segmentation) [27]. Otsus' method performs binary segmentation by separating the histogram of the target image's grayscale. This way, it is possible to separate thoracic and abdominal motion. From the binary segmentation, a mask was created (Fig. 2.3[d]) and applied to the collected depth images.

Breathing signals: To extract the breathing curves from the processed depth images, several further steps were required. First, each pixel of each frame was subtracted from the corresponding pixel value measured in the first frame. This way, each pixel represented the displacement from frame 1. Second, the displacement per frame was averaged for thoracic and abdominal pixels separately. Third, the median of the displacement values (to avoid the baseline shifting from a cough as well as other subtle movements) was subtracted from

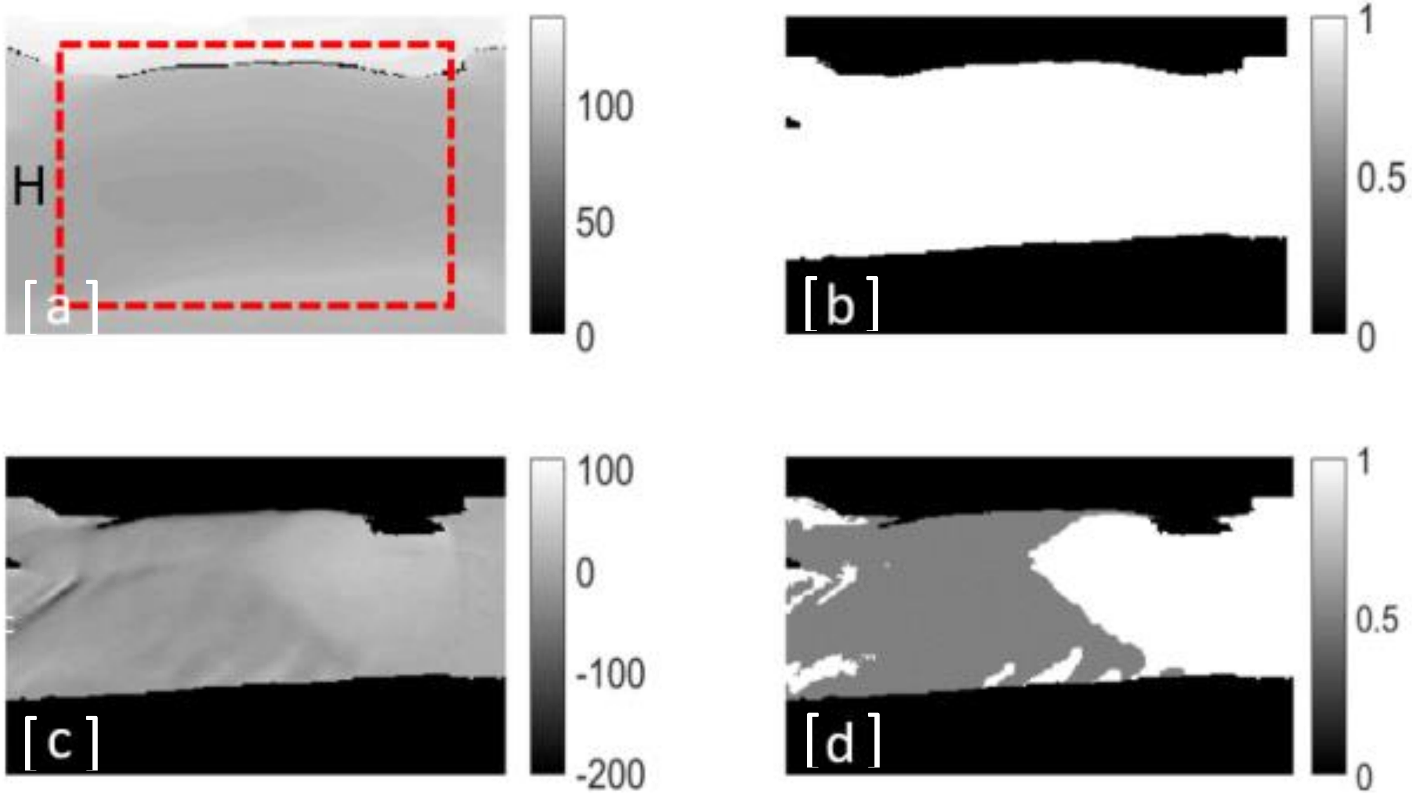

Figure 2.3: Workflow for the image segmentation. [a] A single frame of a subject's surface depth image. The grayscale indicated the distance from the Kinect to the surface. The left side of the image is the head direction. The dashed box indicates the chosen ROI. [b] The mask used for background subtraction. [c] The first Eigen image (PC1) from the first minute (1800 frames) of the FB session, used to segment the motion into thoracic and abdominal signals components. [d] The result of binary segmentation of PC1. The white region (mainly abdomen) represents the major moving part, whereas the grey region is for minor movement (thorax)

6. the two respiratory signals for each session. The signal extraction process was conducted for every session. The final result (Fig. 2.3 [d]) was visually checked to verify the output signals generated from the target region. The optimal mask possessed a clear boundary at the lower rib to separate the thorax and abdomen.

2.2.4 Breathing signal comparison between FB and VC

This research introduced new quantitative methods to compare the two breathing signals from different sessions.

2.2.4.1 Assessment of breathing regularity

To assess how vocal instruction improves breathing regularity, we analysed the abdominal movement breathing curve. We chose only to assess the abdominal signal because of it being the major source of external movement for most people during movement and that it is mainly used by other motion monitoring systems. The vocal instructions were generated from the abdominal signal. For all breathing signals, the cycle time was found for each cycle, and the standard deviation (SD) of the cycle times was used as a measure of regularity. Furthermore, we investigated the SD of the displacement of the end-of-inhale and end-of-exhale positions.

2.2.4.2 Evaluation of the relationship between abdominal and thoracic breathing curves

Kernel density estimation (KDE) was used to visualise the relationship between the thoracic and abdominal signals. We followed the procedure proposed by Alnowami [60], which is briefly described here. First, 2D KDE was estimated from the abdominal and thoracic breathing curves. For any displacement x, the KDE is given by

$$f(x) = \frac{1}{nh} \sum_{i=1} K\left[\frac{x-xi}{h}\right]\left[\frac{y-yi}{h}\right] \qquad (2.1)$$

where x_1, x_2,..., x_n (y_1, y_2,..., y_n) are locations on the breathing curves for abdomen/thorax, n is the sample size (7200 and 1800 for FB and VC sessions, respectively), K is a Gaussian kernel smoothing function, and h is the bandwidth of 0.05 mm. The respiratory trajectory was visualised by plotting thoracic versus abdominal PDFs as a colour map for each session. A new method, which was introduced by our team to compare the variation of 2D breathing signals and was presented at the Estro congress in 2018. To evaluate the difference between the two sessions, the Correlation Coefficient (CC) between KDE maps was calculated, which is a great advantage for this method. The probability density functions (PDFs) of the thoracic and abdominal movement were estimated from the projection of the 2D KDE. Comparing with linear interpolation, KDE offers better data smoothing.

For the volunteer group, in addition to the FB, VC1 and VC2 sessions, the resting state respiration, R, was investigated. The R session was derived from the last 30 seconds of the FB session. This was based on the assumption that breathing progresses more regularly when the subject is relaxed. The CC was calculated for the FB, R, and VC1 sessions separately. For each of these sessions, the CCs between Day 1 and Day 2, Day 1 and Day 3, and Day 2 and Day 3 were calculated and averaged. For VC2, the CC between Day 2 and Day 3 was calculated. For CCs with a value close to 1, breathing patterns between the two sessions are similar. The correlation of the breathing pattern between two sessions was evaluated as the similarity of the corresponding KDEs. Due to the simplified patients' protocol and unforeseen incidents in the treatment room, only one session of VC was conducted. Therefore, the difference between the two sessions was not evaluated.

- Mutual information

Mutual information (MI) is a measure of the shared information between two random variables. Liu presented a similar concept for measuring asymmetric chest movement [61]. MI was calculated using the result of PDFs as follows:

$$I\left(X;Y\right)=\sum P_{xy}\log\frac{P_{xy}}{P_xP_y} \tag{2.2}$$

where P_x and P_y are the PDFs from the abdominal and thoracic movement, the projection from the 2D KDE. P_{xy} describes the joint probability distribution. In this study, the relationship between two breathing signals (KDE) is more consistent. The altered phase-shifting between two signals, the changed baseline and varied amplitude of breathing cycle increased the variation in two signals, indicating a broad KDE. Following this step, the lower MI is estimated. Therefore, the aim is to improve MI with VC methods.

2.3 Results

2.3.1 Single respiratory motion curve

Figure 2.4 shows the SD of the cycle time, the signal value of the end-of-inhale, and the location of the end-of-exhale for different sessions to compare the vocal-coaching effect for a single respiratory signal (abdominal movement). The volunteer group exhibited larger SDs in all parameters, but the effect of the VC session was more noticeable in the volunteers. The VC1 session decreased the SD in all volunteers, whereas in patients, VC did not result in a reduction in the SD of the breathing cycle time and location of end-of-inhale. In patients, the variation of all parameters for FB was relatively small (~1mm). The improvement of VC was limited by showing the end-of-exhale signal value in patients. This finding agreed with our expectation that the variation of 1D breathing signals reduced when subjects followed vocal coaching. The increasing variation in cycle time and end-of-exhale in patient groups may originate from the short recording time. Because patients' daily schedules are carefully controlled, subtle changes can become significant over a small number of breathing cycles.

2.3.2 Motion data visualisation

By utilising the KDE to visualise the 2D motion data, variation in respiratory motion between sessions could be observed. The patterns of KDE can be categorised into three common cases by our observation in this study, as shown in Fig. 2.5. [a] salient feature in all cases is a clear band with a hot spot (red arrow) at the lower left part of the KDE. The hot spot in Fig. 2.5 (left) corresponds to the general respiratory trajectory,

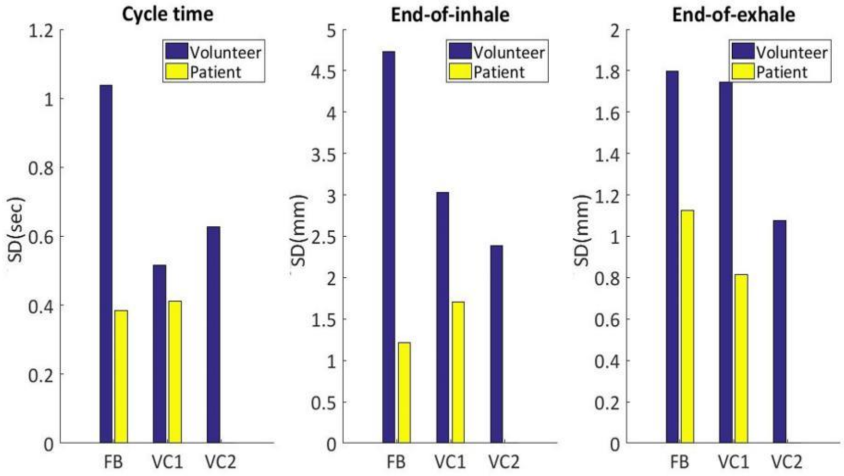

Figure 2.4: Box plots of the SD of the breathing cycle. Location of end-of-inhale and location of end-of-exhale for volunteer and patient data.

indicating that the end-of-exhale period was the longest in the entire breathing cycle and represented the most reproducible pathway. The end-of-inhale (green arrow) was also enhanced in some cases, whereas the enhancement was not as strongly noticeable as the end-of-exhale in those cases. The findings suggested that the end-of-inhale value was more variable and/or that less time was spent on the end-inhale than end-exhale. Fig. 2.5 [b] shows a closed-loop, demonstrating that motion followed a different path for exhalation and inhalation, in turn indicating a higher complexity of respiration. In Fig. 2.5 [c], two parallel bands were observed. This indicated that the breathing pattern changed within a single session. This may have arisen from the baseline shift of the thoracic movement. The MI result met our assumption that the regular KDE (Fig. 2.5 [a]) was the highest in the group. The KDE with a relationship change (Fig. 2.5 [c]) indicated lower MI.

2.3.3 Quantifying the MI of the two signals

Tables 2.1 and 2.2 quantify the mean MI for the entire abdominal and thoracic signals for every session. In both the volunteer and patient studies, MI was time-dependent and could only be computed for signals acquired simultaneously. The values of MI were high in most volunteers for the FB and R sessions, indicating that the relationship between two breathing signals is more stable in FB.

However, the result of the VC sessions showed a mixed influence on MI. For four out of five volunteers, MI decreased from R to VC1 (exception: volunteer 3). For VC2, an increase in MI was observed from VC1 for all volunteers. For two out of the five volunteers, the highest observed MI appeared in VC2. The changing relationship of the two breathing signals was unclear with a minimally increasing MI. For all patients, an increase in MI from FB to VC (with the exception of patient 2) was observed. For patients with low SD in cycle time, vocal coaching improved for maintaining consistency between thoracic and abdominal breathing signals (60% patients with higher MI with vocal coaching comparing with free breathing). An interesting finding in R showed that thoracic and abdominal movement became more similar to MI increased. That result may indicate either consistency in SI/AP internal motion or that total information from the surface reduces. The latter interpretation implies that there is less information available from surface signals to describe the complete motion model. To validate this assumption, the acquisition of internal images, such as those obtained by 4DCT, is necessary.

Volunteer	1	2	3	4	5
FB	1.12 ±0.04	1.05 ±0.3	0.65 ±0.29	1.16 ±0.13	0.72 ±0.1
R	1.23 ±0.08	1.39 ±0.11	0.94 ±0.15	1.56 ±0.12	1.61 ±0.06
VC 1	0.95 ±0.22	1.07 ±0.13	0.67 ±0.18	1.33 ±0.21	0.62 ±0.2
VC 2	1.00 ±0.15	1.24 ±0.11	1.62 ±0.06	1.63 ±0.03	0.85 ±0.03

Table 2.1: MI of respiratory motion using abdominal and thoracic motion data from five volunteers. 4

Patient	1	2	3	4	5	6
FB	0.67 ±0.1	1.4 ±0.70	0.85 ±0.11	0.94 ±0.14	0.7 ±0.19	0.62 ±0.15
VC	1.36 ±0.05	1.05 ±0.13	1.11 ±0.16	1.28 ±0.10	1.2 ±0.11	1.01 ±0.06

Table 2.2: MI of respiratory motion using abdominal and thoracic motion data from six female patients.

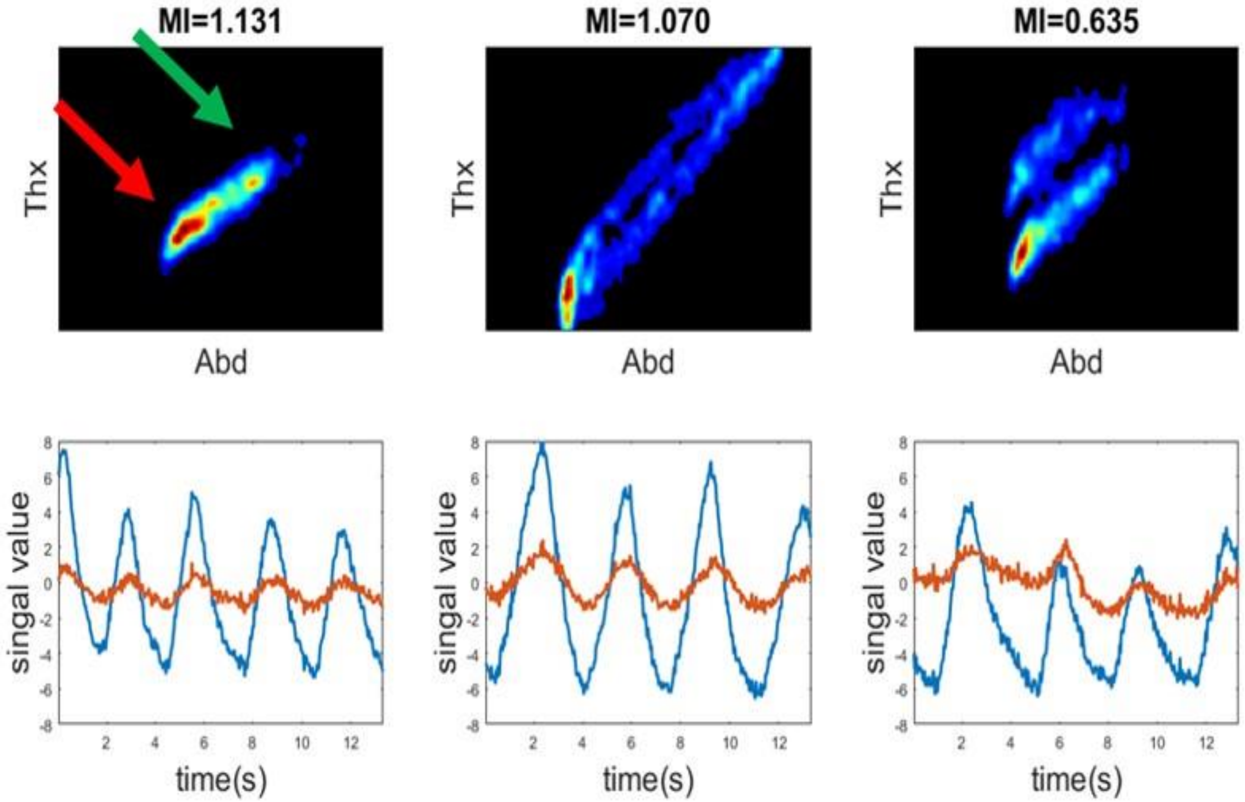

[a]

[a] [b] [c]

Figure 2.5: Typical KDEs from a single session. Abdominal (X-axis) vs thoracic (Y-axis) displacement is visualised. The colour map illustrates the likelihood of each position, with red as high and blue as low likelihoods. The figures below each KDE are the corresponded breathing signals (blue = abdomen, orange = thorax)

2.3.4 Correlation of motion between two sessions

The correlation of the breathing pattern between two sessions was evaluated as the similarity of the corresponding KDEs. The CC between the KDEs from FB and VC were calculated individually.

Table 2.3 lists the average CC for each session of all volunteers by comparing every day with every other day. There was a mixed result for vocal instruction. For most volunteers, the CC was similar or higher in R than in FB (with the exception of volunteer 3). For all volunteers, the CC with VC1 was lower than that with FB. An increase in CC was observed from VC1 to VC2 in all volunteers. For three out of the five volunteers, the CC was higher in VC2 than in FB. The result indicated that there is a mixed influence of the vocal coaching approach. There was no clear tendency to interpret the overall result, potentially due to the small sample size used in this study. There was a need for a large group to provide a more convincing result. Also, our assumption was challenged in R as not all subjects improved in the consistency of their breathing patterns, which hinted that their breathing was relatively unstable, more variation when compared with that of the free-breathing session. For volunteer 2,3 and 4, free-breathing session reached higher CC (CC=0.52) than R state (CC=0.4).

Volunteer	1	2	3	4	5
FB	0.38 ±0.03	0.71 ±0.02	0.45 ±0.11	0.41 ±0.08	0.71 ±0.07
R	0.51 ±0.1	0.67 ±0.06	0.14 ±0.1	0.4 ±0.04	0.81 ±0.02
VC 1	0.09 ±0.07	0.67 ±0.03	0.15 ±0.1	0.39 ±0.06	0.32 ±0.04
VC 2	0.21 ±0.13	0.85 ±0.02	0.52 ±0.08	0.74 ±0.05	0.47 ±0.03

Table 2.3: Average CCs by comparing every day with every other day.

2.4 Discussion and Conclusion

These initial results lend considerable weight to the use of surface surrogate monitoring in clinical applications. This study shows that multiple respiratory signals are able to be acquired with the Kinect system, which is easy to carry around and can be set up within five minutes. The sole problem is its latency in laptop recording, which may have been due to a limitation of RAM memory. Kinect is a promising, low-cost depth camera that could be useful in medical imaging applications, and its total price (less than 200 USD) meets our goal, which is to develop a relatively cheaper contactless image system to monitor respiratory surface movement.

Irregular respiratory motion is a challenge in thoracic tumour radiotherapy. Vocal instruction is a relatively simple method to regularise breathing patterns. Studies have analysed respiratory motion with 1D signals, mostly in abdominal motion, with Real-time Position Management (RPM) [62]. George [63] investigated biofeedback in detail by fitting cosine functions to the breathing waveform. The waveform presented in the research is symmetrical, but our study found that the inhale time and exhale time were unequal for most subjects, indicating that the symmetrical model may not be suitable.

Finally, Alnowami [64] applied the KDE to the classification of breathing patterns based on their phase. This study indicated that the breathing pattern could be either in-phase (Fig. 2.5 [a]) or out-of-phase (Fig. 2.5 [b]). However, the patterns between the sessions were not compared.

There is a need to quantify the outcomes, and to evaluate the effectiveness of personalised vocal instructions, all subjects' surface images were recorded during FB and VC, and abdominal movement was analysed. The difference between FB and VC patterns was noticeable. For the volunteers, VC greatly improved the variation in cycle time, end-of-inhale position and end-of-exhale position. This finding was in agreement with relevant studies [49, 65]. The end-of-exhale position appeared to be more stable when the instructions were generated on the same day (VC2).

The assessment of MI is an innovative approach to breathing signals. It was observed that the MI between two signals was inconsistent across breathing sessions. The changing value of MI indicated that the total information between the two breathing signals either increased or decreased in different sessions. For the volunteers, the MI from the R session was generally higher than that of the FB session. Furthermore, the MI from the VC2 session was usually greater than that from the VC1 session (VC1 = 0.93, VC2 = 1.27). The results from the patient group were in agreement with those from the volunteer group. The observed MI was higher with VC than FB, indicating that total information decreases when vocal instructions are followed.

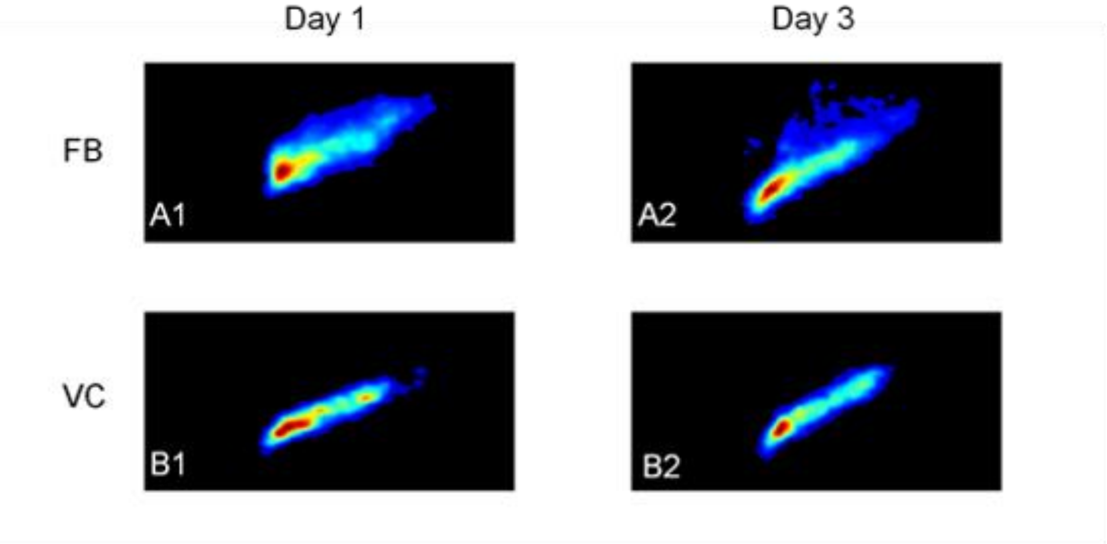

Figure 2.6: Examples of the similarity of KDE by CC. The respiratory motion in B1 and B2 (CC = 0.83) was more regular than that in A1 and A2 (CC = 0.53). This result corresponded with visual observations.

KDE offers an easy way to visualise surface motion. However, when using KDE, variations between single cycles and sessions are easily noticeable. The KDE method provides an alternative to compare the similarity between breathing patterns within different respiration days or sessions. Definite improvements in the regularity of the breathing pattern were visible, as seen in Fig. 2.6. The CC between different sessions indicated similarity of breathing patterns. We observed similar or higher CCs with R than with FB. This indicated that relaxed and uncontrolled breathing was stable. Furthermore, the CC in VC2 was greater than that in VC1 (VC1=0.32, VC2=0.56), implying that breathing is more stable when vocal instructions generated from the same day, VC2, were followed. This tendency was in agreement with the MI results.

Irregularities in the KDEs, such as those observed in Fig. 2.5 [b] and Fig. 2.5 [c], are likely to arise from the signals of thoracic motion. The thoracic signal is usually noisier, resulting in a lower CC because of a relatively divergent KDE.

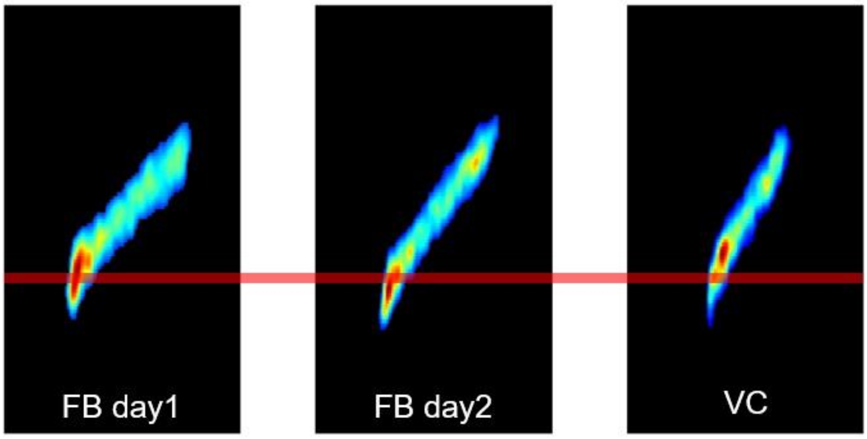

Figure 2.7: The VC affects KDE from a single patient

Furthermore, the amplitude of the thoracic regions is subtle. Occasional behaviours, such as deep breaths, coughs, and changes in the movement baseline, blur the KDE. Also shown in Fig. 2.7 is a single example of the influence of vocal instructions on KDE. The personalised instructions generated an expected respiratory rhythm, causing the breathing cycle to be shorter than instructed. The volunteers claimed that when they got used to the vocal instruction, they changed from one phase to another earlier than the instructions indicated. As a result, the VC KDE could be different from the FB KDE. The red line in Fig. 2.7 illustrates the site of maximum density. For VC, the centre of the high-density region shifted closer to the mean displacement.

There were a few limitations to this research. The most critical concern was the limited amount of patient data. More volunteers and patients are required, and their breathing signals should be recorded over multiple days to achieve conclusive results. In future research, images from 4DMR/Cine-CT should be considered the internal landmark to answer the central concept of the study.

This study revealed that VC is a promising approach to respiratory regulation, although, with the current performance, it is not suitable for clinical applications with a large variation in breathing regulation. More patients are necessary to obtain conclusive results. Moreover, a comparison between visual-feedback and VC methods must be performed for the verification of the influence of psychological expectations, wherein visual feedback; patients can observe their breathing paths by viewing the screen, a feat impossible in the VC method. The VC method provides time- and cost-efficiency, and an easily repeatable approach in both imaging and treatment rooms. The utilisation of **KDE** provides a simple way for observers in a clinic to monitor respiratory motion. In this study, we demonstrated the advantage of generating vocal instructions in a single day with a simple contactless monitoring method.

Chapter 3

Investigation of a 3D printing bolus for post-mastectomy patients

- **Publication**

  Chuang, C.S., Xu, R, Li, X., Fan, J., & Royle, G. Evaluation of a 3D printed Customised Bolus for post-mastectomy patients. *In preparation*.

In this chapter, the concept of personalised treatment in radiotherapy is extended into a parallel project for different thoracic tumours (i.e., breast cancer). This study investigated the application of 3D printing techniques in radiotherapy, mainly focusing on the use of a bolus during post-mastectomy radiotherapy.

Research aims and contribution

This research aims to investigate the feasibility of using new 3D material to make a bolus. The objectives of this research are as follows:

- To evaluate the new material dosimetry by percent depth dose (PDD) measurement and compare it with values found in the literature. The PDD measurement provides the necessary parameters for bolus design. This process validates the photon profile in the printing material and the interplay with other tissues using a treatment planning system.
- To create an optimised, user-friendly workflow from the source image to the final printed product. Specifically, clinicians should be able to delineate the target volume on the image, and the bolus should be able to be made without other programmatic skills.
- To verify the surface dose enhancement with the printed bolus, and perform a conformity test on patients to examine the feasibility of its clinical use. The

customised bolus is expected to increase the surface dose to fulfil the primary purpose. The air gap, which is not expected to exist with the printed bolus, is observed by the new CT scan.

I worked together with a radiation oncologist at Shenzhen People's Hospital to improve the current bolus for post-mastectomy patients. I spent a full year at the department of radiation oncology in Shenzhen People's hospital to help develop an economical and time-saving method of the same quality. I was involved in workflow development and primary project management, and I also tested the new printed material for dosimetric feasibility and clinical placement outcome.

The novelty of the work

This work involves the development of an overnight producing workflow for personalised bolus. After thorough literature research on patient-specific 3D printing, we noticed the lack of integrated research investigating the feasibility of 3D techniques in the literature. Furthermore, a comparison between various printed materials was impossible since every publication used different materials from the companies they are in collaboration with to test their products. During a discussion with a leading oncologist and physicist, we decided to optimize the current workflow for each article [65~69], discussed in a later section, to perform the production overnight. The printed bolus can be completed the day after CT simulation, and it involves a similar waiting time for patient treatment as the conventional procedure. The customised bolus allows better dose coverage and normal tissue protection.

3.1 Rationale

This work aims to develop an advanced method to improve dose distribution as radiotherapy in superficial regions is a critical issue. Due to the characteristics of a high-energy photon beam, receiving a sufficient treatment dose in a shallow region is difficult to achieve. This situation becomes more challenging when patients with breast cancer undergo breast removal (mastectomy), as such patients can expect to retain little tissue on their chest after surgery. In order to improve treatment quality, the novel procedure of breast radiotherapy can be introduced. Among all available technical solutions, the most common alternative is to place the bolus on the patient's surface. This method entails the addition of an extra layer on the skin and an increase in surface dose. However, air gaps may exist between the bolus and the skin due to scars from previous surgery. Related researches conclude that the uncertainty regarding planned and actual dose can show a difference of up to 10% [65, 66]. Therefore, the primary aim is to create a perfectly adhered bolus in order to optimise the dose distribution under the skin. In this regard, 3D printing methods are potential solutions that can overcome the problem of air gaps. Owing to the rapid development of 3D printing techniques, the production of highly precise and customised bolus has become economically and clinically feasible.

Major concerns with the 3D printing technique include the lack of knowledge of new material and the actual interaction between a printing bolus and human skin. Currently, there is no gold standard for 3D printing in clinical applications. Additionally, a few articles have addressed the alignment of the bolus. Therefore, there is no guarantee that the air gap problem can be fully solved.

This study introduces a rapidly developed workflow to build a bolus in the clinical environment. To expedite the production process and lessen the required time, a user-friendly overnight workflow is established. Briefly, a simple dose measurement with films is performed to visualise the dose profile and evaluate the dosimetric result. The film readout is capable of evaluating the water-equivalence of the printing material. Furthermore, the covered bolus on a patient's skin is followed up by CT to evaluate the fit between the printed bolus and the patient's contour. More specifically, this study pertains to the important process of quantifying the air gap volume and assessing the feasibility of such a highly customised product.

3.1.1 The air gap problem

Butson [67] investigated the effect of an air gap volume by having a parallel plate ionisation chamber held in a solid water phantom. This was initially used without the introduction of any air gaps and irradiated with a 6 MV photon beam to produce a reference reading for the bolus and undamaged tissue. A set of measurements was conducted by changing the length of the air gap, field size, and beam angle to determine the effect. There was no reduction in skin dose with a 10 mm bolus and an air gap of 2 mm. With an air gap of 4 mm, the dose reduction varied from 0 to 4% depending on the field size. A small field size showed a great reduction with an air gap. The worst condition, a 10 mm air gap with a small field size (8 x 8 cm) and a beam tilt angle of 60, reduced the surface dose by up to 10%.

In addition, Khan [65] conducted a similar study but used Gafchromic EBT films instead. The EBT films were sandwiched into a solid water slab, with a bolus covering the slab. The air gap was from 0 to 5 cm with two field sizes: 5 x 5 cm and 10 x 10 cm. The surface dose from the 6 MV beam decreased significantly for the air gaps when the distance between the bolus and skin was greater than 5 mm. However, this study did not compare the influence of different beam angles. From both studies, it was concluded that a tilted beam angle, small field size, and air gaps larger than 2 to 5 mm should be avoided. However, with a tangential view, the beam to the bolus was not vertical. Therefore, dose reduction became more influenced by the air gap. To minimise the unwanted dose by using a bolus, an air gap between the bolus and skin of less than 2 mm was used as a conservative criterion.

Because of the air gap, discrepancies in daily bolus placement led to a surface dose reduction or even unwanted dose distribution around an organ at risk. For post-mastectomy irradiation, the ipsilateral lung may be covered by a hot spot with an air gap of uncertain size. To deal with the air gap problem, a customised bolus, fabricated from skin contours to reduce these discrepancies, offers a possible solution.

3.1.2 3D printing technique in radiotherapy

The goal of an ideal radiotherapy treatment plan is to address dose distribution with sufficiency and uniformity in the target volume. According to a guideline from the ICRU 62 report, the Planning Target Volume (PTV) should be covered by 95% of the prescribed dose. However, a challenge emerges when treating a shallow tumour. There is a built-up region with high energy photons between the surface and region of maximum dose. This phenomenon, also known as the skin-sparing effect, causes an insufficient dose below the skin. This effect results in potentially insufficient coverage of PTV for a shallow tumour [67], where 6 MV photon beam cannot reach maximin dose before PTV, where less than 1.5 cm form the surface To overcome the skin-sparing effect problem, an alternative method is used to improve the dose distribution for the treatment of superficial tumours.

The application of a bolus, which is a flexible tissue-equivalent layer covering the surface of lesions, improves the problem of under-dosing at the skin surface for superficial lesions. With this additional layer on the patient's skin, the built-up region of high energy beams moves forward across the surface of the skin and improves the dose coverage for superficial lesions. The application of a bolus to superficial tumours has been shown to have clinical efficacy for post-mastectomy [68], head and neck [69, 70], and external limb [71] irradiation. A bolus can theoretically solve various underdose problems in superficial radiotherapy.

In radiotherapy, 3D printing has been highlighted as a supporting technology because of the feasibility of prototype devices. This concept has been extended to various phantom studies for both image and dosimetry experiments. Furthermore, 3D printing makes fabricating a sophisticated volumetric object from any virtual design possible. The products are printed directly from the computer software without third-party processing, so from design to production, the product can be finished in a single room overnight. Users can change their design easily without negotiating with the manufacturers, as was done with customised products before. This novel technique is straightforward for users, but time-consuming.

Leading researches that relate to respiratory motion can be used as examples. Mayer's team constructed a thoracic phantom with two different materials to simulate bone and muscle tissue [72]. This innovative phantom allowed them to measure the dose from a moving tumour inside the simulated thoracic cavity. Dosimetric measurement is an effective approximation of a real human for demonstrating the influence of respiration on dose distribution. It was impractical and expensive to build a phantom for a single function before the maturation of the 3D printing industry. However, as the cost of 3D printing continues to decrease, the availability of cheap, self-manufactured customised products will enhance the ability of researchers to progress from creative impulse to effective research. Our study explores this concept.

Preliminary 3D bolus research illustrated the relative potential outcome by increasing the dose for a superficial tumour. Using a minimal air gap, Burleson [65] investigated the application of a customised printed bolus to improve the uniformity of dose distribution in the nasal cavity. The nasal cavity is one of the most challenging regions for radiotherapy, owing to its irregular surface and superficial region in which dose delivery is considered problematic. A block with the inverse shape of a RANDO phantom was printed so that the nasal region was covered with the targeted thickness. However, our study used other materials and targeted the breast rather than the nasal cavity.

Park [69] described the application of a printed bolus in post-mastectomy radiotherapy. The work was performed in South Korea, where the target patients were more similar to those in our study: Asian women. Covered by the customised bolus on the target volume with electron beam therapy, 3D-printed boluses resulted in a reduction in the mean dose to the ipsilateral lung by up to 20%. Furthermore, another advantage of shaping the dose distribution is that by amending the bolus design with an electron beam, the organ at risk can be avoided becoming a hotspot. The surface of the outer bolus is in front of the lung. These were all promising outcomes for 3D printing; because the bolus mirrored the contour of the inner lung, the hotspot of the electron beam decreased sharply.

The aforementioned studies represent a small sub-section of bolus research, which largely focuses on dosimetric experiments or clinical applications. Burleson and Kim [74] focused on treatment plan comparisons of phantoms for the nasal cavity with 9 MeV and 6 MV electron and photon beams, respectively. Their studies lacked detailed patient information in the construction of the boluses. Since the patients vary in their bodily structure, customised boluses may not be as perfect a match as expected. Park demonstrated a satisfactory result for a virtual patient treatment plan. Their dosimetry test did not evaluate the material, which can be uncertain when dose curves or exact material density is unknown. No integrated research studies have been conducted on dosimetry and feasibility for clinical use.

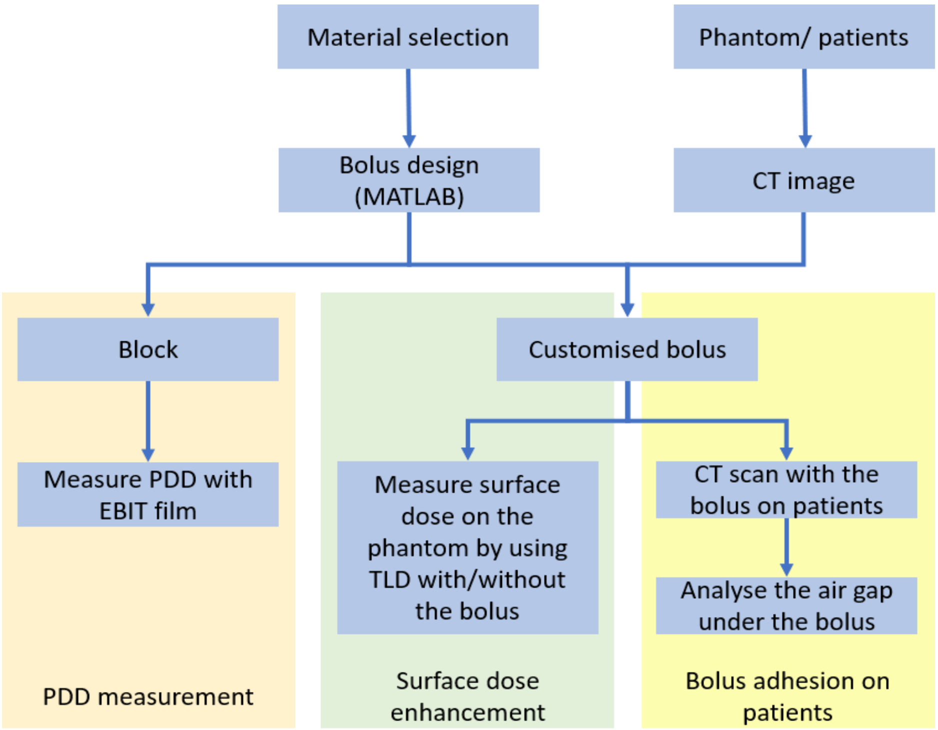

Figure 3.1: Workflow of the experiments presented in this chapter.

3.2 Materials and Methods

3.2.1 Printing material selection

New material was introduced to Shenzhen People's Hospital, but due to the bureaucratic regulation of research funding in Shenzhen, purchasing foreign products (that is, all 3D printers used in the aforementioned studies) is restricted. To use the same printers as used in other studies would have been time-consuming due to the obligation of clearing Chinese customs. Moreover, this part of the funding was used as a proof-of-concept part in the project, and thus a desktop rather than an industrial version of the printer was used. There is a limited printed volume for the desktop version with a single material, whereas the industrial printer is capable of printing dual materials at full thoracic size [73].

Therefore, the printer used was developed by a local research team from the Material Science Department of Tsinghua University. The price of the printing package, including a desktop printer, a bottle of resin, and software was only a quarter of the price of the 3D printers used in the aforementioned studies.

Furthermore, the distributor claimed that the density of the printer resin could be adjusted to meet our requirements by mixing the two materials provided in certain concentrations. This would allow the production of customised bolus material that could be matched to the requirements of the experiments. While the material seemed to be adaptable to meet any of the requirements for this project, the actual performance required characterisation. Therefore, only a single material was used for the initial stage of this project.

3.2.2 Printing technique selection

Two primary formatting techniques are used in mainstream 3D printers:

(1) Fused deposition modelling (FDM) and (2) stereolithography (SLA). The FDM progress is based on the heating and layering of thermoplastics where a temperature-controlled extrusion head is fed with a thermoplastic material, which is then heated to a semiliquid. Burleson [59] presented a detailed workflow and system setup for the FDM printing technique for printing boluses. Simply stated, FDM is like the process of adding cream onto a cake via a pastry bag. The source of the material, normally similar to a bundle of string, is melted, passed through the nozzle, and a selected volume of material is stacked on the target location. There is no need for further operation after the printing process for FDM products.

In contrast, SLA is the process through which light (laser or UV) causes chains of molecules to bind, thereby forming polymers. The ingredient, resin, is composed of relatively short carbon chains which join together to create much longer (and therefore stiffer) chains when exposed to UV or laser light. When a sufficient number of chains have reacted, the final product is a solid part which comprises of a long carbon chain. The length of the polymers, which determines the hardness of the final product depends on the exposure time. The longer the resin is exposed, the harder the layer that forms. The process repeats until those polymers then establish a layer of the completed product. After the process, the area of printed products is soaked in the resin tank. The resident resin on the surface solidifies after exposure to UV from daylight and forms an undesirable shape. To clean the surface, the printed product must be washed using water (in the case of water-soluble resin) or soaked in an ethanol bucket (in the case of oil-soluble resin).

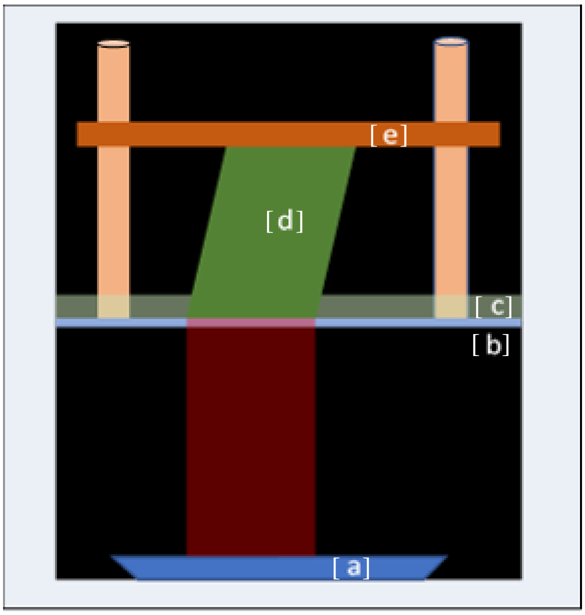

Figure 3.2: Schematic demonstration of an SLA printer. [a] A light source, a laser, or UV. [b] The transparent bottom of the tank. [c] The printing material: photosolidified resin. [d] The printed product. [e] The moving platform to carry the printed product.

Printing Technology	Stereolithography (SLA)
Build Volume	192 120 200mm (7.5” 4.7” 7.8”)
XY Resolution	75 μm
Layer Thickness (Z resolution)	10, 25, 50, 100, 150, 200, 300 μm
Printing Speed	1,000 cc/hr, 200 mm/hr thin-walls

Table 3.1: Characteristics of the 3D printing performed in this work

There is no clear evidence pertaining to which printing technique is more effective for bolus manufacturing. The collaborating company only manufactures SLA-based 3D printers, and hence, we investigated an SLA printer. Compared with other commercial printers, this new project offers a desktop printer that is more convenient for the initial project of prototype evaluation. The target product we investigated was fabricated using a new UV-based printer (SLA technique; SLASH#, UNIZ TECHNOLOGY LLC., USA) with green oil-soluble resin.

3.2.3 Bolus design: Block

In this initial study, to determine the properties of the untested 3D printer, an elementary geometric shape was used, which was a block. The blocks were also used for dosimetry measurements in the following session. The entire printing progress was made using the SLASH#.

Our target was to build two 15 x 15 x 3 cm blocks. The block was designed with 3D Builder, a programme that comes baked in with Microsoft Windows 10. The programme allows users to draw simple shapes, such as a cylinder or cone.

1. First, we opened 3D Builder and selected a cube.
2. The initial size of the cube was 4 x 4 x 4 cm. The size was amended to our target by clicking the arrow in each direction. The amended cube is shown below in Fig. 3.4.
3. The file had to be saved as a printable-file (in the STL file format) that could be read by 3D printer applications.
4. After the STL file was loaded into the printer console, the block was rotated 90 degrees because the block and the moving platform are vertical. This is the limitation of the printer's printable size (the Y-axis is only 12 cm long). The precision of the Z-axis was 0.05 mm, with 2 seconds of exposure time for solidification at each layer.
5. The final project object was attached to the tray and covered with the remaining resin. It had to be removed carefully with a flat shovel and placed into a bucket of ethanol to clean the resin residue on the surface.

As soon as the resin came into contact with water, it turned into a white glue-like form and was difficult to clean. This is unlike other commercial printers with water-soluble resin, which are much easier to clean than ours. Our experience led us to soak the product with medicinal alcohol, which was the cheapest available solution. Next, we used tissue paper to remove the remaining resin on the surface. Another problem we noticed was that the blocks were too heavy for our target volume. The block fell into the resin pool halfway through printing due to its weight, as shown in Fig. 3.3 [b]. Therefore, the final printed products were six 15 x 15 x 1 cm blocks, as shown in Fig. 3.3 [c].

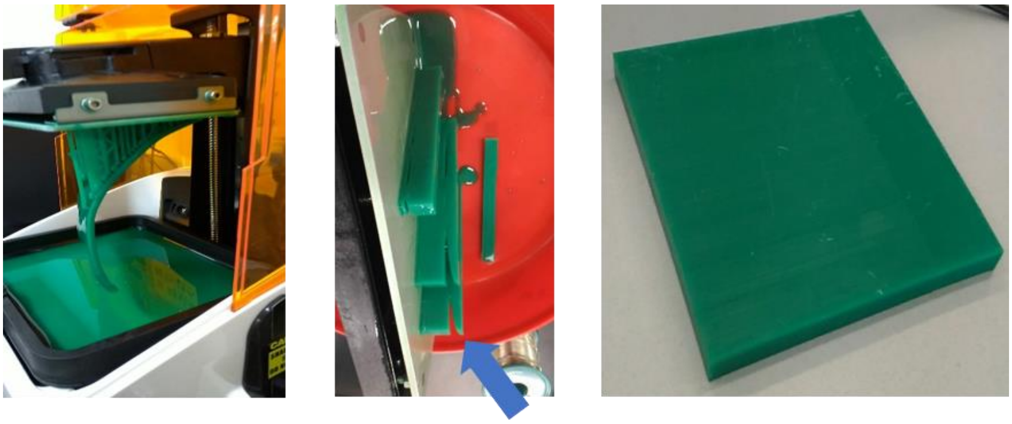

[a] [b] [c]

Figure 3.3: The print process of the customised bolus. [a] The printer uses an upside-down printing process. The green resin (lower tray) solidified when exposed to UV. The printed product was associated with a supporting column to carry the weight of the bolus; if this measure had not been taken, the bolus would have fallen into the tray. This condition became a limitation as we used the printer. The orange shell is to prevent UV leaking from the bottom when applicants observe the printer operating. [b] The failure of the printer was due to the weight of the block. A fissure (blue arrow) was observed. [c] The successfully printed block for the tests (15 x 15 x 1 cm).

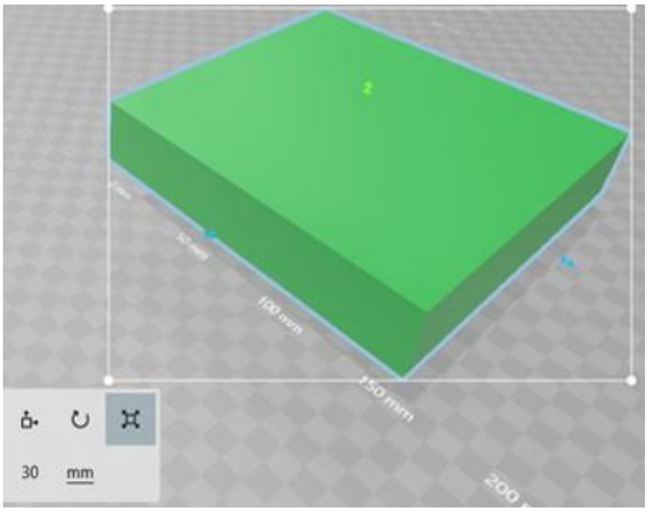

Figure 3.4: Design of the block with a target size of 15 x 15 x 3 cm

3.2.4 Bolus design: From image to printable file

The next step was to build a more complicated model. The bolus was designed according to the contour of the patient or phantom surface. The source of the image to be designed was acquired from the CT simulator at Shenzhen People's Hospital. The CT images of both the anthropomorphic phantom (West China Centre of Medical Sciences of Sichuan University), female torso phantom (China, Fig. 3.5), and three female patients who underwent mastectomy were required for the bolus design.

1. Image acquisition

The treatment room and simulator room were located in a contracted hospital (distal court), whereas the department and CT simulator were in the main court. These two places are separated by 45 minutes by car. The regular procedure in this hospital for radiotherapy patients is as follows:

(i) Patients present for immobilisation using a vacuum bag or mask in the conventional simulator room, and the radiographer draws the marker on their skin (distal court).

(ii) Patients return to the main court for the CT simulation with their markers on the same day (main court).

(iii) Physicians and medical physicists finish the treatment plan in the radiation oncology department. Then, the treatment plan moves to the database in the treatment room (main court).

(iv) Patients visit the treatment room for their sessions (distal court).

The simulated CT images for the treatment plan of three female post-mastectomy patients were used for the bolus design. The axial size between each slice was 5 mm. For the phantom study, the phantom was positioned with the vacuum bag by a physician in the conventional simulator room. The three cross-lead markers placed on the phantom surface with laser lines were used as the marker for the CT simulation. What differed was that the patient CT images had a 5-mm gap, whereas the gap was 1 mm between each axial image for the phantom study.

The image data in the digital imaging and communications in medicine (DICOM) file format was acquired during the CT simulation for each subject. The acquired DICOM files were used to create virtual 3D-printable boluses.

2. File conversion

The CT images were processed using a MATLAB function, from data conversion to bolus design. First, CT data converted the DICOM file into an Mfile (MATLAB-readable file format) with the MATLAB built-in function dicomread. In a complete file with an all-DICOM structure, we only focused on two types of information: volumes and voxDim1 (also voxDim2 and voxDim3). Volume represents the 3D matrix of the whole CT image, and voxDim is the pixel size in each direction. Using the phantom image as an example, the voxDims were 0.973, 0.973, and 1 mm.

3. Building of the surface model

Contouring the surface is a critical process in bolus design. The surface of each subject is the distance from the edge of the image (Y-axis) to the first pixel to reach the selected Hounsfield unit (HU). The target HU was -100 from the edge of the soft tissue. The patients' surface can be described as the inverse image of this distance map, as shown in Fig. 3.6 [c].

(i) The contour was estimated slice by slice. Fig. 3.6 [c] demonstrates the axial signal image of the phantom.

(ii) The binary segmentation was processed by the threshold as -100. The value separates the air, including lung tissue and other tissue.

(iii) The location of the first non-zero pixel was calculated on each Y-axis as the contour of the slice. Therefore, 1D data could be obtained for each slice image.

(iv) After processing all the slices, the contouring data could be assembled into a 2D depth image of the subject. However, this was an inverse depth image; the peak of the surface showed the lowest value. After the image was inverted, the final depth image for surface contouring was complete, as shown in Fig. 3.6 [c].

Figure 3.5: Phantom immobilised with a vacuum bag.

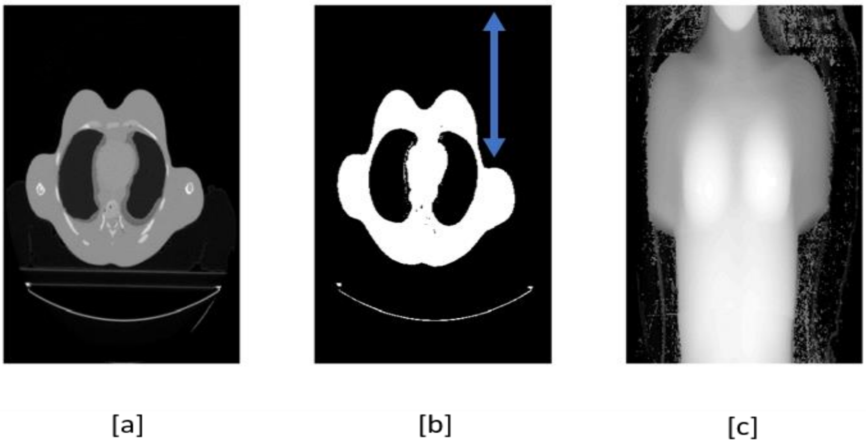

Figure 3.6: Workflow for the bolus design. [a] This is the CT image of the phantom acquired from CT sim. The image had a threshold of -100 HU (soft tissue density). The blue arrow illustrates the distance from the edge of the image to the first nonzero pixel as the subject's surface. This process was conducted for all the axial slices in the CT series. [c] The final depth image from the phantom. The intensity shows the distance from the couch level. The breast regions are the most elevated part in the Z-axis and therefore show the highest intensity.

(v) Because the ROI was manually selected, the noise in the background was negligible.

4. Bolus design

The physicians manually selected the region based on the target volume to define the area of the bolus (ROImask). While the value of the distance was pixel location-based, the surface image could represent an integral number. Furthermore, regarding the pixel size of the CT images, the distance value could change considerably between two adjacent pixels.

The surface directly converted from the depth image was uneven, as shown in Fig 3.7. The smoothness of the surface from the 3D object was required because the original file contained triangular meshes as surface information.

This was an underlying proof-of-concept study. Rather than processing the model with a 3D graph, open-source programmes were used. The programmes were sourced from the MATLAB database (surf2solid and smoothpatch).

The surf2solid programme creates closed solids by adding a flat base or offsetting the voxel size from the DICOM information after receiving thickness information. The bolus was used to determine the target thickness (5 mm). This function determined the actual bolus size by providing the pixel size.

The smoothpatch programme smoothed the triangulated patch/mesh. The effect of this function is demonstrated in Fig 3.8 [a]/[b]. The function supports accurate curvature flow smoothing, keeping the edge ratio the same. The distance to the surface can be a continuous value.

5. Printable file

As with the block phantom, the model was required to convert the file into a printable format. However, MATLAB does not provide this function directly. Another open-source programme was used to convert the Mfile to the STL format.

After finishing the file of the prototype 3D bolus, the bolus was transformed into a printable size due to the limitation of the printing tray (X-Y size). The position of the bolus is shown in Fig. 3.3 [a]. The precision of the Z-axis was 0.05 mm, with 2 seconds of exposure time for solidification at each layer. This description means every exposure formed a 0.05 mm-thick layer of the solid layer.

The design and weight of the bolus influenced the exposure time. A shorter exposure time of the resin softened the final materials, leading to the unsupported structure shown in Fig. 3.2 [b]. Hence, considering the volume and weight of the customised bolus, and as suggested by the agent-based in prior experience, an extended exposure time was required, which inevitably resulted in a higher density and the final product to be quite heavy. Furthermore, the supporting columns were added at the suggestion of the agent. The overall process took approximately eight hours for each bolus.

For medical requirements, an overnight printing protocol can be opted for, which allows the bolus to be ready on the following day after CT scanning. The four open-source functions used in this work were as follows:

- **dicomread**: Reads DICOM images in MATLAB. It is a built-in function.
- **surf2solid**: Turns thin surfaces into closed solids by adding a flat base or offsetting with a given thickness. https://uk.mathworks.com/matlabcentral/fileexchange/26710-smoothtriangulated-mesh
- **smoothpatch**: Ensures that the accurate curvature flow is smoothed. It smooths in the regular axis, keeping the edge ratio the same. It also supports Laplacian smoothing with inverse vertice-distance-based umbrella weights, making the edge lengths more uniform.

  https://uk.mathworks.com/matlabcentral/fileexchange/42876-surf2solidmake-a-solid-volume-from-a-surface-for-3d-printing
- **stlwrite**: Coverts the Mfile into the printable STL format.

  https://uk.mathworks.com/matlabcentral/fileexchange/36770-stlwritewrite-binary-or-ascii-stl-file

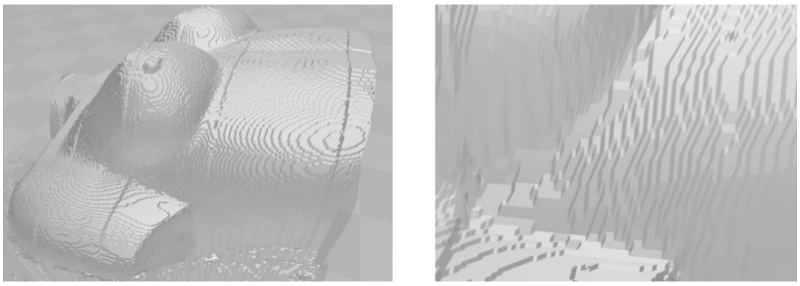

Figure 3.7: Raw STL file directly converted with Surf2solid from the 2D image in Fig. 3.6 [c]. Due to the discrete value of distance measurement, the surface was relativity rigid and not suitable for printing. The zoomed-in image reveals the step-like features.

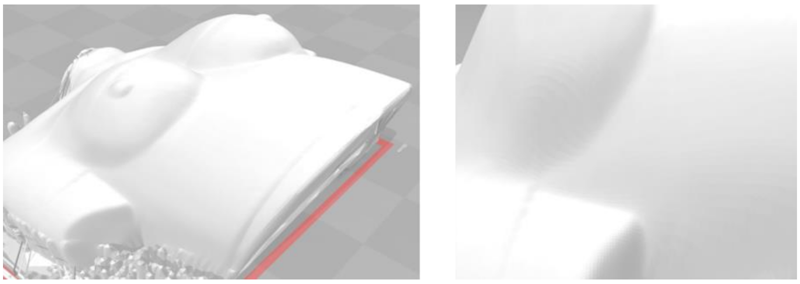

[a] [b]

Figure 3.8: The STL file after the smoothing process with smoothpatch. The surface of the phantom becomes a continuous change, which is smoother than that of the raw data. The zoomed-in image of the armpit area reveals that the step-like features have been removed.

3.2.5 Comparison of PDD measurement

The assessment of tissue-equivalence has become a required process for a bolus. Bolus material should approximate tissue-equivalence, presenting similar properties to water. In this experiment, we applied the target material (M_{target}) and another commercial printer material with different formation techniques, using an FDM printer from a local provider. The material for the FDM technique (M_{FDM}) was polylactide (PLA), which was the same material used in Burleson’s study [59]. The six blocks made of the M_{target} were the 15 x 15 x 1 cm blocks from section 3.2.2, and the blocks made of the M_{FDM} were 15 x 15 x 3 cm.

Compared with measuring from the Roos chamber, a plate ion chamber which is

usually used a dose measurement, film measurement is more

Figure 3.9: Prescan of the film and the strip for PDD measurement.

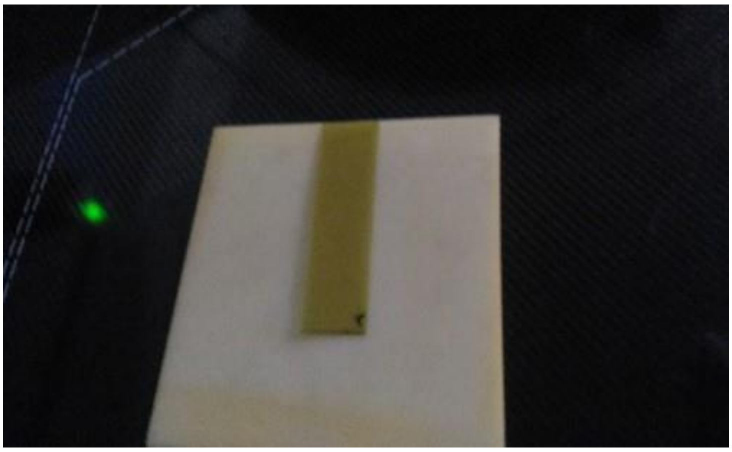

Figure 3.10: Position of the film and blocks. The strip was placed in the middle of the blocks and then sandwiched.

usually used a dose measurement, film measurement is more time-efficient in a busy treatment room. The Gafchromic EBT3-0810 film (lot # 05171701; International Specialty Products, Wayne, NJ) was sandwiched between two blocks (3 cm thickness for each side). Each film was required to be pre-scanned a day before the experiments and was separated into strips of 12 x 3 cm for measurement, as shown in Fig. 3.9. After the total measurement, all strips were placed in the same location on the scanner to be read. The films were scanned using a flatbed scanner (V800-Epson, Seiko Epson Corp, Nagano, Japan) before exposure and after being irradiated for 24 hours for precious optical density (OD).

The experiment revealed the fundamental radiological property of the printed material. Knowledge of the PDD provides an understanding of the built-up region. Hence, the minimal thickness of the bolus can be estimated. Chamber measurements are conducted for more detailed analysis in later processing steps.

The setup was also surrounded by solid water for scattering irradiation. The stack was placed in line with the beam axis with a source-to-surface distance (SSD) of 100 cm, but it had a subtly tilted angle to prevent self-build-up. A photon beam of 6 MV and electron beams of 9 MeV, the standard treatment beam energy for this local hospital, were used for the measurements with 100 monitor unit (MU).

The dose-OD curve was not linear, and calibration was required to be performed for each box. To set up the corresponding curve, ten extra exposures were taken with individual MUs. The measured MUs were 0, 10, 30, 50, 70, 100, 200, 300, 500, 800, and 1000. The film was placed under 5 cm of solid water with an SSD of 100 cm, as standard treatment distance.

3.2.6 Skin dose evaluation with the phantom

To evaluate the feasibility of skin dose enhancement, the surface dose was measured with and without the printed bolus. As with the original plan, the EBT film was inserted into the gap of the phantom layers. The film was cut to fit the contour of the phantom surface.

The readout of the film provided the internal dose distribution, and it illustrated well the difference in the hotspot intensity at the edge of the lung and heart. The left breast was selected as the target region. However, the female phantom was immobilised with a vacuum bag for the entire experiment as in the procedure mentioned in session 3.2.3, and the physicians were worried about altering the position of the film when unpacking the vacuum bag to remove the film. Furthermore, positioning the films inside the phantom was impractical, and therefore, for the phantom study, only the surface dose was measured.

In contrast to the patient CT images, the axial gap for each slice in the phantom image was 1 mm to provide more precision for the bolus design. This series of CT images was only used for the bolus design rather than treatment planning due to the problem of position uncertainty. The bolus manufacturing process was described in section 3.2.3. An additional CT image was processed after the printed bolus was finished, and two CT scans were taken with and without the bolus covering the phantom. The physicist created a routine treatment plan: 2 Gy covered in 95% isodoses of PTV for each fraction, with two tangential views with a 6 MV photon beam.

Tissue	Phantom	Actual [68]
Lung	-783	-700 to 600
Soft tissue	-11	100 to 300
Bone	151	700

Table 3.2: The HU for each tissue of this phantom. The actual human tissue HU is provided by [68] as comparison

Figure 3.11: The setup of a female-phantom study and the location of TLD on the left breast of the phantom. S, I, R, L, and C refer to the superior side, inferior side, right side, left side, and centre point.

The method was inspired by Ha [76]. In their study, optically stimulated luminescence dosimetry (OSLD) was arranged on the phantom surface with a conventional bolus and a printed bolus. In contrast to their setup, we used nine thermoluminescent dosimeters (TLDs) offered and counted the readout by the Shenzhen Prevention and Treatment Center for Occupational Disease in China. This hospital is the authority for health physics in Shenzhen, offering a personal dosimeter to radiation-related workers. Unfortunately, they can only provide the readout of the TLDs and no other useful information such as the dose-response curve. It may be that the TLD is not suitable to use with a high energy beam. These TLDs were attached to the surface of the left breast, as shown in Fig. 3.11, to measure the variance of the skin dose. The TLDs were aligned with the laser lines in the treatment room. Each TLD was positioned approximately 2 cm away from the nearest one. The phantom was irradiated in a single session (2 Gy) with two views to simulate the patient’s condition, and only the photon beam was used during this session.

3.2.7 Evaluation of the air gap under the bolus

The final part of this research involved the printed bolus being placed on the three selected patients for conformity. One item to be aware of for this study was that the patient’s body contours changed during the treatment cycle. The printed material was solid, but air gaps emerged because of this change in body contours. The entire treatment session normally takes six weeks, and it is highly possible for figure change in patients by following nutrition instructions or any other prescription. To illustrate the applicability of the printed 3D bolus, the air gap between the bolus and the patient’s surface was calculated using CT image sets.

The source of the CT images used to design the bolus was the same as for the treatment planning images. The bolus design process is shown in section 3.2.3, and the bolus was made in the middle of the treatment session three to four weeks after the simulator CT scan, at which point we considered such a period sufficient to verify our hypothesis. A repeat CT scan was applied to evaluate the agreement between the design of the printed bolus and the patient’s contour. Patients were asked to bring their own vacuum bag from the distal court to the main court for the repeat CT scan to ensure that the position was correct. The bolus was placed on the patient’s surface without markers.

Figure 3.12: Demonstration of a conformity test on a patient. The printing bolus was aligned on the patient's skin by her physician. The entire setup was repeated on the day of the CT sim.

Adhesion with skin, i.e. conformity of the printing bolus, was evaluated as the voxel Hounsfield Unit (HU), which defined less than -100 HU as the air. Due to the partial volume effect, the voxels from edge of bolus are with higher HU. Hence, the threshold of air is used -100 HU to capture the contour. Only the air volume under the printed bolus that influences the dose distribution was considered as air gap. The maximum distance and the total volume were the criteria for evaluating the conformity of the customised bolus. The air gap was measured column-by-column in the image segment, and the difference was calculated in each column. The nonzero value existed at the boundary from air to solid part (1) and vice versa (-1). The assumption was that the column with the air gap included air (1), bolus (0), air gap (1), and skin (0). Hence, the distance of the bolus was from the location of the first 1 to the location of the second. The final air gap was then visually checked for unwanted noise.

3.3 Result

3.3.1 PDD measurement

The CT images of the two materials were acquired for HUs, which can be related to electron density. They were 165 and -36 HU for M_{Target} and M_{FDM}, respectively. Although that M_{FDM} had an HU closer to water, neither of them were perfect water-equivalent materials. The PDD curves for both materials also agreed with the CT results.

The two images, un-irradiated film and irradiated film, were placed on the same location on the scanner. The region of interest (ROI) was selected on the irradiated film, while the corresponding location of the un-irradiated film was determined. The OD value was calculated pixel-by-pixel in the ROI. The result shows a satisfactory fit between the OD value and MU. The PDD results were used for the fitting curve to estimate the actual dose.

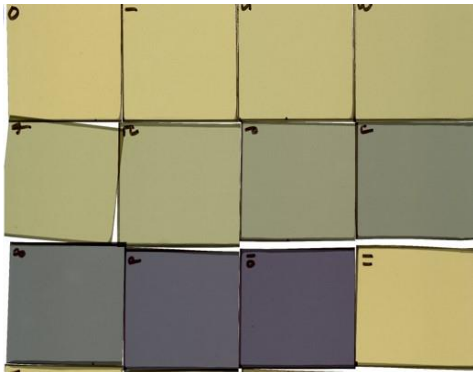

Figure 3.13: The irradiated film with different MUs for calibration. The squares are marked from 0 to 10 and correspond with the MU mentioned in section 3.2.2. The square marked as 11 is the background.

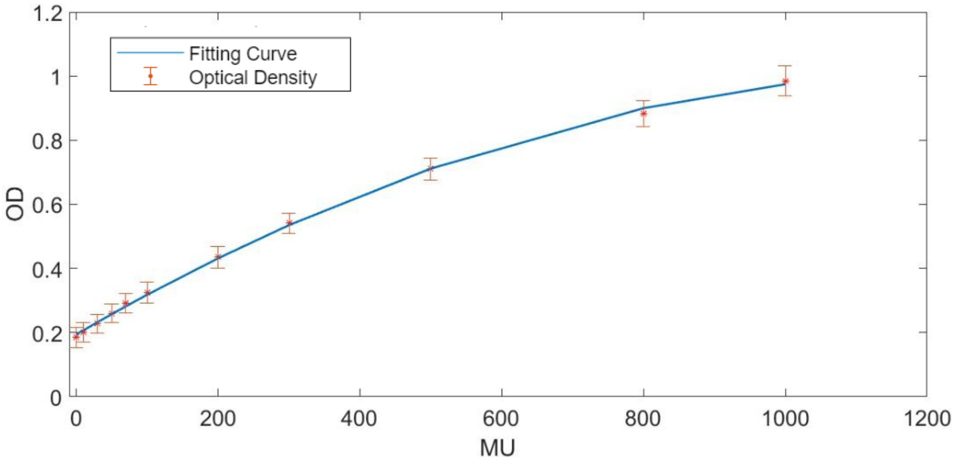

Figure 3.14: The calibration of the OD and MU curve. The dose-grayscale response is nonlinear. An additional experiment is necessary to build the correct response curve. PDD is the relative dose. Therefore, we used MU rather than the exact dose. The MU values were 0, 10, 30, 50, 70, 100, 200, 300, 500, 800, and 1000. The fitting curve (R-square= 0.99) is shown in the same plot. The fitting curve adjusts the measurement from the PDD with OD.

Figure 3.15: Demonstration of the irradiated strip with a 9 MeV electron beam. The beam enters from the side with a number, which is located in the darker part of the strip.

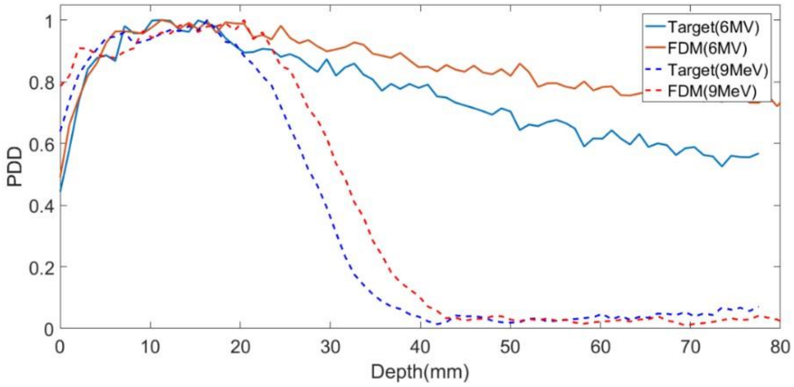

Figure 3.16: PDD curve of EBT film with two printing materials. In this case, two common treatment energy for surface treatment of PDD were performed with 6 MV photons and 9 MeV electron beams.

There was a 3.6-mm shift at the dmax, location with the maximin dose, under the 6 MV photon beam, which was 13.5 mm for M_{Target} and 17.1 mm for M_{FDM} . This shift was different in the built-up zone for both materials. There was a shift of 15 mm for the built-up zone in water under the 6 MV photon beam. These results also showed the minimal thickness of the bolus for each printing material. As expected, with a greater HU (HU>0), there was a steeper build-up and drop-off before and after d_{max}. However, there was little difference in the build-up curve for both materials.

The outcome was similar to the 9 MeV electron beam; d_{max} values were 17.4 mm and 21.4 mm for M_{Target} and M_{FDM}, respectively. The target material demonstrated the potential of the bolus material with a slightly shorter built-up region than the one we found for water, which was 1.5 mm higher. This result implied that manufacturing the customised bolus requires a lower volume of resin than PLA to reach the same quality.

3.3.2 Skin dose with the phantom

Table 3.3 shows that the mean skin dose increased by 3.34±6.62% with the printed bolus. However, the dose did not increase homogeneously. Four TLDs decreased by 3% with the bolus compared with the non-bolus. The worst-case decreased by 7.5% at the S2. However, there was an 8.49% improvement in the skin dose with other measurement points. The central point (C) was enhanced the most at 15.13% using the customised bolus, which matched our expectations because it was the tangential point for the entire breast. The expected readout was 200 cGy for each measured point. The mean surface dose was 206.7 and 200.0 cGy with and without the printed bolus, respectively. The measurement was close to the planned dose (200 cGy per fraction) without the bolus. In addition, the SD was 8.8 and 16.7 without and with the printed bolus, respectively. When covered by the bolus, the variation of dose distribution on the surface increased. Finally, a paired T-test ($p = 0.20$) indicated the same result. There was no significant improvement in the surface dose when using the customised bolus. For this section, the bolus used was unsuitable for clinical application with potential air gap above the surface, due to dose uncertainty. This situation might be improved with a flexible printing material, leading to better surface conformity

3.3.3 Bolus-skin adhesion test

Figure 3.17 shows a histogram of the air gap volume from the CT simulation scan of the three patients. The results demonstrated that the mean air gap between the printed bolus and the patient's skin was 9.75±0.25 cubic centimetres (cc), indicating that the customised printed bolus did not perfectly match patient coverage. A large difference existed in the air gap distance across the thorax. The profiles for the three patients were similar. The histogram of the volume shows that conformity was superior in the lower lung. For the surface of the upper lung in this test, patient 2 illustrated a satisfactory result, whereas the results from patients 1 and 3 were unsatisfactory.

For patient 3, it could be claimed there was no satisfactory adhesion for the entire surface while there was improved contact between the printed bolus and skin around the heart level in the other two patients, indicating that the dose distribution followed the treatment planning outcome to avoid the heart, including the hot spot. The distance of the maximum air gap was 7.87, 7.68 and 8.28 mm for the three patients, respectively. The value was far larger than our target of 2 mm, which is proof that there is no negative impact on dose distribution [57]. The maximum distance reveals the high chance of unwanted dose distribution, particularly in the upper lung region, when covering the printed bolus.

Figure 3.18 displays the axial images from a different position. A clear air gap around the armpit region is observed in Figure 3.18 [a]. A large mismatch (>2mm) appeared at the lateral sides of the breast. However, in the lower part of the thorax shown in Figure 3.18 [b], the conformity improved with significant coverage and minimal air gap. Hence, there are more alternatives to manipulate the beam with tangential views for organs at risk (OAR). That gives us hope that there is potential to use the printed bolus in the context of post-mastectomy irradiation.

	Without	Bolus-covered	Difference (%)
S2	186.2	197.6	6.12
S1	208.6	192.9	-7.53
R2	195.7	207.8	6.18
R1	193	190.2	-1.45
L1	199.4	194.4	-2.51
L2	196.2	205.8	4.89
I1	205.2	203.3	-0.93
I2	215.8	237.6	10.1
C	200.2	230.5	15.13

Table 3.3: The TLD measurement (cGy) at a measuring point from a single session.

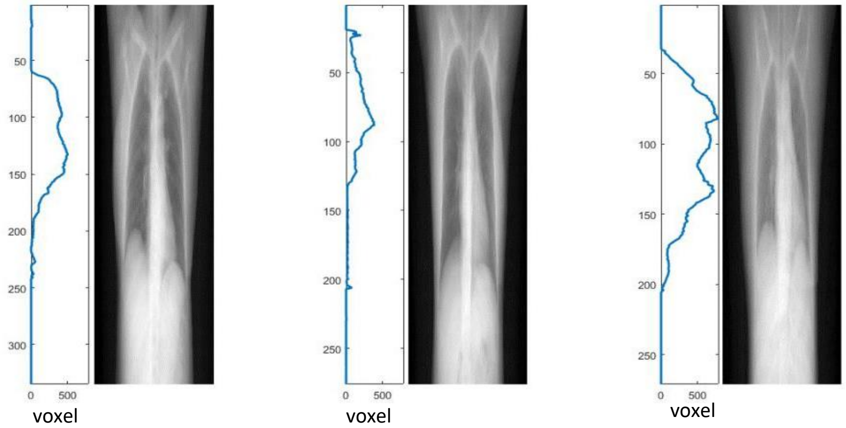

Figure 3.17: Volume (air voxel in each slice) of air gaps on the patients. For each figure, the left graph shows the volume of the air gap in each slice. The right image illustrated the corresponding location of patients.

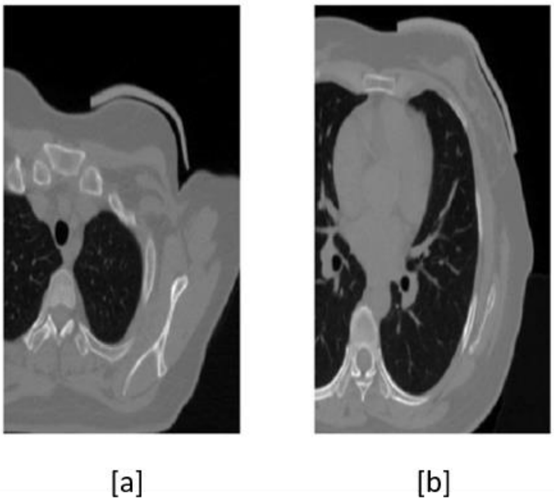

Figure 3.18: Variation in the conformity of the printed bolus on the same patient.

3.4 Discussion and Conclusion

Coverage of PTV at the superficial lesions is a challenge for high-energy photon therapy. The introduction of a 3D printing technique attracts the attention of the medical industry. To mitigate against the pitfalls of commercial boluses, printed boluses use a customised design for each patient. However, there is a lack of knowledge about the new material for medical use, and related studies performed dosimetric experiments while others did not test before clinical application.

To evaluate the feasibility of this new method, we developed a series of experiments. The knowledge of each printing material was developed under different circumstances. In this study, it was by measuring the PDD, which is difficult to compare across studies, but other studies have built customised boluses directly rather than providing PDD information as fundamental properties. Burleson measured the PDD of clear-PLA with a 6 MV and a 9 MeV 4 x 4 beam [74]. Their results implied that the HU must be set at 260 to correct the PDD curve in the treatment plan system, but the PLA used in this study was only -36 HU. The PDD curves of the printing material are crucial, and the test of the target material is satisfactory with promising PDD results.

This difference also showed in the measured d_{max}, which was 13.5 mm with a 6-MV photon beam in Burleson’s study, and 17.1 mm in this study. The d_{max} was shorter for the M_{target} under both the 6 MV photon and 9 MeV electron beam. Given the d_{max} measured, the minimum thickness was determined for the material. In addition, the field in our study was 10 x 10 cm, implying that there was more scatter radiation measured in the film. This work provided the concept for dosimetric properties with chamber measurement (Markus chamber). Using this data, the material can be confidently used for the first stage of this project.

The d_{max} of the target material, which is close to the d_{max} of water, indicated that it is quite similar to water. To approach tissue equivalence, the production process must be modified by shortening the exposure time. The current exposure time was chosen to meet the needs of supporting the printed product rather than achieving a density that approaches water. The advantage of using the SLA technique is the ability to control the hardness of the final product. The longer the exposure time, the longer the polymer chains and the harder the surface. Therefore, PDD experiments can be used to confirm whether a significant influence exists on d_{max}. A material that is close to tissue in terms of tissue equivalence would require several further experiments with a chamber to create a database for the treatment planning system.

The workflow for designing the bolus still needs to be more user-friendly. The clinicians would like to apply the PTV from the treatment plan system rather than a manual selection from the surface image. The current selection may lead to some mismatch.

It was assumed that the skin dose should increase when covered with the bolus and the phantom test demonstrated an unsatisfactory increase in skin dose with the use of the bolus. The experiment was improved for a better-measured method. The C point, at the tangential line of the beam, showed the most considerable improvement, where the regions with the least build-up were without the bolus in all points. Some measurement points, which were around the centre, decreased in absorbance of the dose. It is suspicious that the bolus did not adhere well to the phantom and resulted in the unnoticeable air gap.

This bolus was well-matched with the phantom visually, but air gaps may have occurred during the patients fitting test, which led to unpromising results. The mild distortion of the printed product led to unwanted dose coverage. Furthermore, this occurrence highlighted the idea that the addition of a CT scan is necessary to ensure the fit of the bolus. The thickness of the TLD was around 1.2 mm, which led to the mismatch between the printed bolus and the phantom. The research of Ha [77] and Robar [70] illustrated a significant agreement between the planned dose and measured dose under the printed bolus. Both boluses were designed with pockets on the skin side. The pockets allow OSLD chips to insert the bolus without creating space between the bolus and skin. This indicates that the future development direction of bolus designs is surface dose measurement with OSLD without an air gap.

The patients’ CT scans created an awareness of the pitfalls of the 3D-printed bolus. Various air gaps were found in all cases. The mismatch may lead to worse dose distribution than without the bolus because of the uncertainty of the air gap location from one day to another. Major issues contribute to the shaping of the armpit, and none of the three patients showed a strong attachment to the bolus. The negative outcome indicated to our team that the bolus should be specially designed in this region and suggested that the bolus attachment can easily change due to the influence of body weight. This is an essential finding of this research.

For our phantom study, the results showed zero air gap for the printed bolus, whereas, with the conventional bolus, they showed an air gap of 8 to 15 mm. The problem for the phantom experiment was the solid structure because the patient’s contours changed over time. However, few studies have determined the outcomes of the patient. Robar performed related work that compared a bolus printed with a flexible material with a conventional bolus on 16 patients. The results showed that the mean air gap was reduced to 3 mm with the printed bolus. The air gap regions greater than 5 mm were reduced by 30% when the printed bolus was used. The time from the image to bolus fabrication was not mentioned in their study. The body contours may not have changed significantly in this study. Our study showed a great disparity between the printed bolus and skin, particularly around the armpit area.

Robar obtained a similar finding. A single outlier case was noticed; there was a 2-cm air gap under the bolus in the last session. The case was confirmed to be due to an anatomical change by comparing the CT images across the two sessions. This information should be considered when applying the customised bolus. A repeat CT scan would be necessary for the conformity of the printed bolus.

3.4.1 Future work of 3D printing in radiotherapy

3.4.1.1 Extra CT scan

In the personalised bolus approach, an additional CT scan is required for bolus design, which forces patients to endure extra radiation exposure. Since this is a disadvantage, two potential options exist for reducing CT scans to meet ethical and clinical needs:

(a) Integrated virtual bolus. With superior knowledge of the properties of the printer materials, a virtual bolus could be precisely created using the treatment image with assigned election density for treatment management. Not only could the bolus be shaped with the OAR (the margin of the lung), it could also conform with possible body changes. Park [69] demonstrated this method by integrating the edge of the lung into the outer surface of the customised bolus. The hotspot from the electron beam dropped rapidly before the critical organ, which in this case was the ipsilateral lung.

(b) Optical surface scanner. The optical scanner allows physicists to capture surface information of patients. A bolus could be developed from these surface data, whereas internal information is limited before the planning CT. The bolus design may encounter difficulty if its only reference is the diagnosis CT.

Furthermore, the scanning room requires an alignment system, producing extra complication in the workflow. In terms of this concept, the source image for the bolus design could be linked with the Kinect image, as discussed in the previous chapter.

i. The research group must look for another phantom because the infrared from the Kinect cannot reflect the surface of the current transparent phantom accurately, leading to measurement errors in the depth map.
ii. The optical scan, Kinect, and CT scan are performed to capture the contour of the phantom.
iii. The workflow in section 3.2.2 can be followed to build a customised bolus.
iv. Two printed boluses can be taken to the CT scanner to acquire the image data.
v. The image registration proceeds for two sets of images to analyse the bolus difference with two modalities.

3.4.1.2 Knowledge of material science

Another limitation of the material in this experiment was radiation damage. The chemical bonds in the material break easily under high energy beams, not to mention proton beams. A strain test was presented by Michiels [78], and his study revealed that the printing material became even harder after 6 MV of irradiation. These exciting findings show that materials change their properties as they progress in tandem with the treatment sessions with patients. The printed material from both the FDM and the SLA techniques becomes stiffer after irradiation with the entire treatment dose, and this may imply changes in internal structure. Therefore, it is unclear whether these changes are of sufficient magnitude to have an impact on the dose distribution and to change the tolerance of the HU after irradiation should be considered.

This initial work shows high potential for the use of 3D printing in bolus fabrication, although we cannot deny that there are many steps in which improvement is required. This first glance of the proposed project offers a more sophisticated guideline for further progress. First, a multidisciplinary team is a priority. The process involves 3D graph design, material science, and radiation oncology. With additional research regarding these subjects, a conclusive result for the use of 3D printing in bolus fabrication can finally be determined. Medical application is strategic work and requires a significant amount of time to reach the goal for the following reasons:

i. When comparing the work, the bolus can be designed directly from TPS while our work takes a long detour from the CT image to the printed products.

ii. The mixture-of-material investigation. A mixture-of-material technique was introduced in which the printer can print a target material by mixing two material sources at a selected ratio, providing the opportunity to create an exact water-equivalent product when the range of the photon and electron beams (or even the proton beam alone), are known.

iii. Assessments of new methods must include more patients, and types of superficial tumour other than breast tumour should be included. With further cooperation with the local and leading hospital, the likely outcome will be more convincing.

This study revealed that 3D printing is a potential approach for customised bolus design. The printed bolus process provides a time- and cost-efficient approach for a personalised procedure of cancer therapy. The study showed that the performance of the material is acceptable for making a bolus by demonstrating a similar PPD curve to that of water. However, the outcomes of the surface dose enhancement and air gap fit were unacceptable for clinical use, although the interface of the program was improved. There was uncertainty regarding the processing of the bolus from the image to the final product, leading to a mismatch between the bolus and skin. Although CT imaging revealed a considerable air gap between the bolus and the patient’s skin, we believe this problem can be managed in future research. The optimisation of the current workflow and the inclusion of a specialist, such as a graph designer, are priorities for our future work.

Chapter 4

Final remarks

Radiotherapy has become a standard option for cancer treatment with the basic treatment criteria for each type of cancer demonstrated in the treatment guidelines. However, since the human body is sophisticated, treatment procedures beyond the guidelines should be developed for individuals of different ethnicities, and potentially, on an individual basis, also known as personalized cancer therapy. This thesis aimed to investigate two types of customised procedures in radiotherapy, which were performed in Shenzhen, as well as a personalised imaging system for a specific use. With numerous patients and limited medical resources in a city experiencing a period of rapid development, the need exists to explore and discover an alternative method for the improvement of treatment quality.

The treatment of two leading cancers worldwide, lung cancer and breast cancer is limited by time and if there is sufficient time in the treatment room, the problem of respiratory motion compensation can be managed with greater flexibility. The change in internal margin from respiratory motion causes uncertainty in treatment planning during radiation therapy. The application of surrogate signals and motion models could be a solution to this challenge as with knowledge provided by the motion model, the location of the tumour could potentially be estimated, although the related methods are time-consuming. Therefore, the solution to this problem was simplified to an approach that aimed to regularise the breathing cycle of patients.

The method we presented is vocal coaching, which requires patients to control their breathing cycle by following instructions. Vocal coaching is the most straightforward approach among the different attempts to regularise breathing as it does not require reading skills or knowledge on interaction with a digital device, which is occasionally a problem for older patients. However, the improvement of respiratory regularity by following vocal instruction was not observed in all patients. This study showed good performance when utilising the contactless monitoring system as a respiratory surrogate. The abdominal and thoracic breathing signals can be separated from the subject’s surface with post-processing. The fact that the variation in abdominal movement decreased the relationship between thoracic and abdominal breathing means breathing signals may become more complicated with vocal instruction. The subjects' breathing cycle that became more irregular with vocal instruction may be due to prior expectation, and this problem highlighted a field we had not considered human psychology. The need thus exists to design a questionnaire to investigate this possible issue with a much larger sample group. With limited patients and volunteers, the study showed mixed results on this topic and thus, increasing the number of participants is crucial for a more conclusive result.

Another critical treatment that this study investigated is post-mastectomy radiotherapy, for which our study evaluated a new printing material with a complete workflow. The dosimetry test showed that the material has a similar profile to water, less dose uncertainty between layers, thereby determining the minimal thickness of the bolus design. However, improvements in chamber measurement must be considered to obtain convincing dosimetric test results. The surface dose enhancement and conformity tests revealed this difficulty. Specifically, there was no significant dose increase with the bolus with a potential air gap, according to a thermoluminescent dosimeter. Due to positional uncertainty and alterations in body shape, unwanted moderate-to-large air gaps which were larger than the air gaps formed when using flexible commercial bolus were observed under the solid printed bolus used in our study. An adhesion test must be taken the following day during the scanning for CT simulation, and the volume of the thermoluminescent dosimeter must be taken into consideration during the design of the bolus to allow for extra space when covering the surface. This dosimetric result demonstrates that the printed bolus is not appropriate for clinical applications. To achieve a meaningful conclusion, a need exists to extend the investigation to an interdisciplinary group that includes 3D graph designers to ensure that the impact of body shape on the printed bolus that is processed and built overnight is minimised.

Both studies illustrated that a personalised procedure must rely on more precise control during the treatment sessions. Without a surrogate, it is difficult for the investigators to monitor the breathing signals of patients following instruction. Furthermore, it is difficult to analyse the dose distribution after positioning the bolus when a CBCT image is lacking. In terms of exploring the utilisation of vocal coaching and printed bolus as solutions for radiotherapy, the results were contradictory to our initial purposes. Currently, these methods require more effort and time to meet the same requirements as conventional methods. However, the two projects share a potential point as initial stages and further modifications such as increasing the sample size.

Bibliography

[1] M Wilms, R Werner, J Ehrhardt, a Schmidt-Richberg, H-P Schlemmer, and H Handels. Multivariate regression approaches for surrogate-based diffeomorphic estimation of respiratory motion in radiation therapy. *Physics in medicine and biology*, 59(5):1147–64, 2014.

[2] Hiroki Shirato, Yvette Seppenwoolde, Kei Kitamura, Rikiya Onimura, and Shinichi Shimizu. Intrafractional Tumor Motion: Lung and Liver. *Seminars in Radiation Oncology*, 14(1):10–18, 2004.

[3] Trine Juhler Nøttrup, Stine Sofia Korreman, Anders Navrsted Pedersen, Lasse Rye Aarup, Hakan Nystr˚ om, Mikael Olsen, and Lena Specht.¨ Intra- and interfraction breathing variations during curative radiotherapy for lung cancer. *Radiotherapy and Oncology*, 84(1):40–48, 2007.

[4] Tae Hyun Kim, Kwan Ho Cho, Hong Ryull Pyo, Jin Soo Lee, Jae Ill Zo, Dae Ho Lee, Jong Mog Lee, Hyae Young Kim, Bin Hwangbo, Sung Yong Park, Joo Young Kim, Kyung Hwan Shin, and Dae Yong Kim.Dose-volumetric Parameters for Predicting Severe Radiation Pneumonitis after Three-dimensional Conformal Radiation Therapy for Lung Cancer. *Radiology*, 235(1):208–215, 2005.

[5] Paul J Keall, Gig S Mageras, James M Balter, Richard S Emery, Kenneth M Forster, Steve B Jiang, Jeffrey M Kapatoes, Daniel a Low, Martin J Murphy, Brad R Murray, Chester R Ramsey, Marcel B Van Herk, S Sastry Vedam, John W Wong, and Ellen Yorke. *The management of respiratory motion in radiation oncology report of AAPM Task Group 76.*, volume 33. 2006.

[6] Daniel a. Low, Parag J. Parikh, Wei Lu, James F. Dempsey, Sasha H. Wahab, James P. Hubenschmidt, Michelle M. Nystrom, Maureen Handoko, and Jeffrey D. Bradley. Novel breathing motion model for radiotherapy. *International Journal of Radiation Oncology Biology Physics*, 63(3):921–929, 2005.

[7] Matthias Wilms, Jan Ehrhardt, Rene Werner, Mirko Marx, and Heinz´ Handels.Statistical analysis of surrogate signals to incorporate respiratory motion variability into radiotherapy treatment planning. (March 2014):90360J, 2014.

[8] ICRU 50. *ICRU Report 50*. 1993.

[9] T Landberg, J Chavaudra, and Hj Dobbs. *ICRU Report 62*. 1999.

[10] Anja Betgen, Tanja Alderliesten, Jan Jakob Sonke, Corine Van VlietVroegindeweij, Harry Bartelink, and Peter Remeijer. Assessment of setup variability during deep inspiration *ICRU Report 62*breath hold radiotherapy for breast cancer patients by 3D-surface imaging. *Radiotherapy and Oncology*, 106(2):225–230, 2013.

[11] Gikas S. Mageras and Ellen Yorke. Deep Inspiration Breath Hold and Respiratory Gating Strategies for Reducing Organ Motion in Radiation Treatment. *Seminars in Radiation Oncology*, 14(1):65–75, 2004.

[12] Ross I Berbeco, Hassan Mostafavi, Gregory C Sharp, and Steve B Jiang. Towards fluoroscopic respiratory gating for lung tumours without radiopaque markers. *Physics in medicine and biology*, 50(19):4481–4490, 2005.

[13] Ekberg, L., O. Holmberg, L. Wittgren, G. Bjelkengren, and T. Landberg. (1998). “What margins should be added to the clinical target volume in radiotherapy treatment planning for lung cancer?” Radiother Oncol 48:71–77.

[14] Kubo, H. D., and B. C. Hill. “Respiration gated radiotherapy treatment: A technical study.” Phys Med Biol 41(1):83–91.

[15] Papiez, L. (2003). “The leaf sweep algorithm for an immobile and moving target as an optimal control problem in radiotherapy delivery.” Mathematical and Computer Modelling 37:735–745.

[16] Engelsman, M., E. M. Damen, K. De Jaeger, K. M. van Ingen, and B. J.

Mijnheer. (2001). “The effect of breathing and set-up errors on the cumulative dose to a lung tumor.” Radiother Oncol 60(1):95–105.

[17] Murphy, M. J., J. R. Adler, Jr., M. Bodduluri, J. Dooley, K. Forster, J. Hai, Q. Le, G. Luxton, D.Martin, and J. Poen. (2000). “Image-guided radiosurgery for the spine and pancreas.” Comput Aided Surg 5(4):278–288.

[18] Chen, Q. S., M. S. Weinhous, F. C. Deibel, J. P. Ciezki, and R. M. Macklis. “Fluoroscopic study of tumor motion due to breathing: Facilitating precise radiation therapy for lung cancer patients.” Med Phys 28(9):1850–1856.

[19] Barnes, E. A., B. R. Murray, D. M. Robinson, L. J. Underwood, J. Hanson, and W. H. Roa. (2001). “Dosimetric evaluation of lung tumor immobilization using breath hold at deep inspiration.” Int J Radiat Oncol Biol Phys 50(4):1091–1098.

[20] Murphy, M. J., D. Martin, R. Whyte, J. Hai, C. Ozhasoglu, and Q. T. Le. (2002). “The effectiveness of breath-holding to stabilize lung and pancreas tumors during radiosurgery.” Int J Radiat Oncol Biol Phys 53(2):475–482.

[21] Ozhasoglu, C., and M. J. Murphy. (2002). “Issues in respiratory motion compensation during external-beam radiotherapy.” Int J Radiat Oncol Biol Phys 52(5):1389–1399.

[22] Tiezhi Zhang, Harry Keller, Matthew J O’Brien, Thomas R Mackie, and Bhudatt Paliwal. Application of the spirometer in respiratory gated radiotherapy. *Medical physics*, 30(12):3165–3171, 2003.

[23] Christopher Nelson, George Starkschall, Peter Balter, Rodolfo C. Morice, Craig W. Stevens, and Joe Y. Chang. Assessment of lung tumor motion and setup uncertainties using implanted fiducials. *International Journal of Radiation Oncology Biology Physics*, 67(3):915–923, 2007.

[24] P J Keall, V R Kini, S S Vedam, and R Mohan. Potential radiotherapy improvements with respiratory gating. *Australasian physical & engineering sciences in medicine / supported by the Australasian College of Physical Scientists in Medicine and the Australasian Association of Physical Sciences*

in Medicine, 25(1):1–6, 2002.

[25] Jeremy D P Hoisak, Katharina E. Sixel, Romeo Tirona, Patrick C F Cheung, and Jean Philippe Pignol. Correlation of lung tumor motion with external surrogate indicators of respiration. *International Journal of Radiation Oncology Biology Physics*, 60(4):1298–1306, 2004.

[26] G. S. Mageras, E. Yorke, K. Rosenzweig, L. Braban, E. Keatley, E. Ford, S. a. Leibel, and C. C. Ling. Fluoroscopic evaluation of diaphragmatic motion reduction with a respiratory gated radiotherapy system. *Journal of applied clinical medical physics] / American College of Medical Physics*, 2(4):191–200, 2001.

[27] Simon Hughes, James McClelland, Segolene Tarte, David Lawrence, Shahreen Ahmad, David Hawkes, and David Landau. Assessment of two novel ventilatory surrogates for use in the delivery of gated/tracked radiotherapy for non-small cell lung cancer. *Radiotherapy and Oncology*, 91(3):336–341, 2009.

[28] Nicole M. Wink, Christoph Panknin, and Timothy D. Solberg. Phase versus amplitude sorting of 4D-CT data. *Journal of Applied Clinical Medical Physics*, 7(1):77–85, 2006.

[29] Chiara Paganelli, Matteo Seregni, Giovanni Fattori, Paul Summers, Massimo Bellomi, Guido Baroni, and Marco Riboldi. Magnetic resonance imaging-guided versus surrogate-based motion tracking in liver radiation therapy: A prospective comparative study. *International Journal of Radiation Oncology Biology Physics*, 91(4):840–848, 2015.

[30] David P. Gierga, Johanna Brewer, Gregory C. Sharp, Margrit Betke, Christopher G. Willett, and George T.Y. Chen. The correlation between internal and external markers for abdominal tumors: Implications for respiratory gating. *International Journal of Radiation Oncology Biology Physics*, 61(5):1551–1558, 2005.

[31] Dan Ionascu, Steve B Jiang, Seiko Nishioka, Hiroki Shirato, and Ross I

Berbeco. Internal-external correlation investigations of respiratory induced motion of lung tumors. *Medical physics*, 34(10):3893–3903, 2007.

[32] Nicholas Koch, H. Helen Liu, George Starkschall, Marc Jacobson, Kenneth Forster, Zhongxing Liao, Ritsuko Komaki, and Craig W. Stevens. Evaluation of internal lung motion for respiratory-gated radiotherapy using MRI: Part I - Correlating internal lung motion with skin fiducial motion. *International Journal of Radiation Oncology Biology Physics*, 60(5):1459–1472, 2004.

[33] Hadi Fayad, Tinsu Pan, Jean Franc¸ois Clement, and Dimitris Visvikis. Technical note: Correlation of respiratory motion between external patient surface and internal anatomical landmarks. *Medical physics*, 38(6):3157–3164, 2011.

[34] T Klinder, C Lorenz, and J Ostermann. Free-breathing intra-and intersubject respiratory motion capturing, modeling, *Proceedings of SPIE*, 7259:1–11, 2009.

[35] Rohini George, Theodore D. Chung, Sastry S. Vedam, Viswanathan Ramakrishnan, Radhe Mohan, Elisabeth Weiss, and Paul J. Keall. Audiovisual biofeedback for respiratory-gated radiotherapy: Impact of audio instruction and audio-visual biofeedback on respiratory-gated radiotherapy. *International Journal of Radiation Oncology Biology Physics*, 65(3):924–933, 2006.

[36] Nobuyuki Otsu, P L Smith, D B Reid, Cluttered Environment, Lockheed Palo, Palo Alto, P L Smith, Nobuyuki Otsu, P L Smith, D B Reid, Cluttered Environment, Lockheed Palo, Palo Alto, P L Smith, Nobuyuki Otsu, P L Smith, D B Reid, Cluttered Environment, Lockheed Palo, Palo Alto, P L Smith, Nobuyuki Otsu, P L Smith, D B Reid, Cluttered Environment, Lockheed Palo, and Palo Alto. A Tlreshold Selection Method from Gray-Level Histograms. 20(1):62–66, 1979.

[37] D Rueckert, L I Sonoda, C Hayes, D L Hill, M O Leach, and D J Hawkes. Nonrigid registration using free-form deformations: application to breast

MR images. *IEEE Transactions on Medical Imaging*, 18(8):712–21, 1999.

[38] Marc Modat, Jamie McClelland, and Sebastien Ourselin. Lung Regis-´ tration Using the NiftyReg Package. *MICCAI2010 Workshop: Medical Image Analysis For The Clinic - A Grand Challenge*, (May):33–42, 2010.

[39] Daniel a Low, Michelle Nystrom, Eugene Kalinin, Parag Parikh, James F Dempsey, Jeffrey D Bradley, Sasa Mutic, Sasha H Wahab, Tareque Islam, Gary Christensen, David G Politte, and Bruce R Whiting. A method for the reconstruction of four-dimensional synchronized CT scans acquired during free breathing. *Medical physics*, 30(6):1254– 1263, 2003.

[40] Suk Jin Lee and Yuichi Motai. *Prediction and Classification of Respiratory Motion*, volume 525. 2014.

[41] Danny Lee, Peter B. Greer, Joanna Ludbrook, Jameen Arm, Perry Hunter, Sean Pollock, Kuldeep Makhija, Ricky T. O'Brien, Taeho Kim, and Paul Keall. Audiovisual Biofeedback Improves Cine-Magnetic Resonance Imaging Measured Lung Tumor Motion Consistency. *International Journal of Radiation Oncology Biology Physics*, 94(3):628–636, 2016.

[42] Alnowam, M. R., Lewis, E., Wells, K., & Guy, M. (2010, October). Respiratory motion modelling and prediction using probability density estimation. In IEEE Nuclear Science Symposuim & Medical Imaging Conference (pp. 2465-2469). IEEE. S Vedam, a Docef, M Fix, M Murphy, and P Keall. Dosimetric impact of geometric errors due to respiratory motion prediction on dynamic multileaf collimator-based four-dimensional radiation delivery. *Medical physics*, 32(6):1607–1620, 2005.

[43] P Giraud and R Garcia. Respiratory gating for radiotherapy: main technical aspects and clinical benefits. *Bulletin du cancer*, 97(Table 1):847–856, 2010.

[44] Tinsu Pan, Ting Yim Lee, Eike Rietzel, and George T.Y. Chen. 4D-CT imaging of a volume influenced by respiratory motion on multi-slice CT. *Medical Physics*, 31(2):333–340, 2004.

[45] Jan Jakob Sonke, Lambert Zijp, Peter Remeijer, and Marcel Van Herk. Respiratory correlated cone beam CT. *Medical Physics*, 32(4):1176– 1186, 2005.

[46] S. A. Nehmeh, Y. E. Erdi, C. C. Ling, K. E. Rosenzweig, O. D. Squire, L. E. Braban, E. Ford, K. Sidhu, G. S. Mageras, S. M. Larson, and J. L.Humm. Effect of respiratory gating on reducing lung motion artifacts in PET imaging of lung cancer. *Medical Physics*, 29(3):366–371, 2002.

[47] Raghu B. Venkat, Amit Sawant, Yelin Suh, Rohini George, and Paul J. Keall. Development and preliminary evaluation of a prototype audiovisual biofeedback device incorporating a patient-specific guiding waveform. *Physics in Medicine and Biology*, 53(11), 2008.

[48] Jesang Yu, Ji Hoon Choi, Sun Young Ma, Tae Sig Jeung, and Sangwook Lim. Comparison between audio-only and audiovisual biofeedback for regulating patients’ respiration during four-dimensional radiotherapy. *Radiation Oncology Journal*, 33(3):250–255, 2015.

[49] Fumiya Baba, Satoshi Tanaka, Yoshinori Nonogaki, Shinji Hasegawa, Minami Nishihashi, Shiho Ayakawa, Maho Yamada, and Yuta Shibamoto. Effects of audio coaching and visual feedback on the stability of respiration during radiotherapy. *Japanese Journal of Radiology*, 34(8):572–578, 2016.

[50] Robyn Keall and Paul Keall. Pollock et al. - 2015 - Breathing guidance in radiation oncology and radiology A systematic review of patient and healthy volunteer studies.pdf.

[51] F. Tahavori, M. Alnowami, and K. Wells. Marker-less Respiratory Motion Modeling Using the Microsoft Kinect for Windows. *SPIE Medical Imaging*, 9036(0):1–10, 2014.

[52] F. Tahavori, E. Adams, M. Dabbs, L. Aldridge, N. Liversidge, E. Donovan, T. Jordan, Pm. Evans, and K. Wells. Combining marker-less patient setup and respiratory motion monitoring using Kinect. 9415:94152I, 2015.

[53] Mirco Heß, Florian Buther, Fabian Gigengack, Mohammad Dawood,¨ and Klaus P. Schafers. A dual-Kinect approach to determine torso sur-¨ face motion for respiratory motion correction in PET. *Medical Physics*, 42(5):2276–2286, 2015.

[54] Danny Lee, Peter B. Greer, Chiara Paganelli, Joanna Jane Ludbrook, Taeho Kim, and Paul Keall. Audiovisual biofeedback improves the correlation between internal/external surrogate motion and lung tumor motion:. *Medical Physics*, 45(3):1009–1017, 2018.

[55] Joel Schaerer, Aurora Fassi, Marco Riboldi, Pietro Cerveri, Guido Ba-¨ roni, and David Sarrut. Multi-dimensional respiratory motion tracking from markerless optical surface imaging based on deformable mesh registration. *Physics in Medicine and Biology*, 57(2):357–373, 2011.

[56] F. Tahavori, E. Adams, M. Dabbs, L. Aldridge, N. Liversidge, E. Donovan, T. Jordan, Pm. Evans, and K. Wells. Combining marker-less patient setup and respiratory motion monitoring using Kinect. 9415:94152I, 2015.

[57] F. Tahavori, M. Alnowami, J. Jones, P. Elangovan, E. Donovan, and K. Wells. Assessment of Microsoft Kinect technology (Kinect for Xbox and Kinect for windows) for patient monitoring during external beam radiotherapy. *IEEE Nuclear Science Symposium Conference Record*, 2013.

[58] M. Alnowami, B. Alnwaimi, F. Tahavori, M. Copland, and K. Wells. A quantitative assessment of using the Kinect for Xbox360 for respiratory surface motion tracking. *Proc. SPIE*, 8316:83161T–83161T–10, 2012.

[59] Fatemeh Tahavori, Ashrani Aizzuddin, Abd Rahni, and Kevin Wells.A Statistical Analysis of External Respiratory Motion Using Microsoft Kinect. pages 2–5, 2014.

[60] Majdi R. Alnowam, E. Lewis, K. Wells, and M. Guy. Marker-less tracking for respiratory motion correction in nuclear medicine. *IEEE Nuclear Science Symposium Conference Record*, pages 3118–3121, 2010.

[61] Zheng, Lianrong, et al. "Detection of respiration movement asymmetry between the left and right lungs using mutual information and transfer entropy." IEEE Access 6 (2017): 605-613.

[62] Sidsel M.S. Damkjær, Marianne C. Aznar, Anders N. Pedersen, Ivan R. Vogelius, Jens Peter Bangsgaard, and Mirjana Josipovic. Reduced lung dose and improved inspiration level reproducibility in visually guided DIBH compared to audio coached EIG radiotherapy for breast cancer patients. *Acta Oncologica,* 52(7):1458–1463, 2013.

[63] R. George, S. S. Vedam, T. D. Chung, V. Ramakrishnan, and P. J. Keall. The application of the sinusoidal model to lung cancer patient respiratory motion. *Medical Physics*, 32(9):2850–2861, 2005.

[64] M Alnowami, E Lewis, M Guy, K Wells, and M Guy. Inter-and intra-subject variation of abdominal vs. thoracic respiratory motion using kernel density estimation. *IEEE Nuclear Science Symposuim & Medical Imaging Conference,* pages 2921–2924, 2010.

[65] Yousaf Khan, J Eduardo Villarreal-barajas, Mona Udowicz, Richie Sinha, Wazir Muhammad, Ahmed N Abbasi, and Amjad Hussain. Clinical and Dosimetric Implications of Air Gaps between Bolus and Skin Surface during Radiation Therapy. 2013(September):1251–1255, 2013.

[66] M J Butson, T Cheung, and P K N Yu. Radiochromic film for verification of superficial x-ray backscatter factors. *Australasian physical & engineering sciences in medicine / supported by the Australasian College of Physical Scientists in Medicine and the Australasian Association of Physical Sciences in Medicine*, 30(4):269–273, 2007.

[67] Martin J. Butson, Tsang Cheung, Peter Yu, and Peter Metcalfe. Effects on skin dose from unwanted air gaps under bolus in photon beam radiotherapy. *Radiation Measurements,* 32(3):201–204, 2000.

[68] Merisa L. Piper, Maristella Evangelista, Dominic Amara, David Daar, Robert D. Foster, Barbara Fowble, and Hani Sbitany. An innovative risk-

reducing approach to Postmastectomy radiation delivery after autologous breast reconstruction. *Plastic and Reconstructive Surgery Global Open*, 5(4):1–9, 2017.

[69] J. W. Park and J. W. Yea. Three-dimensional customized bolus for intensity-modulated radiotherapy in a patient with Kimura's disease involving the auricle. *Cancer/Radiotherapie*, 20(3):205–209, 2016.

[70] R. J. Kudchadker. Utilization of custom electron bolus in head and neck radiotherapy. *Journal of Applied Clinical Medical Physics*, 4(4):321, 2003.

[71] Yuehong Kong, Tengfei Yan, Yanze Sun, Jianjun Qian, Gang Zhou, Shang Cai, and Ye Tian. A dosimetric study on the use of 3D-printed customized boluses in photon therapy: A hydrogel and silica gel study. *Journal of Applied Clinical Medical Physics*, (August):1–8, 2018.

[72] Gerd Becker and Dirk Bottke. Radiotherapy in the management of Kaposi's sarcoma. *Onkologie*, 29(7):329–333, 2006.

[73] Rulon Mayer, Peter Liacouras, Andrew Thomas, Minglei Kang, Liyong Lin, and Charles B. Simone. 3D printer generated thorax phantom with mobile tumor for radiation dosimetry. *Review of Scientific Instruments*, 86(7), 2015.

[74] Sarah Burleson, Jamie Baker, An T ing Hsia, and Zhigang Xu. Use of 3D printers to create a patient-specific 3D bolus for external beam therapy. Journal of applied clinical medical physics / American College of Medical Physics, 16(3):5247, 2015.

[75] Min Joo Kim, Seu Ran Lee, Min Young Lee, Jason W. Sohn, Hyong Geon Yun, Joon Yong Choi, Sang Won Jeon, and Tae Suk Suh. Characterization of 3D printing techniques: Toward patient specific quality assurance spine-shaped phantom for stereotactic body radiation therapy. *PLoS ONE*, 12(5):1–12, 2017.

[76] Matthew S. Brown, Michael F. McNitt-Gray, Nicholas J. Mankovich, Jonathan G. Goldin, John Hiller, Laurence S. Wilson, and Denise R. Aberle. Method for segmenting chest CT image data using an anatomical model:

Preliminary results. *IEEE Transactions on Medical Imaging*, 16(6):828–839, 1997.

[77] Jin-suk Ha, Jae Hong Jung, Min-joo Kim, Mi Jin Jeon, and Won Suk Jang. Customized 3D Printed Bolus for Breast Reconstruction for Modified Radical Mastectomy (MRM). 27(4):196–202, 2016.

[78] James L. Robar, Kathryn Moran, James Allan, James Clancey, Tami Joseph, Krista Chytyk-Praznik, R. Lee MacDonald, John Lincoln, Parisa Sadeghi, and Robert Rutledge. Intrapatient study comparing 3D printed bolus versus standard vinyl gel sheet bolus for postmastectomy chest wall radiation therapy. *Practical Radiation Oncology*, 8(4):221– 229, 2018.

[79] Steven Michiels, Antoine D'Hollander, Nicolas Lammens, Mathias Kersemans, Guozhi Zhang, Jean-marc Denis, Kenneth Poels, Edmond Sterpin, Sandra Nuyts, Karin Haustermans, and Tom Depuydt. Towards 3D printed multifunctional immobilization for proton therapy: Initial materials characterization. *Medical Physics*, 10(10):5392–5402, 2016.

Appendix

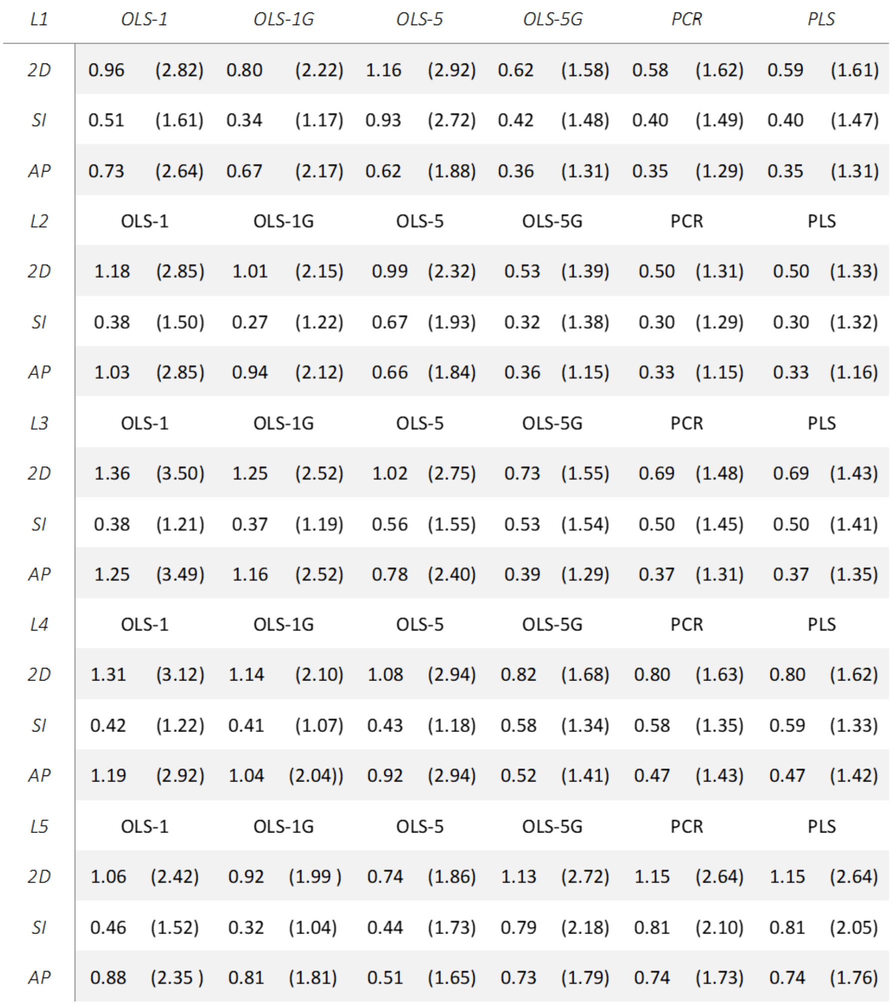

L1	*OLS-1*		*OLS-1G*		*OLS-5*		*OLS-5G*		*PCR*		*PLS*	
2D	0.96	(2.82)	0.80	(2.22)	1.16	(2.92)	0.62	(1.58)	0.58	(1.62)	0.59	(1.61)
SI	0.51	(1.61)	0.34	(1.17)	0.93	(2.72)	0.42	(1.48)	0.40	(1.49)	0.40	(1.47)
AP	0.73	(2.64)	0.67	(2.17)	0.62	(1.88)	0.36	(1.31)	0.35	(1.29)	0.35	(1.31)
L2	OLS-1		OLS-1G		OLS-5		OLS-5G		PCR		PLS	
2D	1.18	(2.85)	1.01	(2.15)	0.99	(2.32)	0.53	(1.39)	0.50	(1.31)	0.50	(1.33)
SI	0.38	(1.50)	0.27	(1.22)	0.67	(1.93)	0.32	(1.38)	0.30	(1.29)	0.30	(1.32)
AP	1.03	(2.85)	0.94	(2.12)	0.66	(1.84)	0.36	(1.15)	0.33	(1.15)	0.33	(1.16)
L3	OLS-1		OLS-1G		OLS-5		OLS-5G		PCR		PLS	
2D	1.36	(3.50)	1.25	(2.52)	1.02	(2.75)	0.73	(1.55)	0.69	(1.48)	0.69	(1.43)
SI	0.38	(1.21)	0.37	(1.19)	0.56	(1.55)	0.53	(1.54)	0.50	(1.45)	0.50	(1.41)
AP	1.25	(3.49)	1.16	(2.52)	0.78	(2.40)	0.39	(1.29)	0.37	(1.31)	0.37	(1.35)
L4	OLS-1		OLS-1G		OLS-5		OLS-5G		PCR		PLS	
2D	1.31	(3.12)	1.14	(2.10)	1.08	(2.94)	0.82	(1.68)	0.80	(1.63)	0.80	(1.62)
SI	0.42	(1.22)	0.41	(1.07)	0.43	(1.18)	0.58	(1.34)	0.58	(1.35)	0.59	(1.33)
AP	1.19	(2.92)	1.04	(2.04))	0.92	(2.94)	0.52	(1.41)	0.47	(1.43)	0.47	(1.42)
L5	OLS-1		OLS-1G		OLS-5		OLS-5G		PCR		PLS	
2D	1.06	(2.42)	0.92	(1.99)	0.74	(1.86)	1.13	(2.72)	1.15	(2.64)	1.15	(2.64)
SI	0.46	(1.52)	0.32	(1.04)	0.44	(1.73)	0.79	(2.18)	0.81	(2.10)	0.81	(2.05)
AP	0.88	(2.35)	0.81	(1.81)	0.51	(1.65)	0.73	(1.79)	0.74	(1.73)	0.74	(1.76)

*

Individual results for each target landmark. The mean 2D Euclidean, SI, and AP distance for each of the target landmarks (in mm).

Details of MATLAB file

- Code snippet 1 Surface contouring program:

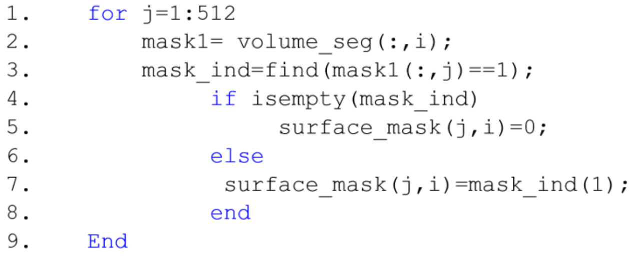

```
for j=1:512
    mask1= volume_seg(:,i);
    mask_ind=find(mask1(:,j)==1);
         if isempty(mask_ind)
              surface_mask(j,i)=0;
         else
          surface_mask(j,i)=mask_ind(1);
         end
End
```

Code snippet 2. Surface smoothing and thickening program:

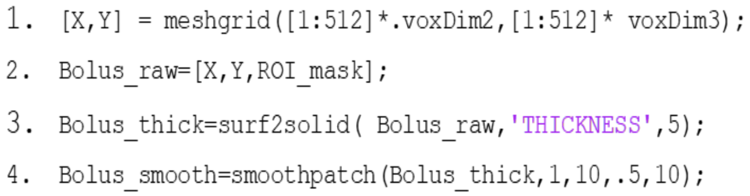

```
[X,Y] = meshgrid([1:512]*.voxDim2,[1:512]* voxDim3);
Bolus_raw=[X,Y,ROI_mask];
Bolus_thick=surf2solid( Bolus_raw,'THICKNESS',5);
Bolus_smooth=smoothpatch(Bolus_thick,1,10,.5,10);
```

Code snippet: 3 air gap detection

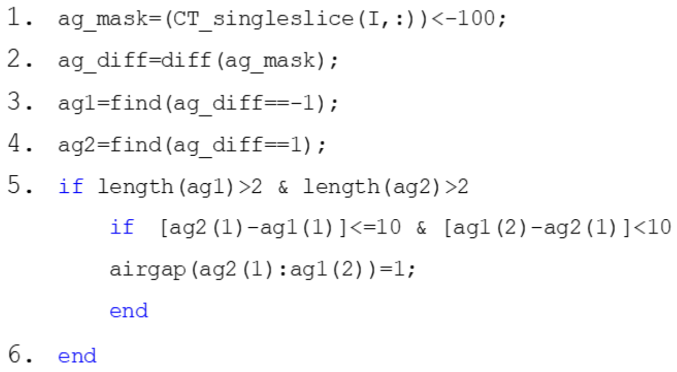

```
ag_mask=(CT_singleslice(I,:))<-100;
ag_diff=diff(ag_mask);
ag1=find(ag_diff==-1);
ag2=find(ag_diff==1);
if length(ag1)>2 & length(ag2)>2
    if  [ag2(1)-ag1(1)]<=10 & [ag1(2)-ag2(1)]<10
    airgap(ag2(1):ag1(2))=1;
    end
end
```

Code snippet: 3 air gap detection

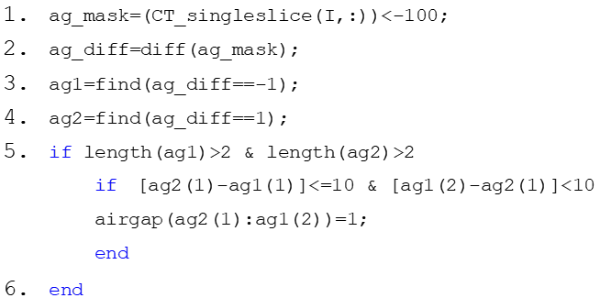

ag_mask=(CT_singleslice(I,:))<-100;
ag_diff=diff(ag_mask);
ag1=find(ag_diff==-1);
ag2=find(ag_diff==1);
if length(ag1)>2 & length(ag2)>2
    if [ag2(1)-ag1(1)]<=10 & [ag1(2)-ag2(1)]<10
    airgap(ag2(1):ag1(2))=1;
    end
end